

1 **J/ψ production in Au+Au collisions at $\sqrt{s_{NN}} = 39, 62.4,$ and 200GeV**
2 **Analysis notes**

3 Wangmei Zha^{1,2,*}

4 ¹*University of Science and Technology of China, Hefei, China*

5 ²*Brookhaven National Laboratory, New York, USA*

The Relativistic Heavy Ion Collider (RHIC) is built to search for the Quark-gluon Plasma (QGP) and to study its properties in laboratory through high energy heavy-ion collisions. J/ψ suppression in heavy-ion collisions due to color screening of quark and anti-quark potential has been proposed as a signature of QGP formation. Other mechanisms are likely to contribute to the observed J/ψ production in heavy-ion collisions such as the cold nuclear matter effect and charm quark recombination. Measurements of J/ψ invariant yields at different collision energies can shed new light on understanding the interplay of these mechanisms for J/ψ production and medium properties. In this analysis notes, we report on the measurements of J/ψ invariant yields as a function of transverse momentum at midrapidity ($|y| < 1.0$) in Au+Au collisions at $\sqrt{s_{NN}} = 39, 62.4$ and 200 GeV taken by STAR with full Time-of-Flight detector and Barrel Electromagnetic Calorimeter in operation. Centrality dependence of J/ψ production and nuclear modification factors are presented. Comparisons among different collision energies and model calculations are discussed.

* wangmei@rcf.rhic.bnl.gov

1
CONTENTS

I.	Run 2011 Au + Au 200 GeV Analysis	4
	A. Data sets and Triggers	4
	B. Event Selection	4
	C. Track Selection	6
	D. Electron Identification	6
	1. TPC dE/dx	6
	2. TOF $1/\beta$	7
	3. BEMC p/E	8
	E. Efficiency and Acceptance	8
	1. TPC tracking efficiency and acceptance	8
	2. Momentum resolution	10
	3. BEMC cuts efficiency	11
	4. TOF cuts efficiency	13
	5. $n\sigma_e$ cuts efficiency	14
	6. nHitsDedx cuts efficiency	15
	F. Total J/ψ detection efficiency	15
	G. J/ψ signal and invariant yield	15
	1. J/ψ signal	15
	2. J/ψ invariant p_T spectrum	19
	H. Systematic uncertainty estimation	20
	1. Tracking efficiency	20
	2. $n\sigma_e$ cut efficiency	22
	3. TOF matching efficiency	23
	4. $1/\beta$ cut efficiency	23
	5. BEMC mathcing and cut efficiency	23
	6. Yield extraction	23
	7. J/ψ internal radiation	24
	8. Summary of systematic uncertainty source	25
II.	Run 2010 Au+Au 62.4 and 39 GeV Analysis	25
	A. Data sets and Triggers	25
	B. Event Selection	25
	C. Track Selection	28
	D. Electron Identification	28
	E. Efficiency and Acceptance	34
	TPC tracking efficiency and acceptance	34
	Momentum resolution	35
	BEMC cuts efficiency	36
	TOF cuts efficiency	37
	$n\sigma_e$ cuts efficiency	38
	nHitsDedx cuts efficiency	39
	F. Total J/ψ detection efficiency	39
	G. J/ψ signal and invariant yield	40
	J/ψ signal	41
	J/ψ invariant p_T spectrum	41
	H. Systematic uncertainties	41

1	III. The interpolation of pp reference at $\sqrt{s} = 39$ and 62.4 GeV	45
2	IV. Introduction	45
3	V. Available experimental results treatment	46
4	VI. Results	47
5	VII. summary	53
6	VIII. Nuclear Modification Factor	53
7	References	55
8	IX. Appendix	57
9	A. J/ψ signal in Au+Au 39 GeV	57
10	B. J/ψ signal in Au+Au 62 GeV	58
11	C. $J/\psi p_T$ spectrum in different centrality bins for Au+Au 39, 62, and 200 GeV collisions	59
12	D. The $J/\psi p_T$ spectrum for 200 GeV in comparison with published RHIC RUN 2010 results	59
13		

I. RUN 2011 AU + AU 200 GEV ANALYSIS

A. Data sets and Triggers

This analysis uses the minimum bias (MB) Au+Au data recorded in 2011. The MB trigger IDs include 350003, 350013, 350023, 350033, 350043. The minimum bias trigger for Au + Au required a coincidence between the East and West VPD, selecting on collisions within 30 cm of the interaction region along the beam line on the z-axis. The recorded number of events for the MB trigger in Au + Au collisions are shown in Figure 1, and a total of 740 M events were analyzed. The data was produced in the production series P11id usig library version SL11d.

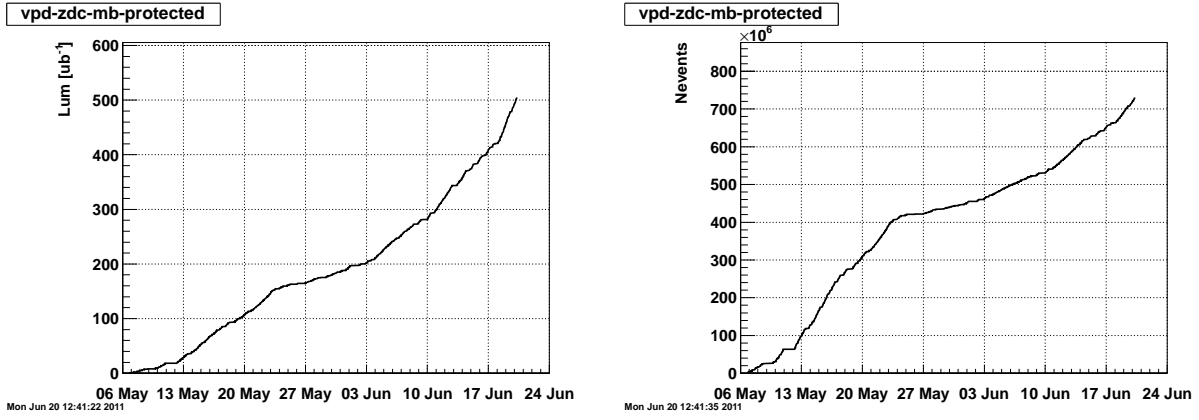


FIG. 1. The luminosity (left) and events (right) of MB trigger recorded for Au+Au collisions at $\sqrt{s_{NN}} = 200$ GeV versus time. Figures are taken from [1].

B. Event Selection

The minimum bias trigger identifies collisions that occur within $|V_z| < 30\text{cm}$, and this online vertex position is determined from the time difference in the East and West VPD signals. The offline vertex position is determined by the vertex finding algorithm implemented for Au+Au collisions (MinuitVF), which minimizes the distance of closest approach of the reconstructed tracks at the origin. The VPD trigger is less efficient in low multiplicity collisions, which causes losses in peripheral Au+Au collisions. Only data in 0 - 60% central Au+Au collisions, where the VPD inefficiency is negligible, were used in this analysis. The left panel of Figure 2 shows the VPD V_z (called $V_z(VPD)$) distribution in Au+Au collisions versus the reconstructed V_z obtained using MinuitVF (called $V_z(TPC)$). From the left panel of Figure 2 , there is a very strong correlation between the $V_z(VPD)$ and $V_z(TPC)$ in most of the events, but there are some bad events which are some bad events which are not what we wanted to trigger like pileup events or the vertex finder fails to find the triggered V_z or something else. These kinds of events are shown as the horizontal and vertical bands in the left panel of Figure 2. The right panel of Figure 2 shows the distribution of the difference between $V_z(VPD)$ and $V_z(TPC)$. The huge peak around zero is what we want to select. We used a $|V_z(TPC) - V_z(VPD)| < 4\text{cm}$ cut to reject the background events. The left panel of Figure 3 shows the V_x vs. V_y distribution before the vertex cut ($|V_z(TPC) - V_z(VPD)| < 4\text{cm}$). Most of the events collided around 0, but clearly there are some events happening on the beam pipe. The right panel of this figure shows the same distribution after the vertex cut. The beam pipe events are successfully removed by the vertex cut. The vertexes of the survived events are very concentrated

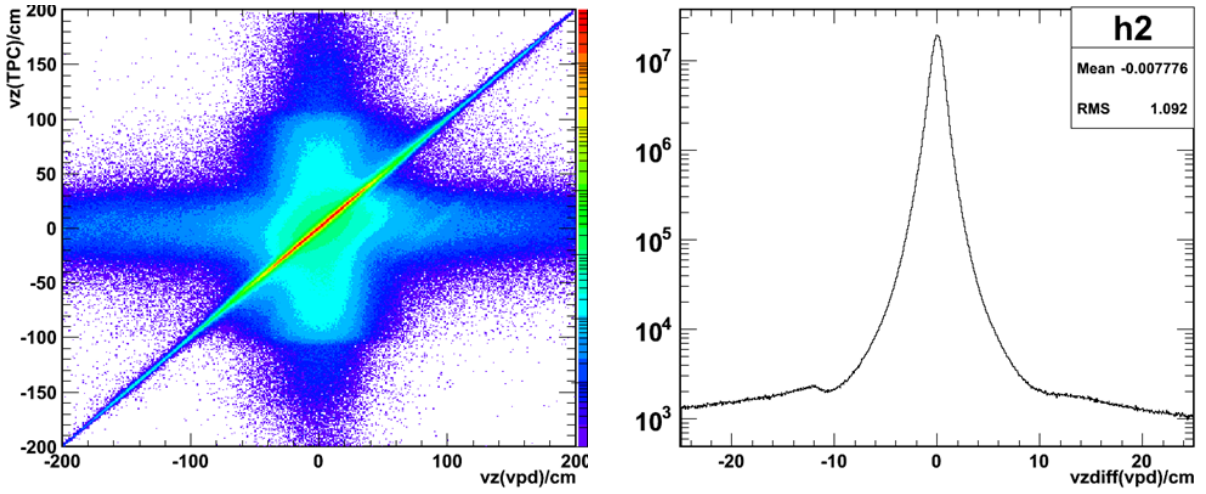


FIG. 2. The VPD V_z versus the reconstructed V_z position in Au+Au collisions (left panel), and the difference between $V_z(VPD)$ and $V_z(TPC)$, V_{zdiff} (right panel).

around 0. The centrality is determined from the StRefMultCorr class. The reference multiplicity

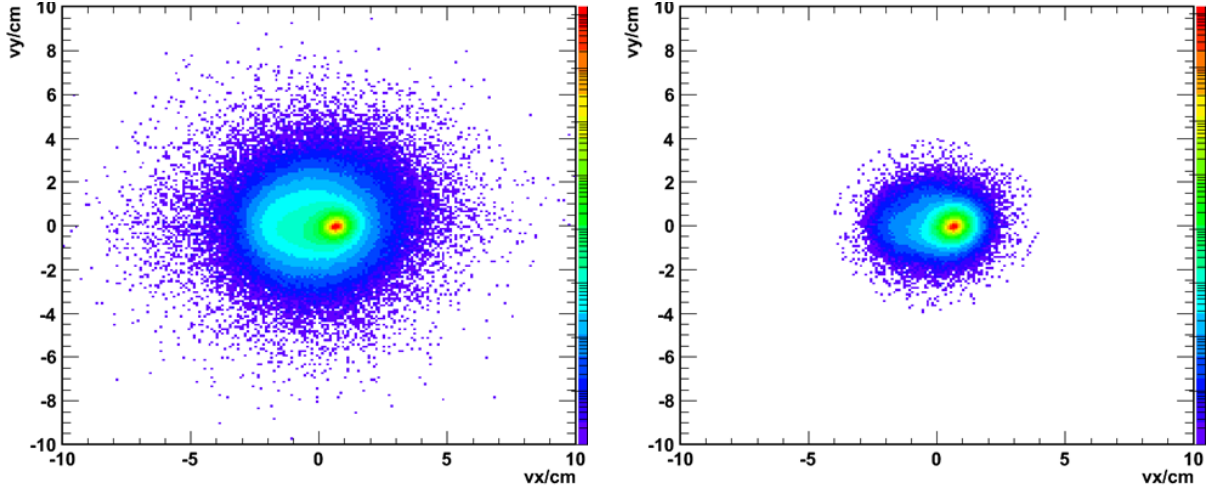


FIG. 3. V_x vs. V_y distribution before and after vertex cuts in MB triggered 200 GeV Au+Au collisions taken in Run 2011

cut for each centrality depends on the V_z , luminosity and runnumber. Details can be found at [2]

Event Cut Parameters	Cut Value	accepted Events
Trigger Ids	350003 or 350013 or 350023 or 350033 or 350043	615 M
Valid vertex	$ V_x(TPC) > 10^{-5} \text{ cm}$ or $ V_y(TPC) > 10^{-5} \text{ cm}$ or $ V_z(TPC) > 10^{-5} \text{ cm}$	585 M
Vertex correlation	$ V_z(TPC) - V_z(VPD) < 4 \text{ cm}$	552 M
V_z	$ V_z(TPC) < 30 \text{ cm}$	516 M
$V_r = \sqrt{V_x^2 + V_y^2}$	$ V_r(TPC) < 2 \text{ cm}$	515 M
centrality	0-60%	360 M

TABLE I. Event selection cuts for 2011 200 GeV Au+Au collisions

1 **C. Track Selection**

2 The TPC provides tracking for charged particles with full azimuthal coverage and pseudorapidity
 3 coverage at midrapidity. Tracks are required to have $p_T > 0.2\text{GeV}/c$ in order to reach the outer
 4 radius of the TPC. To ensure a high track reconstruction quality, requirements are placed on the
 5 number of reconstructed hit points ($n\text{HitsFit}$), the number of dE/dx hit points ($n\text{HitsDedx}$), and the
 6 distance of closest approach between the track and the vertex (dca). Tracks are required to have
 7 $n\text{HitsFit} \geq 25$, $n\text{HitsDedx} \geq 15$ and $dca < 3\text{cm}$ in Au+Au collisions. The minimum number of
 8 spatial and dE/dx hits are chosen to reject poorly reconstructed tracks. Tracks are also assigned a
 9 flag during the fitting process to indicate the fit quality and detector used in the fitting. Tracks,
 10 which are poorly reconstructed, have flag < 0 and are not what we wanted. Post-crossing tracks
 11 that from pile-up have flag > 1000 and are also not considered. The quality requirements for tracks
 12 reconstructed in Au+Au collisions are listed in Table II.

Transverse Momentum	$p_T > 0.2\text{GeV}/c$
Pseudorapidity	$ \eta < 1.0$
Track Flag	$flag > 0$ and $flag < 1000$
Spatial Hits	$n\text{HitsFit} \geq 25$
dE/dx Hits	$n\text{HitsDedx} \geq 15$
$dca (p < 1.5 \text{ GeV}/c)$	$dca < 3\text{cm}$
$dca (p > 1.5 \text{ GeV}/c)$	$dca < 1\text{cm}$

13 TABLE II. Primary track selection in Au+Au collisions.
 14

15 **D. Electron Identification**

16 The J/ψ is reconstructed via its dielectron decay channel. In order to select electron and reject
 17 hadron, the TPC has been used as the primary tool for electron identification in STAR, and utilizes
 18 the reconstructed momentum and ionization energy loss per unit length (dE/dx). The TOF and
 19 BEMC has been used to further discriminate between electrons and hadrons at low and hight p_T ,
 20 respectively. The details of the electron identification methods using the TPC, BEMC, and TOF
 21 are described below.

22 1. *TPC dE/dx*

23 The Time Projection Chamber has been used for track reconstruction and measuring particle
 24 ionization energy loss per unit length (dE/dx). The track momentum and dE/dx have been used to
 25 identify electrons, and this is illustrated in 4 for charged particles in Au+Au collisons. The expected
 26 dE/dx values for various particles obtained from Bichsel functions [3] are also shown (lines). In
 27 order to identify electrons, the dE/dx is normalized to the expected dE/dx for electrons obtained
 28 from the Bichsel functions ($dE/dx_{Bichsel}$) and scaled by the dE/dx resolution ($\sigma_{dE/dx}$) to obtain the
 29 probability of a track being an electron ($n\sigma_e$). The variable $n\sigma_e$ is defined to have an expected mean
 30 of 0 and width of 1, where

$$31 \quad n\sigma_e = \log\left(\frac{dE/dx_{Measured}}{dE/dx_{Bichsel}}\right)/\sigma_{dE/dx} \quad (1)$$

32 The measured mean and width of the $n\sigma_e$ distribution are not exactly equal to 0 and 1, and must
 33 be determined from data (using photonic electron samples). One can see that there are a lot of

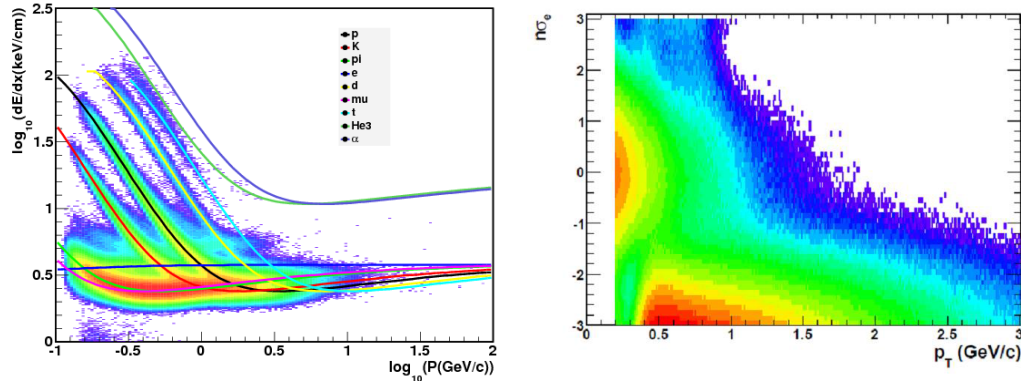


FIG. 4. The energy loss per unit length, dE/dx , of charged particles in Au+Au collisions. The solid lines indicate the expected dE/dx obtained from the Bichsel functions [3]

hadrons, especially pions in the sample. $-1.5 \leq n\sigma_e \leq 2$ cut selects electrons very efficiently and rejects a lot of pions in the whole momentum range and other hadrons.

3 2. TOF $1/\beta$

4 The mass of electrons is negligible in the momentum range considered in this analysis, and as a
5 result they have a velocity $\beta \equiv v/c \sim 1$. Heavier particles will travel slower at a given momentum,
6 thus the TOF can be used to separate these from the electrons by measuring the particle flight time
7 and velocity. As the momentum of particles increases, their velocity approaches c and hadrons can
8 no longer be discriminated from electrons. The TOF can be used to separate electrons from heavier
9 hadrons up to $p \sim 1.5 GeV/c$, but can not remove all pions due to their small mass. Tracks in the

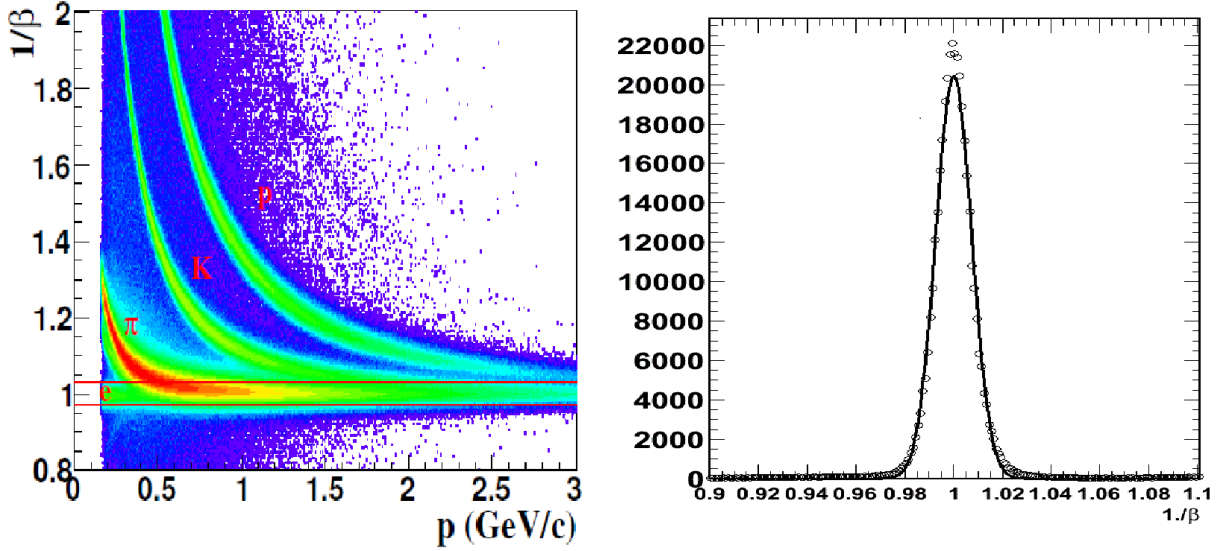


FIG. 5. The TOF $1./\beta$ versus TPC momentum for all charged particles in Au+Au collisions (left panel). The lines indicate the expected value for various particles. The $1./\beta$ for electrons with $0.2 < p_T < 0.3 GeV/c$ (right panel) is fitted with a Gaussian

10
11 TPC are matched to the TOF in order to calculate their flight time and velocity. The TOF $1/\beta$
12 distribution is shown in the left panel of Figure 5 as a function of TPC momentum for all charged
13 particles in Au+Au collisions. The expected $1/\beta$ has been calculated using the mass of each particle
14

[4], and these are shown (lines). The $1/\beta$ distribution for electrons with $0.2 < p_T < 0.3\text{GeV}/c$ is depicted in the right panel of Figure 5, and has been fitted with a Gaussian function to obtain a width of $\sigma = 0.01$. Electrons are identified by requiring $|1/\beta - 1| < 0.03$, corresponding to a 3σ cut around $1/\beta = 1$.

5 3. BEMC p/E

The BEMC has been used to discriminate between electrons and hadrons and improve the purity of the electron candidates used for J/ψ reconstruction. This was done by considering the energy deposited in the BEMC towers (BTOW), and the shower shape obtained by BEMC shower maximum detector (BSMD). The energy deposited by electrons in the BTOW is approximately equal to their momentum, and electron can be identified from their momentum-to-energy ratio $p/E \sim 1$ (as shown in Fig. 6). Electromagnetic showers are also more developed than hadronic showers, and the BSMD η and ϕ strips can be used to distinguish between electrons and hadrons. The BSMD can also provide the information of the shower position more accurately than that of the BTOW. However, There is no BSMD information recorded in Run 11 MB data. We can only used BTOW to pure our electron samples.

Tracks in the TPC were projected outwards to the BEMC to determine the η and ϕ coordinates of the particle as it struck the BEMC. Towers were required to have an energy greater than the threshold energy $E_T = 200$ MeV to remove false matches due to noise in the electronics. This value was obtained by fitting a Gaussian function to the noise peak in the energy spectrum at $E = 0$ GeV and excluding energies within 5σ .

The Moliere radius for electrons in lead is $R_M \sim 1.6$ cm, and electrons will deposit $\sim 95\%$ of their shower in a cylinder of radius $2R_M$. At midrapidity, the BEMC tower size is $\sim 10 \times 10\text{cm}^2$, and electrons that strike near the center of a tower will deposit their entire energy into a single tower. While electrons that hit near the edge of a tower may deposit their energy in more than one tower. The clustering of neighboring towers in the BEMC is an effective tool in reconstructing the electron energy in a low occupancy environment. However, due to the high background rates in Au+Au collisions, this method can over-estimate the energy of low- p_T electrons. Instead, only a single tower, which has the most deposited energy in the cluster, was used to determine the energy in Au+Au.

The event selection, track quality and electron identification (EID) requirements are summarized in Table III.

32 E. Efficiency and Acceptance

The total J/ψ efficiency and acceptance was determined by combining the electron tracking efficiency and acceptance with the electron identification efficiencies using a toy model. The details will be described as bellow.

36 1. TPC tracking efficiency and acceptance

In order to determine the TPC tracking efficiency and acceptance, Monte Carlo J/ψ s were embedded and decayed into real events. A GEANT simulation was used to determine the interaction of the electron daughters with the detector material, after which the TPC Response Simulator was used to model the ionization energy and detector response. The embedding was performed using production P11id and library SL11d_embed. Flat input spectra for the Monte Carlo J/ψ transverse

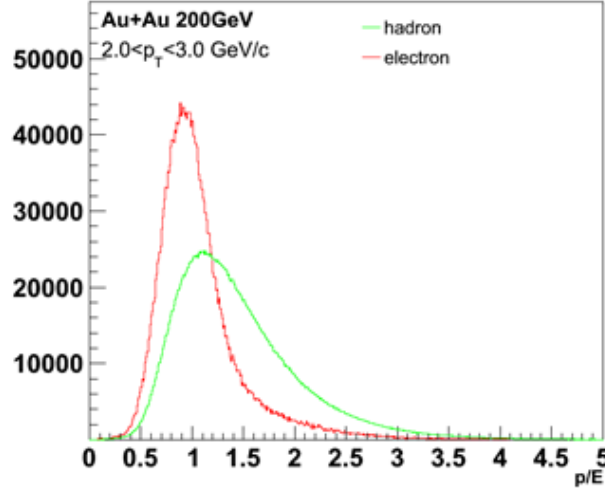


FIG. 6. p/E distribution for electron sample and hadron sample in 200 GeV Au+Au collisions taken in 2010.

Event Cut Parameters	Cuts Value
Trigger Ids	350003 or 350013 or 350023 or 350033 or 350043
Valid vertex	$ V_x(TPC) > 10^{-5} \text{cm}$ or $ V_y(TPC) > 10^{-5} \text{cm}$ or $ V_z(TPC) > 10^{-5} \text{cm}$
Vertex correlation	$ V_z(TPC) - V_z(VPD) < 4\text{cm}$
V_z	$ V_z(TPC) < 30\text{cm}$
$V_r = \sqrt{V_x^2 + V_y^2}$	$ V_r(TPC) < 2\text{cm}$

Track quality cuts	Cuts value
Transverse Momentum	$p_T > 0.2\text{GeV}/c$
Pseudorapidity	$ \eta < 1.0$
Track Flag	$flag > 0$ and $flag < 1000$
Spatial Hits	$nHitsFit >= 25$
dE/dx Hits	$nHitsDedx >= 15$
$dca (p > 1.5\text{GeV}/c)$	$dca < 1\text{cm}$
$dca (p < 1.5\text{GeV}/c)$	$dca < 3\text{cm}$

EID cuts	Cuts value
$1/\beta (p < 1.5\text{GeV}/c)$	$ 1/\beta - 1 < 0.03$
$p/E (p > 1.5\text{GeV}/c)$	$0.3 < p/E < 1.5$
$n\sigma_e$	$-1 < n\sigma_e < 2$

TABLE III. analysis cuts for Run11 200 GeV Au+Au collisions

mommentum, ϕ and rapidity distributions were used to reduce CPU time and increase statistics at higher p_T . The input J/ψ p_T , ϕ and rapidity distribution are shown in Fig.7. And the p_T , ψ and rapidity distribution of the decayed electron daughters are shown in Fig.8

The Monte Carlo electron daughters that pass through the TPC acceptance and were reconstructed by the tracking software were subjected to the same track quality requirements as the real data. Since the dE/dx can not be reproduce very well in embedding, we get the dE/dx distribution from data. For $nHitsDedx$ cut efficiency, we also got it from data.

The embedding request can be found at:

<http://www.star.bnl.gov/HyperNews-star/protected/get/heavy/3916.html>

The QA plots of embedding can be found at:

http://www.star.bnl.gov/protected/heavy/Wangmei/PaperProsal_62_39/support/embeddingQA.pdf

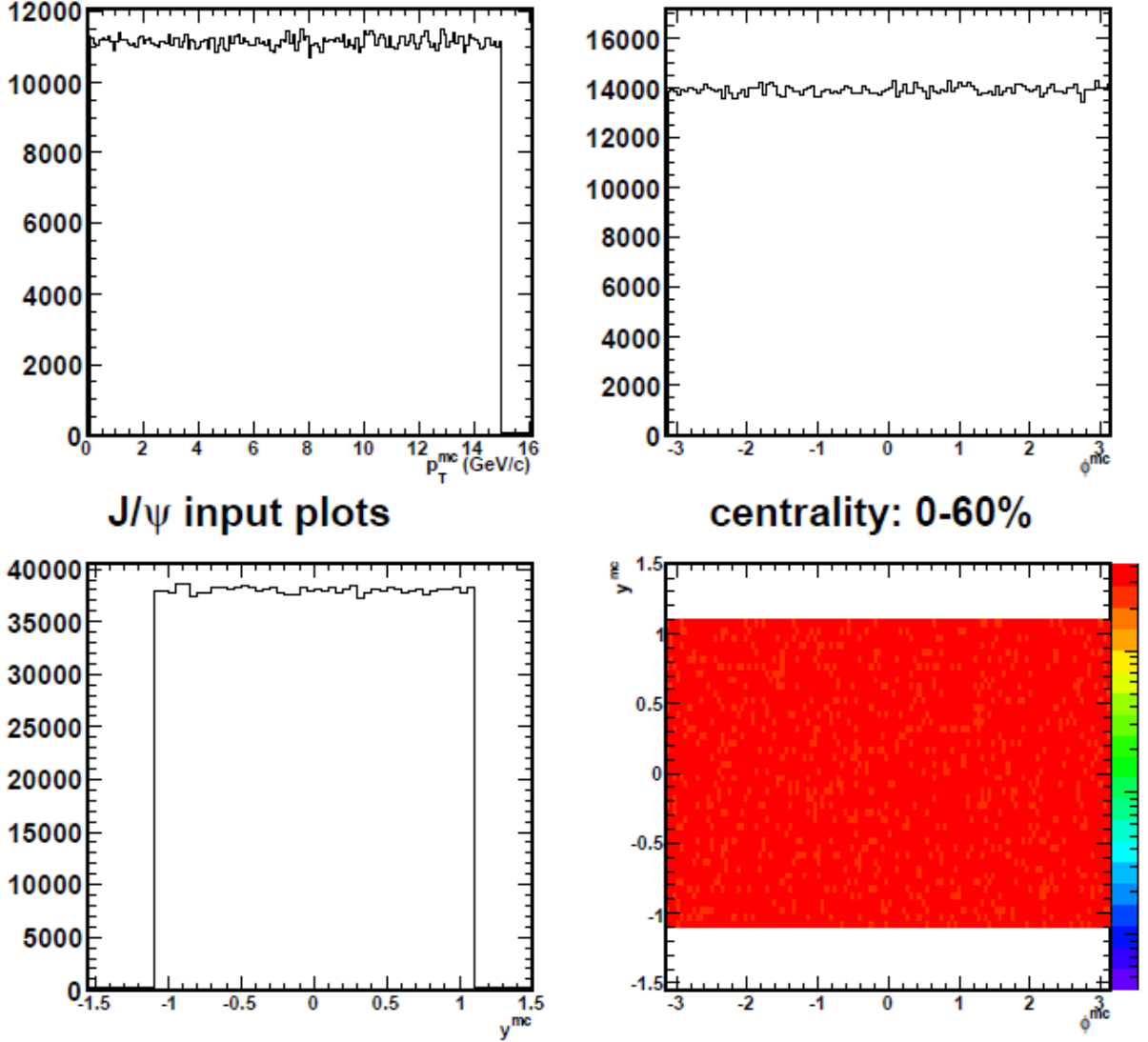


FIG. 7. The input J/ψ p_T , ϕ and rapidity distribution

- 1 Figure 9 shows the electron daughters efficiency as a function of MC p_T after cuts listed bellow:
- 2 a) $n\text{HitsFit} \geq 25$
- 3 b) $dca < 3$ cm

4

2. Momentum resolution

5 The momentum resolution and bremsstrahlung radiation energy loss are also obtained from the
6 embedding. We separate them into transverse momentum p_T . Figure 10 shows the ratio of recon-
7 strcuted p_T and MC p_T , $p_T^{\text{RC}}/p_T^{\text{MC}}$, distributions in different p_T bins. The integral of the histograms
8 are normalized to 1. The Gaussian peaks around 1 are due to p_T resolution and the long tails on the
9 left side are due to bremsstrahlung radiation energy loss. The p_T smearing is strongly dependent

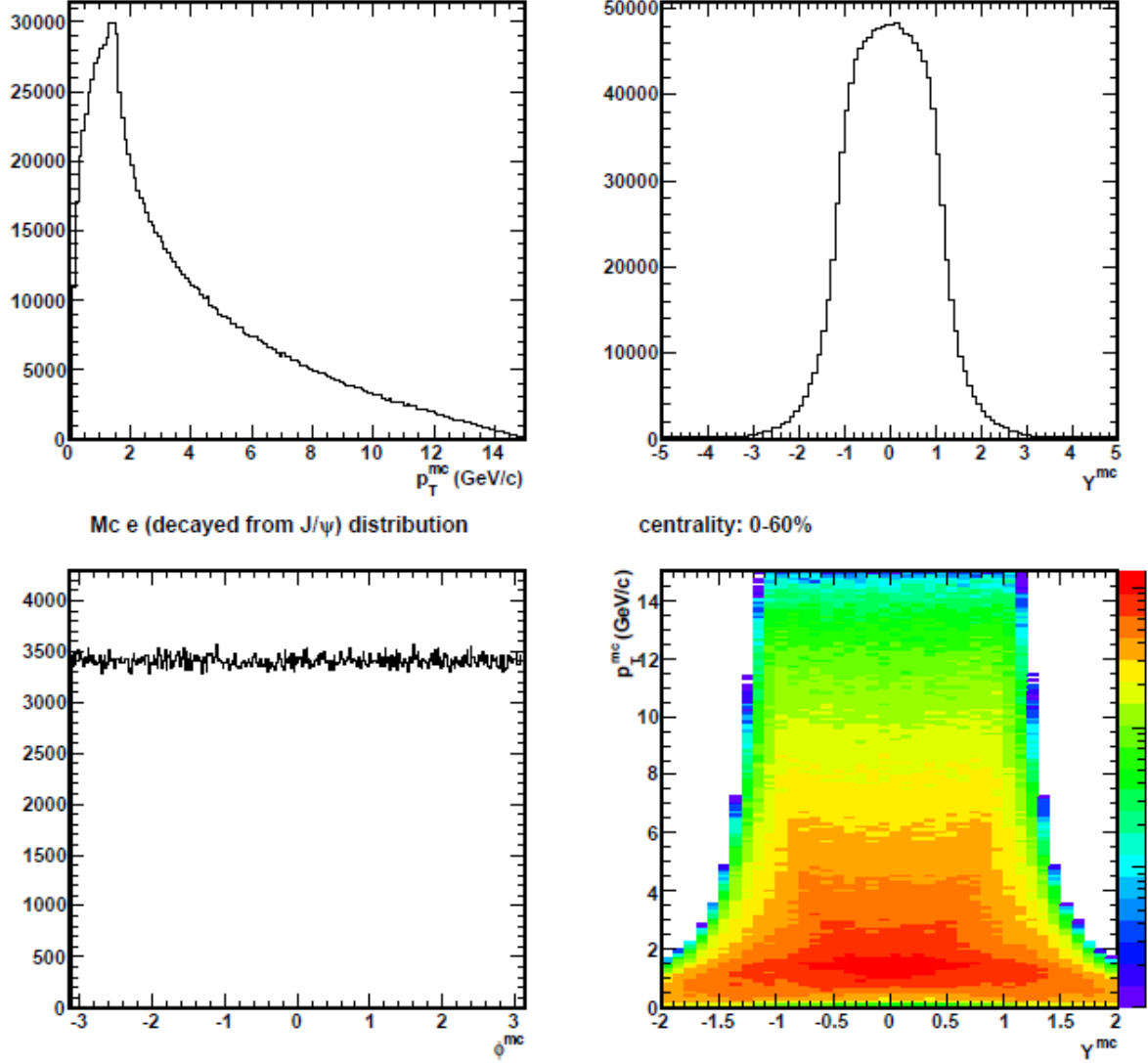


FIG. 8. The electron daughters p_T , ϕ and rapidity distribution

on p_T . Figure 11 shows the distribution of the difference of reconstructed η and its corresponding MC η , $\eta^{RC} - \eta^{MC}$, in different p_T bins. The smearing is quite small, on the order of 0.01. The dependence on p_T is small. Figure 12 shows the distribution of the difference of reconstructed ϕ and its corresponding MC ϕ , $\phi^{RC} - \phi^{MC}$, in different p_T bins. The smearing is even smaller, on the order of 0.01. It has small dependence on p_T .

3. BEMC cuts efficiency

Electron candidates in the TPC are projected to the BEMC and matched to an energy cluster to determine their momentum-to-energy ratio p/E . In Au+Au, the highest energy tower in the energy cluster matched was used to remove background.

The same methods of matching tracks to the BEMC was performed in simulation. Monte Carlo electrons were embedded into real data events and propagated through the detector using a GEANT

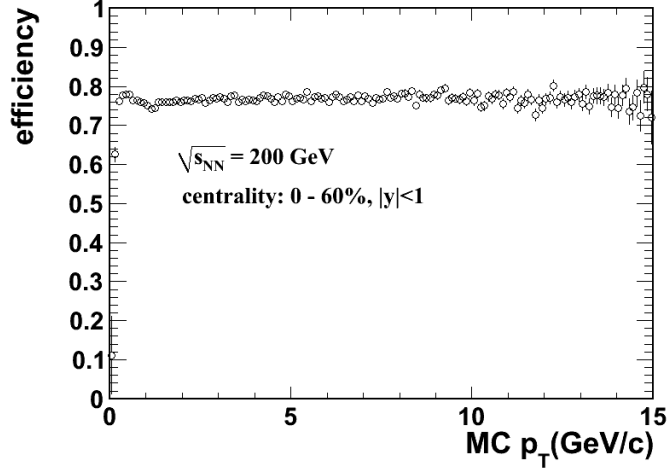


FIG. 9. Electron daughters efficiency as a function of MC p_T

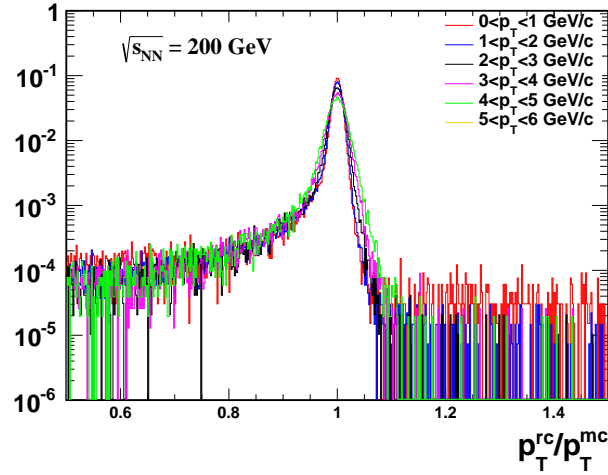


FIG. 10. The p_T^{rc}/p_T^{mc} distribution of electrons in different p_T bins for Au+Au 200GeV.

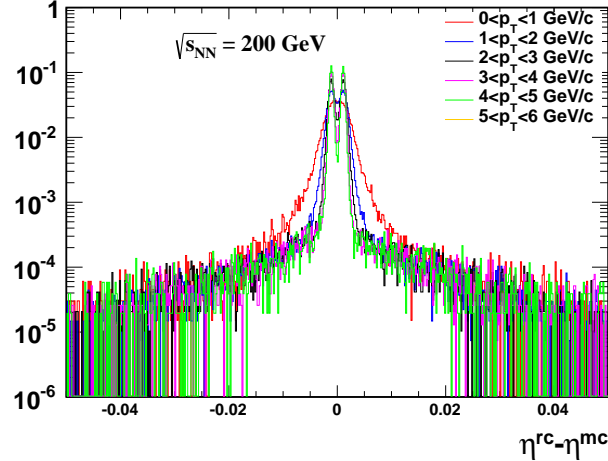


FIG. 11. The $\eta^{rc} - \eta^{mc}$ distribution of electrons in different p_T bins for Au+Au 200GeV.

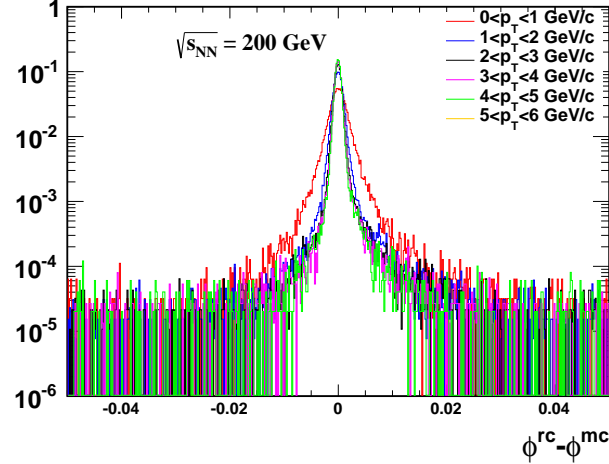


FIG. 12. The $\phi^{rc} - \phi^{mc}$ distribution of electrons in different p_T bins for Au+Au 200GeV.

simulation. The tracks reconstructed from the Monte Carlo electrons were matched to the BEMC to determine the detector performance.

Figure 13 shows the electron efficiency as a function of MC p_T in $|\eta| < 1$ after TPC tracking, BEMC matching and cuts listed below ("TPC+EMC" electron efficiency):

- nHitsFit ≥ 25
- dca $< 1\text{cm}$
- $0.3 < p/\text{E} < 1.5$

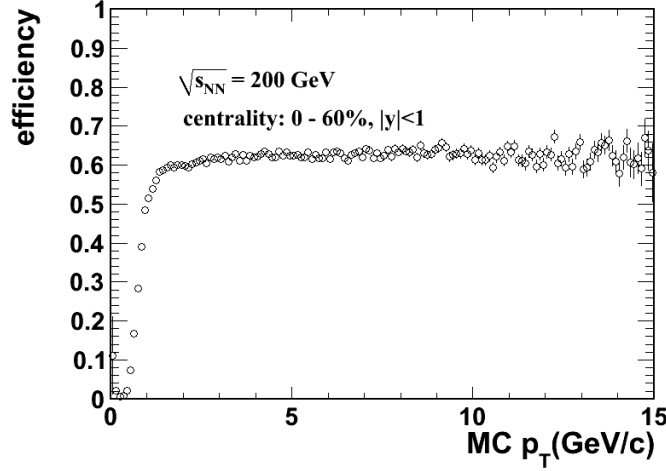


FIG. 13. The "TPC+EMC" electron efficiency as a function of MC p_T in midrapidity at centrality 0- 60%

4. TOF cuts efficiency

The TOF conditions are not well simulated in the embedding so efficiencies of the TOF cuts have to be calculated from data. The efficiency of matching a track to the TOF in $Au + Au$ collisions was obtained from a high purity sample of electrons (photonic electron sample) from data by requiring

$m_{ee} < 10 MeV/c^2$. The TOF matching efficiency for electrons is calculated as a number of electrons that match to the TOF divided by a number of electrons in the TPC (N_{TPC}^e) that passed the track quality and acceptance cuts:

$$\epsilon_{TOF\text{ matching}} = \frac{N_{TOF}^e}{N_{TPC}^e} \quad (2)$$

The $1./\beta$ cut efficiency is also extracted using the photonic electron sample. The TOF matching efficiency and $1./\beta$ cut efficiency as a function of p_T is shown in Fig.14.

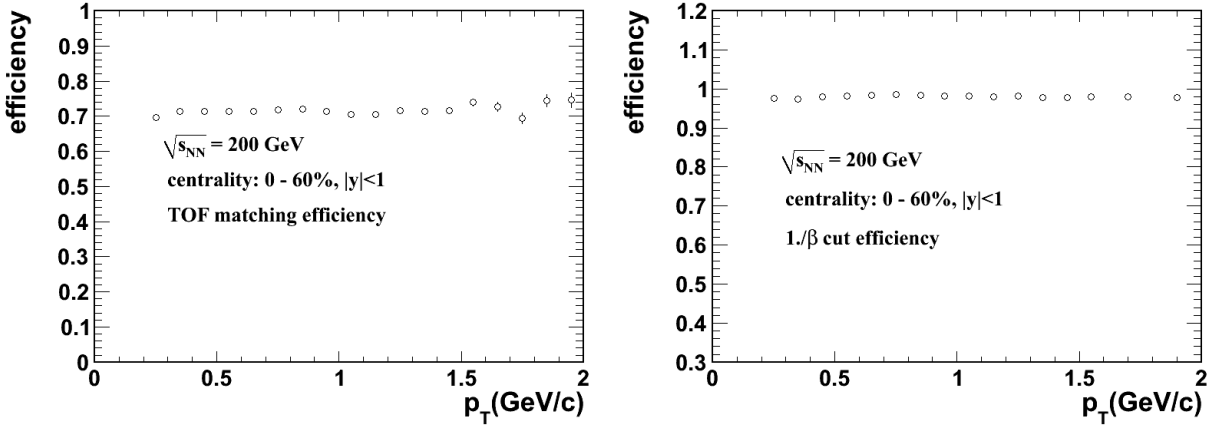


FIG. 14. The TOF matching efficiency and $1./\beta$ cut efficiency verse p_T .

5. $n\sigma_e$ cuts efficiency

Since the dE/dx can not be reproduced very well in embedding, we get the $n\sigma_e$ distribution from data. After enhancing the electron contribution in the $n\sigma_e$ distribution by using the TOF and selecting photonic electrons, a Gaussian + exponential fitting was performed to the $n\sigma_e$ distribution to determine the shape of the electron contribution. Fig.15 shows the $n\sigma_e$ distribution for $0.2 < p_T < 0.3 \text{ GeV}/c$ in Au+Au collisions and the $n\sigma_e$ cut efficiency as a function of p_T .

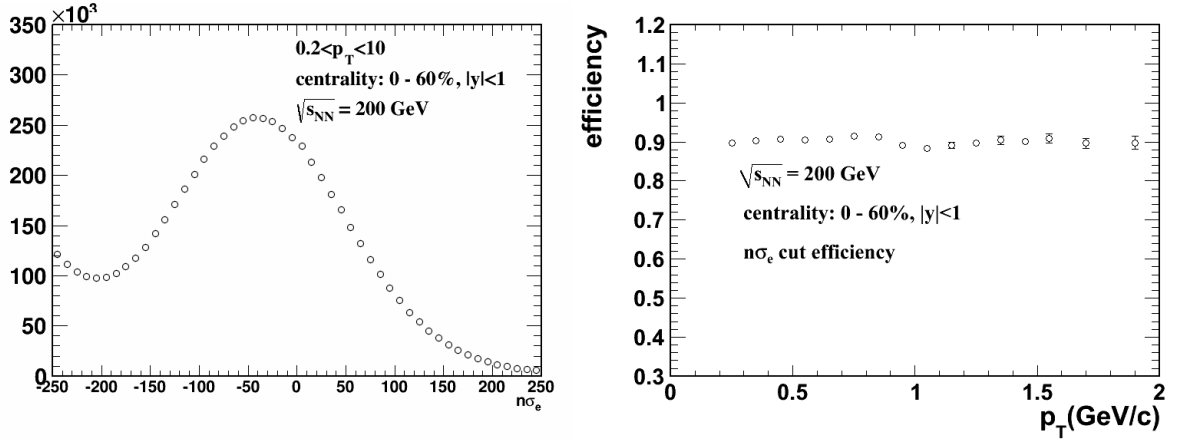
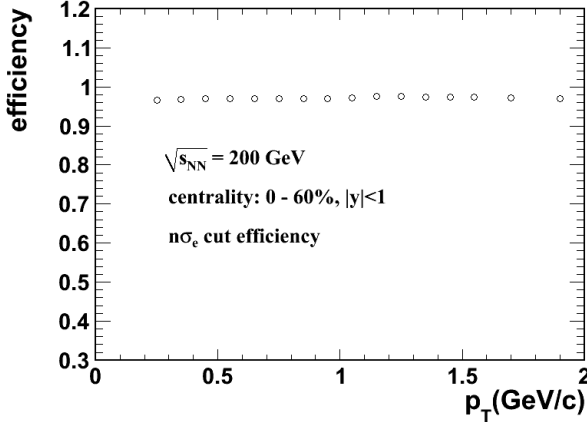


FIG. 15. The $n\sigma_e$ distribution for electrons with $0.2 < p_T < 0.3 \text{ GeV}/c$ (left panel) and the $n\sigma_e$ cut efficiency as a function of p_T (right panel).

1 6. *nHitsDedx cuts efficiency*

2 The $n\text{HitsDedx} \geq 15$ cut efficiency is obtained from the photonic electron sample. We compared
 3 the number of electron candidates with and without this $n\text{HitsDedx}$ cut after the basic tracking
 4 quality cuts the same as we used in the analysis. The efficiency as a function of p_T is shown in
 5 Fig.16.



6 FIG. 16. The $n\text{HitsDedx}$ cut efficiency as a funcion of p_T .

7

8 F. *Total J/ψ detection efficiency*

9 After getting the detection efficiencies for the decay electrons, the J/ψ detection efficiency is then
 10 determined by folding the efficiencies of the decay electrons using the J/ψ decays kinematics. We
 11 wrote a toy model follow almost the same methods, which used in Au+Au 200GeV analysis, to
 12 calculate the total J/ψ detection efficiency.

13 The p_T and centrality dependence of the total J/ψ efficiency correction in Au+Au collisions are
 14 shown in Fig. 17. The efficiency increases with p_T and decreases in more central collisions. The
 15 total efficiency and acceptance corrections have been used to correct the measured J/ψ p_T spectrum
 16 to determine the invariant J/ψ yield. The J/ψ signal and invariant yield in $Au + Au$ collisions are
 17 describe in the following chapter.

18 G. *J/ψ signal and invariant yield*

19 The reconstruction of J/ψ has been performed in Au+Au collisions at STAR via the dielectron
 20 decay channel:

$$21 \quad J/\psi \rightarrow e^+ + e^- (\mathcal{B} = 5.94 \pm 0.06\%),$$

22 where \mathcal{B} is the branching ratio of the J/ψ decay to dielectrons.

23 The dielectron invariant mass spectrum is presented below, followed by a description of the J/ψ
 24 yield extraction and efficiency correction. Finally, the J/ψ invariant p_T spectrum is presented.

25 1. *J/ψ signal*

26 Electron pairs that originate from the collision vertex within the same event have been used to
 27 reconstruct the dielectron invariant mass spectrum. Like-sign pairs ($e^+ + e^+$ and $e^- + e^-$) have been

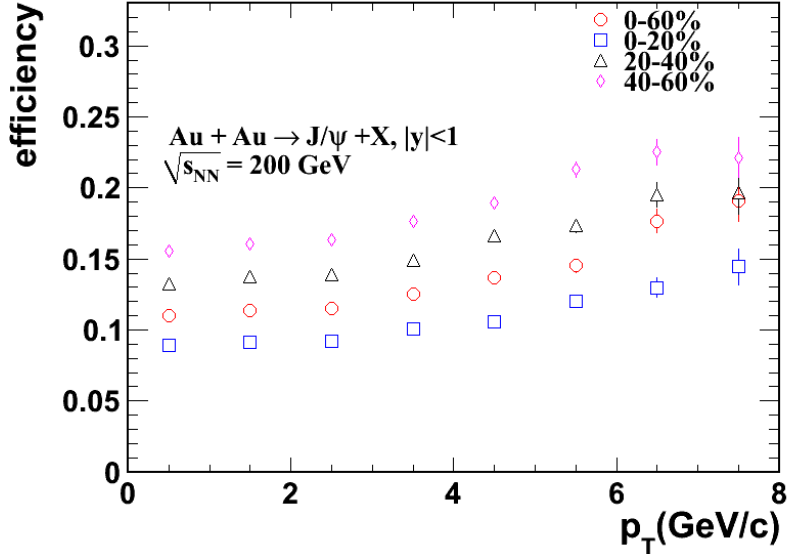


FIG. 17. The J/ψ total efficiency versus p_T for various centrality bins in Au+Au collisions.

used to estimate the background from random combinations of opposite-sign pairs ($e^+ + e^-$). The number of background (combinatorial) pairs, N_{BG} , is calculated using the geometric mean of the like-sign pairs:

$$N_{BG} = 2\sqrt{N_{++} \times N_{--}} \quad (3)$$

where N_{++} (N_{--}) is the number of the $e^+ + e^+$ ($e^- + e^-$) pairs. The statistical uncertainty in the background contributes to the uncertainty in the J/ψ signal, and to minimize this, a mixed-event background calculation was used in Au+Au collisions. The mixed-event background was obtained by mixing opposite-sign electron pairs from different events with similar event conditions such as collision centrality and vertex position. The vertex position were divided into 20 bins and the event centrality into 10bins to ensure that the mixing was done between tracks from similar events. All combinations of opposite sign pairs in a given collision centrality and V_z range were used to reconstruct the mixed-event background. This process was repeated across the entire data set, providing a significant increase in the statistics used in the mixed-event background compared to the like-sign background. The mixed-event background requires a normalization factor, and this was obtained by normalizing to the like-sign background in the range $2.6 < m_{ee} < 3.6 \text{ GeV}/c^2$. The amount of background is quantified using the signal-to background ratio, S/B , where $S = N_{J/\psi} = N_{+-} - N_{BG}$ and $B = N_{BG}$. The signal strength is defined by it's significance, $S/\sqrt{(S+B)}$.

The dielectron invariant mass spectrum for $|y| < 1$ and $p_T < 5 \text{ GeV}/c$ in Au+Au collisions i shown in Fig 18 for minimum bias triggered data in 0 – 60% central collisions. The like-sign (upward triangles) and mixed-event (downward triangles) background are shown, and a strong signal-to background ratio has been achieved using TPC, TOF, and BEMC, with $S/B = 0.11$ in 0 – 60%. The dielectron mass spectrum in 0 – 20% and 40 – 60% central Au+Au collisions is shown in Fig 19 to illustrate the centrality dependence of background, which decreases in more peripheral collisions. The like-sign (upward triganles) and mixed-event (downward triangles) background are shown, and the improvement in the statistical uncertainty of the mixed-event background can be clearly seen in 40 – 60% central collisions.

The combinatorial background has been subtracted from the opposite-sign dielectron invariant

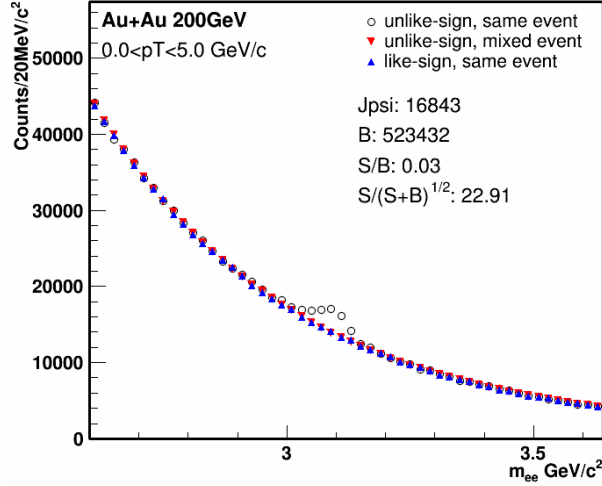


FIG. 18. The dielectron mass spectrum in 0 – 60% central Au+Au collisions.

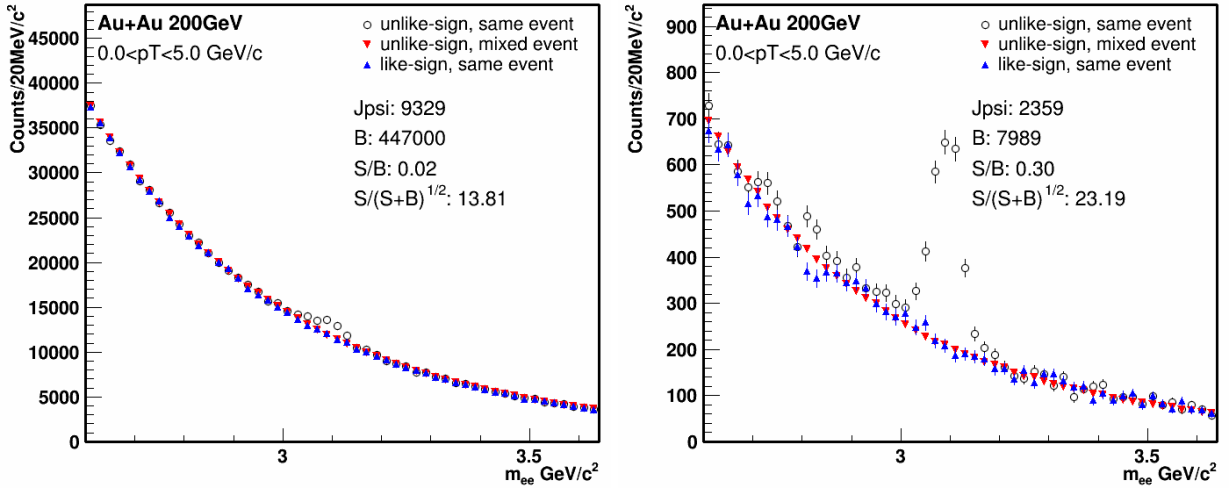
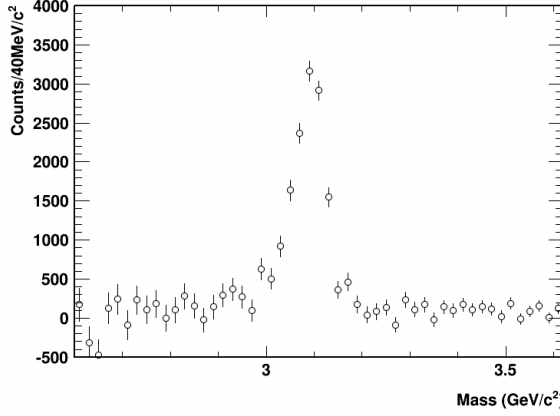
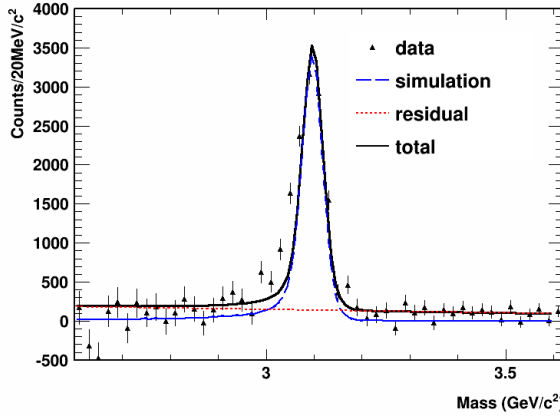


FIG. 19. The dielectron mass spectrum in 0 – 20% central (left) and 40 – 60% central (right) Au+Au collisions.

mass spectrum to obtain the J/ψ signal. This is shown for $|y| < 1$ and $p_T < 5\text{GeV}/c$ in 0 – 60% central Au+Au collisions in Fig 20.

The J/ψ signal shape was determined from simulation by embedding Monte Carlo J/ψ s into real data, and results from momentum resolution of the TPC and the radiative energy loss of electrons (Bremsstrahlung) interacting with the material in the detector. The J/ψ signal shape from simulation has been fitted to the dielectron mass spectrum after background subtraction to determine the J/ψ , and has been combined with a straight line to account for residual background contributions from $c\bar{c}$ and Drell-Yan.

The invariant mass distribution of the J/ψ signal obtained from the embedding (the J/ψ lineshape) is shown in Fig 21, along with the J/ψ signal from the data, for $0 < p_T < 5.0\text{GeV}/c$. One can see that the J/ψ signal from the simulation is narrower than the J/ψ signal obtained from the data. Observed in the experiment width of the J/ψ signal depends on the STAR detector resolution. The smaller width of the J/ψ signal in the embedding from the width of the signal in the data suggests that the TPC resolution is not well simulated in the embedding. An additional, Gaussian smearing on the p_T is applied in order to reflect the detector conditions in the simulation. To the p_T resolution

FIG. 20. The J/ψ signal in 0 – 60% central Au+Au collisions.FIG. 21. The J/ψ signal after the combinatorial background subtraction with the J/ψ lineshape from embedding (without applying additional smearing on the embedding momentum).

from the embedding an additional Gaussian component is added, the Gaussian parameters are:

- mean: $\mu = 0$
- width: $\sigma_A = A \times p_T$

where A is a smearing parameter.

To find the best value of the smearing parameter, a χ^2 minimization is done. J/ψ signal from the simulation with the additional smearing of p_T is compared to the J/ψ signal from the data and χ^2 is determined, for each A value from 0 to 1% with 0.01% interval. Then the best value of the A is determined by finding a minimum of the χ^2 distribution as a function of A . The J/ψ signal from the data and the embedding are compared at $0 < J/\psi p_T < 5\text{GeV}/c$, the whole used in the analysis p_T range. The smearing parameter for χ^2_{min} : $A = 0.61\%$. The χ^2 minimization was also done for narrower $J/\psi p_T$ bins used in the analysis: $0 < p_T < 1\text{GeV}/c$, $1 < p_T < 2\text{GeV}/c$, $2 < p_T < 3\text{GeV}/c$, $3 < p_T < 4\text{GeV}/c$, $4 < p_T < 5\text{GeV}/c$. Although, a small smearing parameter dependence of p_T was observed which could be due to statistical fluctuations effects. In order to avoid fluctuations effects one value of smearing parameter for the whole $J/\psi p_T$ range was applied in the embedding analysis. The J/ψ signal with additional smearing of the p_T of 0.61% p_T is shown in Fig. 22. The counting method in mass window (2.7 - 3.2) GeV/c^2 with residual background subtraction (straight

¹ line fitting for residual background) has been set as default method.

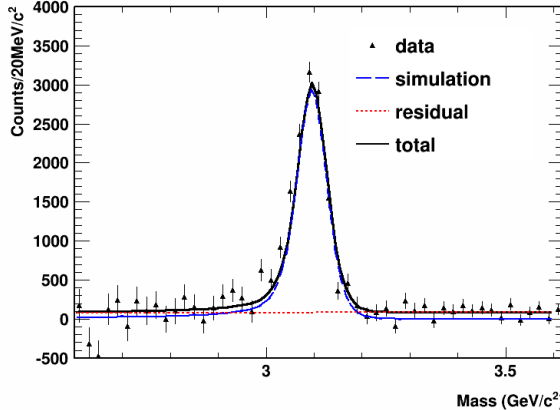


FIG. 22. The J/ψ signal after the combinatorial background subtraction with the J/ψ lineshape from embedding (with additional p_T smearing of 0.61% p_T).

² A total of 16843 J/ψ s have been reconstructed in minimum bias 0–60% central Au+Au collisions,
³ with a signal significance of 22.91σ . The final J/ψ yield in $|y| < 1$ and $p_T < 5\text{GeV}/c$ has been
⁴ extracted as a function of transverse momentum and collision centrality by counting the entries in
⁵ $2.7 < m < 3.2\text{GeV}/c^2$ in the dielectron mass spectrum after background subtraction. The signal
⁶ shape combined with straight line has been fitted to the data to account for any residual background,
⁷ and the residual background has been subtracted from the count entries in the given mass range.
⁸ The yield can also extracted from the integral of fitted J/ψ line shape in the same mass range for
⁹ comparison. The J/ψ raw signal, signal-to-background ratio, and significance obtained in each p_T
¹⁰ bin are summarized in Table IV.

Centrality (%)	p_T (GeV/c)	$N_{J/\psi}$	S/B	$S/\delta S$
0-60	0-1	4739	0.03	11.27
	1-2	6875	0.03	14.16
	2-3	3675	0.03	11.06
	3-4	1309	0.03	6.57
	4-5	691	0.06	6.25

TABLE IV. The J/ψ uncorrected signal $N_{J/\psi}$, signal-to-background ratio S/B and significance $S/\delta S$ obtained in 200 GeV Au+Au collisions

¹¹

¹²

¹³

2. J/ψ invariant p_T spectrum

¹⁴ To obtain the J/ψ invariant p_T spectrum, the J/ψ yield has been corrected using the efficiency in
¹⁵ Fig 17, and normalized to the number of events and phase space used in the analysis. The invariant
¹⁶ p_T spectrum is defined as:

$$\mathcal{B} \frac{d^3N}{p_T dp_T dy d\phi} = \frac{1}{2\pi p_T} \frac{N_{J/\psi}}{\Delta p_T \Delta y} \frac{1}{\epsilon \times a} \quad (4)$$

¹⁸ where $\Delta y = 2$ for $|y| < 1$, p_T is the mean transverse momentum in a bin of width Δp_T , and $\epsilon \times a$
¹⁹ is the efficiency and acceptance correction.

²⁰ The J/ψ p_T spectrum for different centrality bins in Au+Au collisions is shown in Fig. 23. The
²¹ comparison with published results can be found in Appendix Fig. 72.

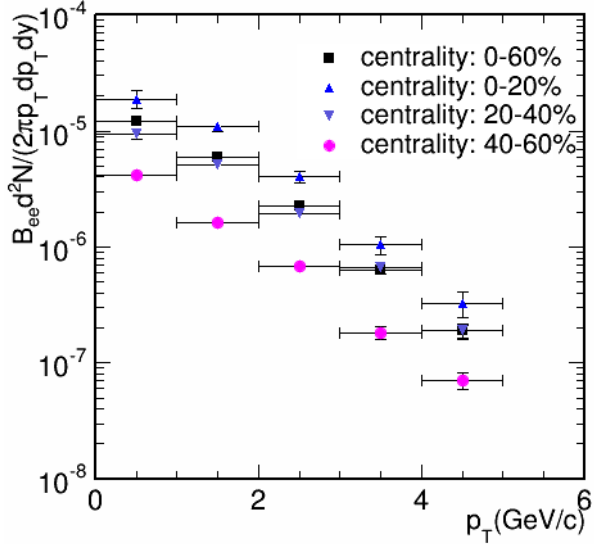


FIG. 23. The invariant yield versus transverse momentum for $|y| < 1$ in 0 – 20%, 20 – 40%, 40 – 60%, and 0 – 60% centrality in Au+Au collisions.

H. Systematic uncertainty estimation

The primary sources of uncertainty in the data analysis, yield extraction, and efficiency correction for J/ψ in Au+Au collisions are described in the belowing.

1. Tracking efficiency

We studied the daughter particle (electron) tracking efficiencies from embedding. The daughters tracking efficiencies depend on the cuts of Dca and number of fit points (nHitsFit). Figure 24 and Fig. 25 shows the dca and nHitsFit distribution, for one p_T bins for embedding in green and the data in red. The distributions were obtained from a pure electron sample by selecting photonic electrons.

There is some discrepancy between the data and the embedding in nHitsFit and dca distributions. The difference between data and embedding introduces the efficiency uncertainties. We studied the dca and nHitsFit distributions in volume.

We define the unit area under the distributions as dA , the total integrated area of the distribution is A . Then the cut efficiency is define as:

$$Eff_{dcacut1} = \frac{\int_{dca=0}^{dca=1} dA}{A}; Eff_{dcacut2} = \frac{\int_{dca=0}^{dca=3} dA}{A}. \quad (5)$$

The relative uncertainty thus can be calculated as:

$$\sigma_{dca} = \frac{\int_{dca=0}^{dca=1} dA_{data}/Eff_{dcacut1}^{emb}}{\int_{dca=0}^{dca=3} dA_{data}/Eff_{dcacut2}^{emb}} \quad (6)$$

σ_{dca} as a fuction of p_T is shown in Fig. 26 for 0 – 60% most central bin in Au+Au collisions. The relative uncertainty was applied to the total J/ψ efficiency calculation to extract the uncertainty.

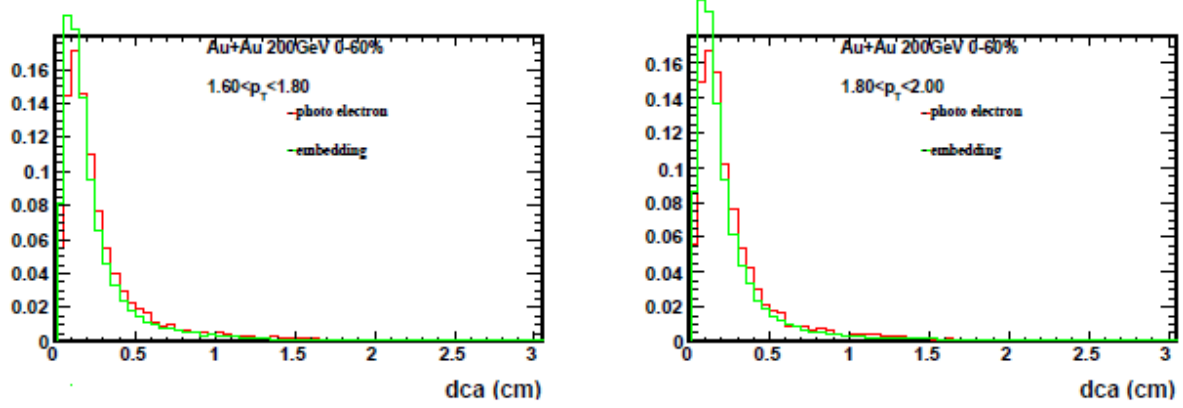


FIG. 24. Electrons dca distributions from the embedding in green and the data in red in 0 – 60% centrality bin. The left panel is for $1.6 < p_T < 1.8 \text{ GeV}/c$ and the right panel is for $1.8 < p_T < 2.0 \text{ GeV}/c$

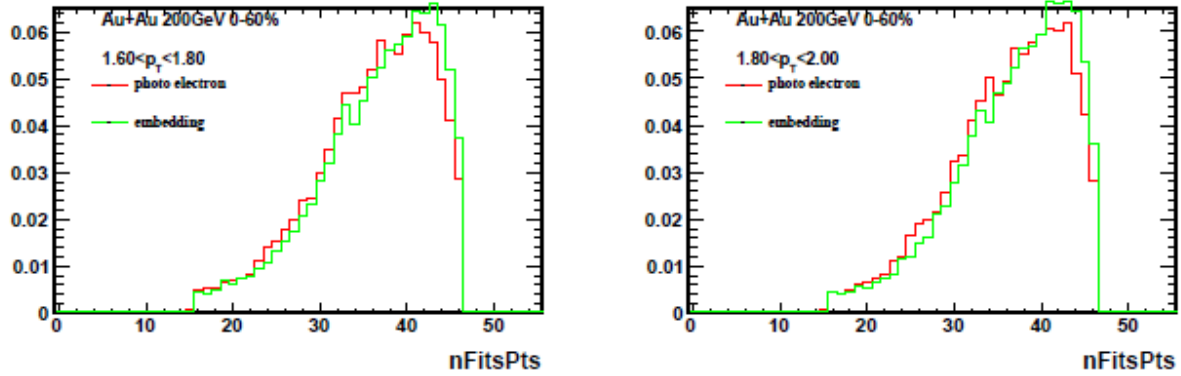


FIG. 25. Electrons nHitsFit distributions from the embedding in green and the data in red in 0 – 60% centrality bin. The left panel is for $1.6 < p_T < 1.8 \text{ GeV}/c$ and the right panel is for $1.8 < p_T < 2.0 \text{ GeV}/c$

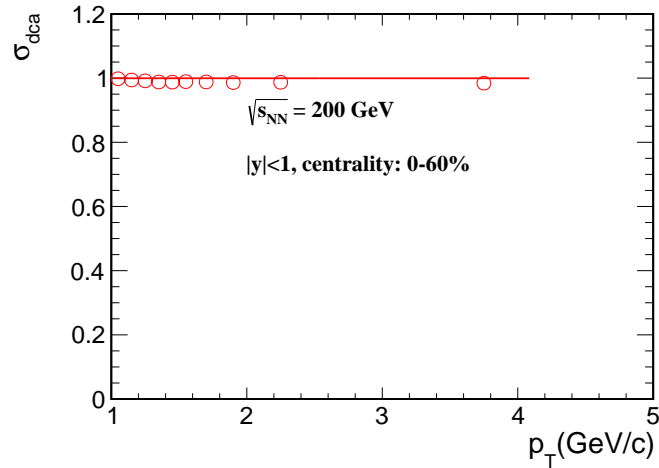


FIG. 26. σ_{dca} verse p_T for centrality: 0 – 60% in Au+Au collisions.

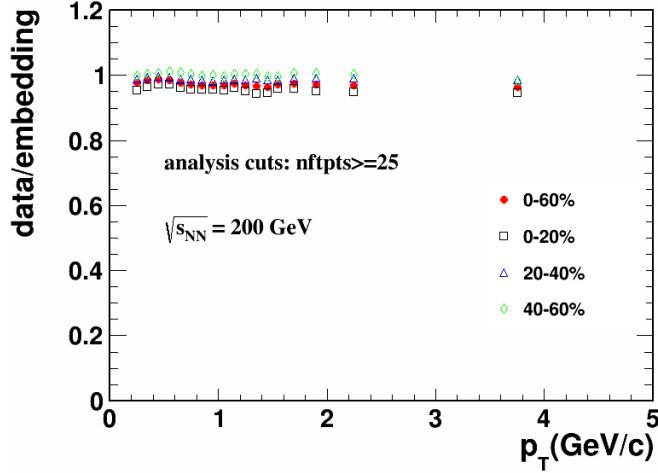


FIG. 27. $\sigma_{n\text{HitsFit}}$ verse p_T for different centrality bins in Au+Au collisions.

1 The systematic uncertainties of nHitsFit are also estimated in the same way. And Fig. 27 shows
2 the $\sigma_{n\text{HitsFit}}$ as a function of p_T for Au+Au collisions in different centrality bins.

3 The systematic uncertainties associated with dca and nHitsFit verse transverse momentum are
4 shown in Table V.

p_T range (GeV/c)	0 – 1	1 – 2	2 – 3	3 – 4	4 – 5
dca cuts systematic uncertainties (%)	0.73	1.10	1.80	4.28	1.88
nHitsFit cuts systematic uncertainties (%)	3.54	4.07	5.31	4.51	8.05

TABLE V. The systematic uncertainties associated with dca and nHitsfit cut.

5 2. $n\sigma_e$ cut efficiency

6 The uncertainty associated with the electron dE/dx identification efficiency can be separated into
7 several components, and these are discussed below.

8 • Fit Constraints. In order to determine the $n\sigma_e$ distribution form photonic electron samples,
9 a exponential + guassian is fitted to account for the electrons and merged hadrons. There is
10 some ambiguity in the fitting in regions. We change the fit range and it results in uncertainties
11 less than 1%.

12 • Momentum dependence. The mean and width of the electron $n\sigma_e$ distributions in Au+Au
13 exhibit a momentum dependence, which may be due to calibration effects, or from a residual
14 hadron contamination underneath the electron peak that is not removed by photonic electron
15 requirements. To understand this effect, the mean and width were assumed to be constant,
16 and fitted with a constant function in the range $0.2 < p_T < 5\text{GeV}/c$. The efficiency calculated
17 using the corresponding constant mean and width resulted in a change in the final yield. And
18 the change has been considered as a source of the uncertainties associated with the $n\sigma_e$ cut.

19 The systematic uncertainties associated with the electron dE/dx identification efficiency verse trans-
20 verse momentum are shown in Table VI.

p_T range (GeV/c)	0 – 1	1 – 2	2 – 3	3 – 4	4 – 5
$n\sigma_e$ cuts systematic uncertainties (%)	0.72	0.95	0.22	1.55	1.87

TABLE VI. The systematic uncertainties associated with $n\sigma_e$ cut.

3. TOF matching efficiency

The TOF matching efficiency was obtained from the data using photonic electron sample. The uncertainties associated with TOF matching efficiency include the pile-up track effect and the lack of statistics. To determine the uncertainty on the efficiency, the final yield were also obtained using the hadron efficiency. In order to remove the pile-up effect, the hadron efficiency was scaled up to match the hadron TOF matching efficiency with EMC match (described in formula 7) at p_T range: $> 2GeV/c$. The changes in final yield is about $\sim 0.1\%$, which has been included in the systematics.

$$\epsilon_{TOF \text{ with } BEMC \text{ match}} = \frac{N_{BEMC \wedge TPC \wedge TOF}}{N_{BEMC \wedge TPC}} \quad (7)$$

4. $1/\beta$ cut efficiency

The $1/\beta$ cut efficiency was calculated by determining the fraction of electrons with $|1/\beta - 1| < 0.03$. This was done by obtaining a high-purity electron sample (photonic electrons) and counting the entries in $|1/\beta - 1| < 0.03$ (shown in formula 8). The efficiency was also estimated by fitting a Gaussian function to the $1/\beta$ distribution to remove any non-Gaussian contributions to the tails of the distribution from hadron contamination. These different methods result in an uncertainty of 2%.

$$\epsilon_{1/\beta \text{ efficiency}} = \frac{N_{counts \text{ in } 0.97 < 1/\beta < 1.03}}{N_{counts \text{ in } 0.9 < 1/\beta < 1.1}} \quad (8)$$

5. BEMC matching and cut efficiency

The uncertainty due to the BEMC was primarily from the disagreement between simulation and data. The matching and p/E cut efficiency from simulation and data are compared in Fig. 28 for Au+Au collisions. The uncertainty from the BEMC is obtained by comparing the results obtained from simulation and data. The systematic uncertainties associated with BEMC cuts efficiency versus transverse momentum are shown in Table VII.

p_T range (GeV/c)	0 – 1	1 – 2	2 – 3	3 – 4	4 – 5
BEMC cuts systematic uncertainties (%)	0.29	2.46	1.33	1.35	0.50

TABLE VII. The systematic uncertainties associated with BEMC cuts.

6. Yield extraction

The J/ψ yield was obtained by subtracting a combinatorial background form the opposite sign dielectron mass spectrum, and fitting this with a signal shape obtained from simulation. The uncertainties associated with this describe below.

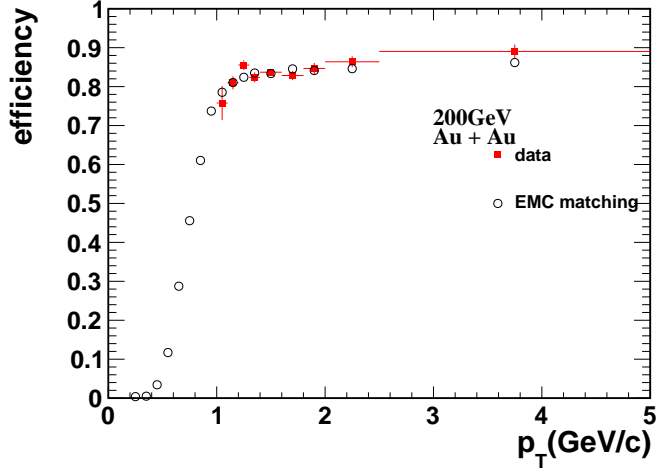


FIG. 28. The matching and p/E cut efficiency from simulation and data for Au+Au 200GeV.

- The yield was also obtained by counting the number of entries in the dielectron mass spectrum in the range $2.7 < m_{ee} < 3.2 \text{GeV}/c^2$ after background subtraction. The number of counts was corrected using the fraction of J/ψ s outside of this mass range, which was determined using the signal shape from simulation. This was compared to the results obtained from fitting the signal shape from simulation to the mass spectrum, and results in an uncertainty of 2% in Au+Au, depending on p_T and collision centrality.
- A mixed-event background was used in Au+Au and has been fitted to the like-sign background in the range $2.6 < m_{ee} < 3.6 \text{GeV}/c^2$. The fit range for the mixed-event background has been varied, and result in an uncertainty on the final yield in Au+Au of < 1%.
- An additional Gaussian smearing was applied to the momentum resolution in simulation to improve the fit quality between data and simulation in Au+Au collisions. The additional smearing factor was determined by performing a χ^2 minimization of the signal shape to the data. The uncertainty on smearing coefficient ($0.61 \pm 0.05\%$) was obtained from the χ^2 distribution and resulted in an uncertainty in the final yield in Au+Au of 1%.

The systematic uncertainties associated with yield extraction verse transverse momentum are shown in Table VIII.

p_T range (GeV/c)	0 – 1	1 – 2	2 – 3	3 – 4	4 – 5
systematic uncertainties associated with yield extraction (%)	5.53	9.41	7.63	10.58	5.76

TABLE VIII. The systematic uncertainties associated with yield extraction.

7. J/ψ internal radiation

The J/ψ mass is reconstructed via the $J/\psi \rightarrow e^+ + e^-$ channel, but J/ψ may also have radiate decay into lepton pair. The invariant mass of the dilepton will also have a long tail of the left hand side of the J/ψ mass due to the missing energy from the photon. This may modify the J/ψ line shape and affect the J/ψ yield within limit mass window. A detail reference on the J/ψ internal radiation can be found at [7]. This reference suggests that we can ignore the contribution on J/ψ

yield from the radiative decay if we do not apply any cut on the dielectron mass window (one should be aware that the J/ψ line shape is still affected by this effect). But in reality, we did apply a cut on the dielectron mass to count or fit for the extraction of J/ψ yield, this will reject some radiative decay and need to be corrected for the loss of signal. According to the theoretical calculation in this reference, the corresponding correction factor is around 4% for the mass cut ($2.7\text{-}3.2 \text{ GeV}/c^2$). We take it as a source of systematic uncertainty.

8. Summary of systematic uncertainty source

A summary of systematic uncertainties verse transverse momentum are shown in Table IX.

p_T range (GeV/c)	0 - 1	1 - 2	2 - 3	3 - 4	4 - 5
dca cuts (%)	0.73	1.10	1.80	4.28	1.88
nHitsFit cuts (%)	3.54	4.07	5.31	4.51	8.05
$n\sigma_e$ cuts (%)	0.72	0.95	0.22	1.55	1.87
TOF related cuts (%)	2.00	2.00	2.00	2.00	2.00
BEMC related cuts (%)	0.29	2.46	1.33	1.35	0.50
yield extraction (%)	5.53	9.41	7.63	10.58	5.76
radiative decay (%)	4.00	4.00	4.00	4.00	4.00
total for 0-60% (%)	8.05	12.33	10.41	13.35	11.18
total for 0-20% (%)	9.67	12.43	10.56	12.59	8.76
total for 20-40% (%)	8.13	12.76	9.85	12.28	10.29
total for 40-60% (%)	8.16	12.08	10.27	12.17	10.02

TABLE IX. The systematic uncertainties verse p_T for MB Au+Au 200GeV.

II. RUN 2010 AU+AU 62.4 AND 39 GEV ANALYSIS

A. Data sets and Triggers

This analysis uses the minimum bias (MB) Au+Au data recorded in 2010. The MB trigger IDs for Au+Au 62.4 GeV include 270001, 270011, 270021. The MB trigger IDs for Au+Au 39 GeV include 280001. The recorded number of events for the MB trigger in Au + Au collisions at 62.4 GeV and 39 GeV are shown in Figure 29. The data was produced in the production series P10ik usig library version SL10k.

B. Event Selection

The minimum bias trigger identifies collisions that occur within $|V_z| < 30\text{cm}$. The offline vertex position is determined by the vertex finding algorithm implemented for Au+Au collisions (MinuitVF). The VPD trigger is less efficient in low multiplicity collisions, which causes losses in peripheral Au+Au collisions. Only data in 0 - 60% central Au+Au collisions, where the VPD inefficiency is negligible, were used in this analysis. The left panel of Figure 30 and Figure 31 show the VPD V_z (called $V_z(\text{VPD})$) distribution in Au+Au collisions versus the reconstructed V_z obtained using MinuitVF (called $V_z(\text{TPC})$) at 62.4 GeV and 39 GeV, respectively. From the left panel of Fig. 30 and Fig. 31 , there is a very strong correlation between the $V_z(\text{VPD})$ and $V_z(\text{TPC})$ in most of the events, but there are some bad events which are some bad events which are not what we wanted to trigger like pileup events or the vertex finder fails to find the triggered V_z or something else. These kinds of events are shown as the horizontal and vertical bands in the left panel of Fig. 30

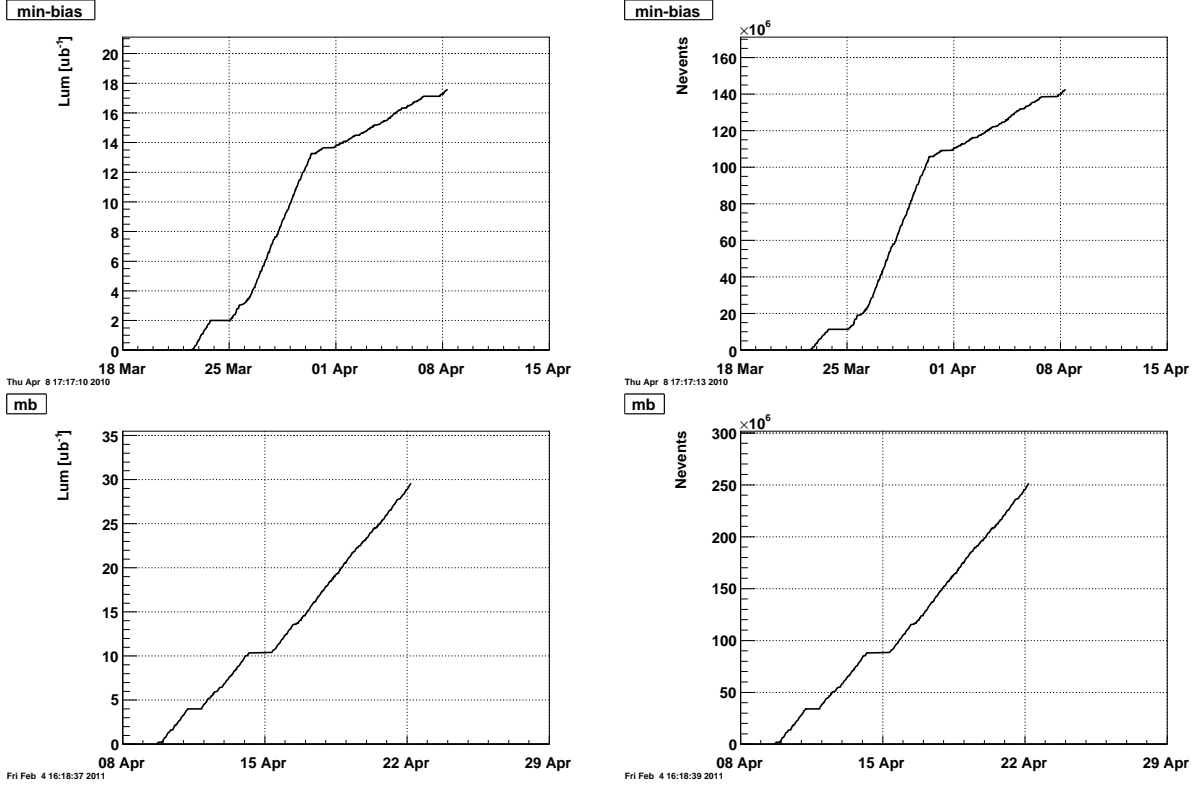


FIG. 29. The luminosity and events of MB trigger recorded for Au+Au collisions at $\sqrt{s_{NN}} = 62$ GeV (upper) and 39 GeV (bottom) versus time. Figures are taken from [8] [9].

and Fig. 31. The right panel of Fig. 30 and Fig. 31 shows the distribution of the difference between $V_z(VPD)$ and $V_z(TPC)$. The huge peak around zero is what we want to select. We used a $|V_z(TPC) - V_z(VPD)| < 4\text{cm}$ cut to reject the background events.

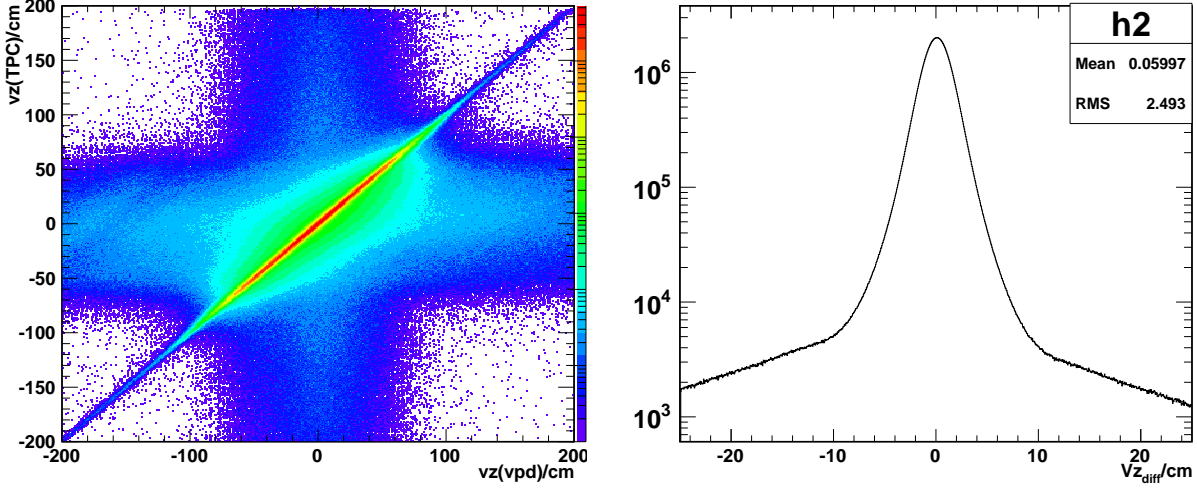


FIG. 30. The VPD V_z versus the reconstructed V_z position in Au+Au 62 GeV collisions (left panel), and the difference between $V_z(VPD)$ and $V_z(TPC)$, V_{zdiff} (right panel).

The left panel of Figure 32 and Fig. 33 show the V_x vs. V_y distribution before the vertex cut ($|V_z(TPC) - V_z(VPD)| < 4\text{cm}$) at Au+Au 62 and 39 GeV collisions. Most of the events collided

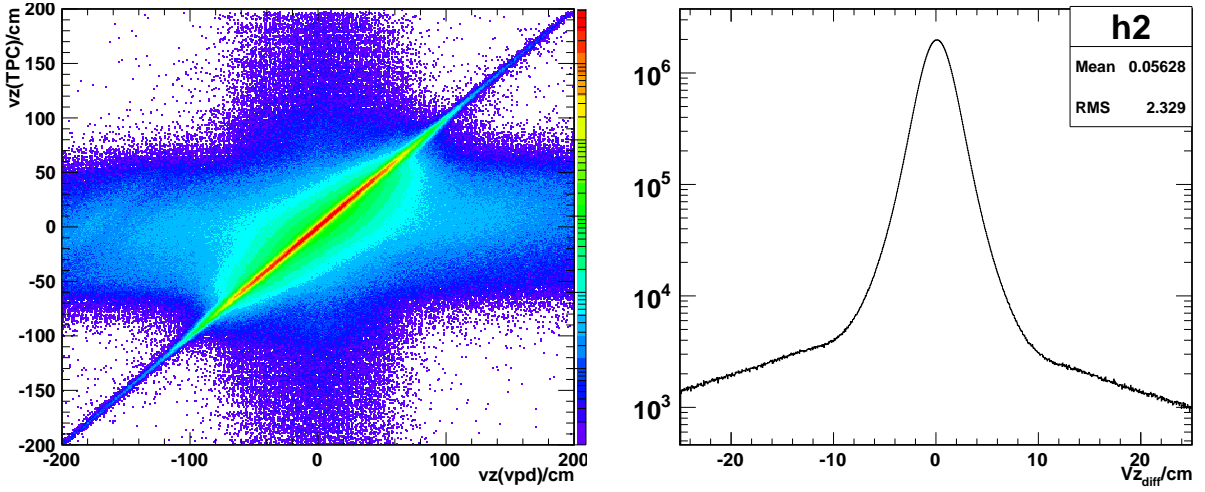


FIG. 31. The VPD V_z versus the reconstructed V_z position in Au+Au 39 GeV collisions (left panel), and the difference between $V_z(VPD)$ and $V_z(TPC)$, $V_{z\text{diff}}$ (right panel).

around 0, but clearly there are some events happening on the beam pipe. The right panel of this figure shows the same distribution after the vertex cut. The beam pipe events are successfully removed by the vertex cut. The vertexes of the survived events are very concentrated around 0.

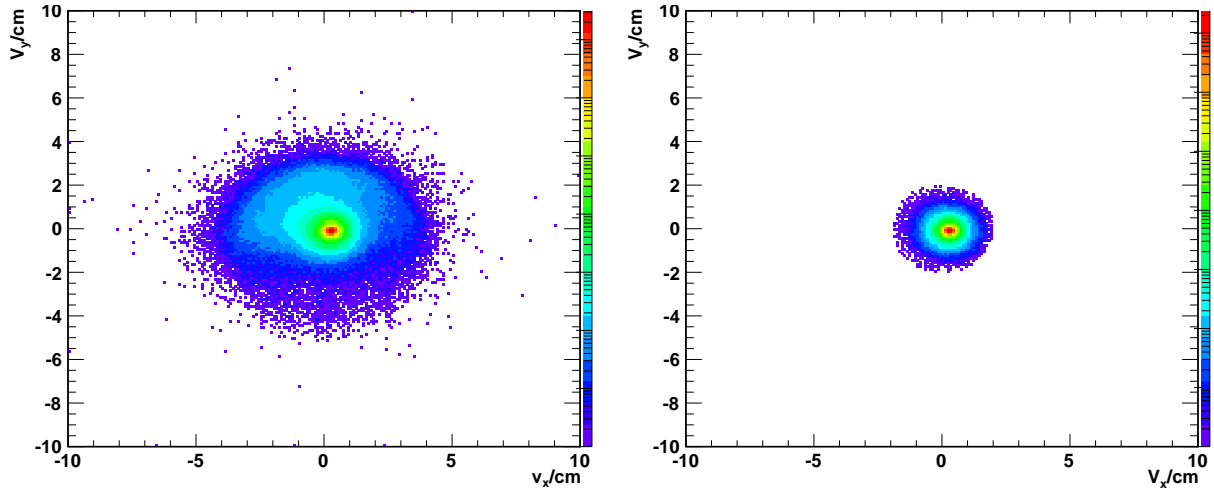


FIG. 32. V_x vs. V_y distribution before and after vertex cuts in MB triggered 62 GeV Au+Au collisions taken in Run 2010

The centralities for 62.4 GeV and 39 GeV are also determined from the StRefMultCorr class.

Event Cut Parameters	Cut Value	Events (39 GeV)	Events (62.4 GeV)
Valid vertex	$ V_x(TPC) > 10^{-5} \text{ cm}$ or $ V_y(TPC) > 10^{-5} \text{ cm}$ or $ V_z(TPC) > 10^{-5} \text{ cm}$	290 M	147 M
Vertex correlation	$ V_z(TPC) - V_z(VPD) < 4 \text{ cm}$	277 M	139 M
V_z	$ V_z(TPC) < 30 \text{ cm}$	260 M	131 M
$V_r = \sqrt{V_x^2 + V_y^2}$	$ V_r(TPC) < 2 \text{ cm}$	260 M	131 M
centrality	0-60%	182 M	94 M

TABLE X. Event selection cuts for RUN 2010 at 62.4 and 39 GeV Au+Au collisions

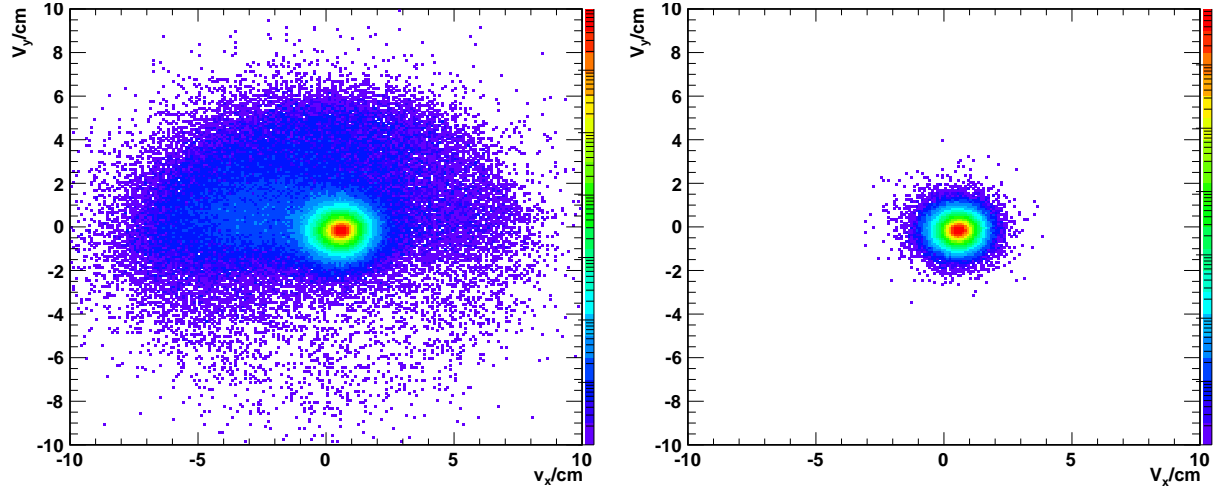


FIG. 33. V_x vs. V_y distribution before and after vertex cuts in MB triggered 39 GeV Au+Au collisions taken in Run 2010

C. Track Selection

Tracks are required to have $p_T > 0.2\text{GeV}/c$ in order to reach the outer radius of the TPC. To ensure a high track reconstruction quality, requirements are placed on the number of reconstructed hit points (nHitsFit), the number of dE/dx hit points (nHitsDedx), and the distance of closest approach between the track and the vertex (dca). We have two kinds of electron candidates in the analysis. One kind of electron is identified by combining TPC and EMC information, tagged as "TPC+EMC" electron. This kind of electron candidates have relative high p_T and high purity. The other kind of electron candidates use the TPC and TOF information to identify it, tagged as "TPC+TOF". This kind of electron candidates have relative lower p_T and lower purity. For "TPC+TOF" electrons, tracks are required to have $p_T > 0.2\text{GeV}/c$, nHitsFit ≥ 25 , nHitsDedx ≥ 15 and dca $< 3\text{cm}$ in Au+Au collisions at $\sqrt{s_{NN}} = 62.4$ and 39 GeV. For "TPC+EMC" electrons, tracks are required to have $p_T > 1.0\text{GeV}/c$, nHitsFit ≥ 25 , nHitsDedx ≥ 15 and dca $< 1\text{cm}$. Tracks are also assigned a flag during the fitting process to indicate the fit quality and detector used in the fitting. Tracks, which are poorly reconstructed, have flag < 0 and are not what we wanted. Post-crossing tracks that from pile-up have flag > 1000 and are also not considered. The quality requirements for tracks reconstructed in Au+Au collisions are listed in Table XI.

Requirements	"TPC+TOF" candidates	"TPC+EMC" candidates
Transverse Momentum	$p_T > 0.2\text{GeV}/c$	$p_T > 1.0\text{GeV}/c$
Pseudorapidity	$ \eta < 1.0$	$ \eta < 1.0$
Track Flag	$flag > 0$ and $flag < 1000$	$flag > 0$ and $flag < 1000$
Spatial Hits	$nHitsFit \geq 25$	$nHitsFit \geq 25$
dE/dx Hits	$nHitsDedx \geq 15$	$nHitsDedx \geq 15$
dca	$dca < 3\text{cm}$	$dca < 1\text{cm}$

TABLE XI. Primary track selection in Au+Au collisions at $\sqrt{s_{NN}} = 62.4$ and 39 GeV.

D. Electron Identification

In order to select electron and reject hadron, the TPC has been used as the primary tool for electron identification in STAR, and utilizes the reconstructed momentum and ionization energy

loss per unit length (dE/dx). The TOF and BEMC has been used to further discriminate between electrons and hadrons for "TPC+TOF" electron candidates and "TPC+EMC" electron candidates, respectively.

Below list the the main selection of the "EMC+TPC" electron candidates:

1. Electron identification using BEMC cluster energy:

a) $0.3 < p/E < 1.5$

2. Using BSMD information for electron identification

a) $n_\eta >= 1, n_\phi >= 1$

i. n_η : number of fired SMD cells on η plane

ii. n_ϕ : number of fired SMD cells on ϕ plane

b) $|phiDist| < 0.01, |zDist| < 2$ cm

i. phiDist: distant between track projection and EMC hit on ϕ plane

ii. zDist: distant between track projection and EMC hit on η plane

3. electron identification using dE/dx

a) $-1.0 < n\sigma_e < 2.5$

4. p_T cut

a) $p_T > 1GeV/c$

The cuts for "TPC+TOF" electron identification are listed below:

1. Electron identification using TOF information:

a) TOF match

b) 39GeV: $|1/\beta - 1.00| < 0.03$; 62GeV: $|1/\beta - 0.99| < 0.03$

2. electron identification using dE/dx

a) $-1.0 < n\sigma_e < 2.5$

3. p_T cut

a) $p_T > 0.2GeV/c$

Figure 34, figure 35, figure 36, figure 37 and figure 38 shows the p/E , n_η , n_ϕ , z_{dist} and ϕ_{dist} distribution for electron sample and hadron sample in 62GeV and 39GeV Au+Au collisions at $2.0 < p_T < 3.0$ GeV/c, respectively. The green histogram is for electron sample (photonic electron sample), the selection cuts besides the basic tracking quality and TOF cuts for this sample are: $1 < n\sigma_e < 2 \& m_{pair} < 0.01$. The red histogram is for hadron sample ($|n\sigma_e| > 2.0$). The histograms are normalized to have the same number of total entries. BSMD is helpful for identifying electrons by providing Electro-Magnetic shower size and shower position compared with track projected position.

Figure 39 shows $1/\beta$ distribution for electron sample (photonic electron sample) in 62GeV and 39GeV Au+Au collisions at $0.3 < p_T < 0.4$ GeV/c. We use a gaussian function to fit the $1/\beta$ distribution from 62GeV and 39GeV. The mean from the fit of 62 GeV is about 0.99, while the mean from the fit of 39GeV is about 1.00. The σ from the fits are both at value of 0.01.

Figure 40 shows the $n\sigma_e$ distribution for "TPC+EMC" electron sample and "TPC+TOF" electron sample in 62GeV and 39 GeV Au+Au collisions. The event selection, track quality and electron identification (EID) requirements are summarized in Table XII for Au+Au 62GeV and 39 GeV.

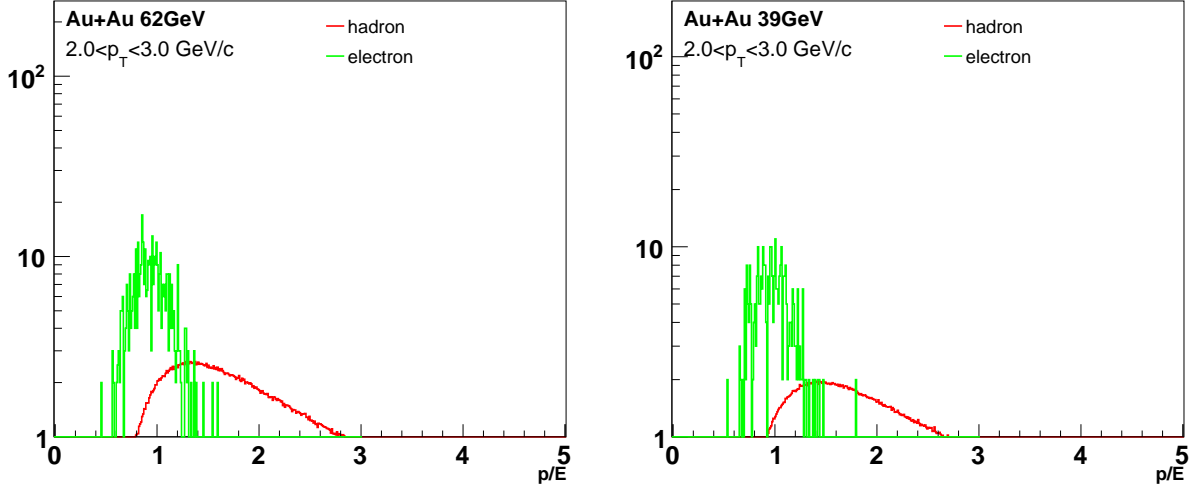


FIG. 34. p/E distribution for electron sample (from photonic electron) and hadron sample in 62GeV (left panel) and 39 GeV (right panel) Au+Au collisions taken in 2010

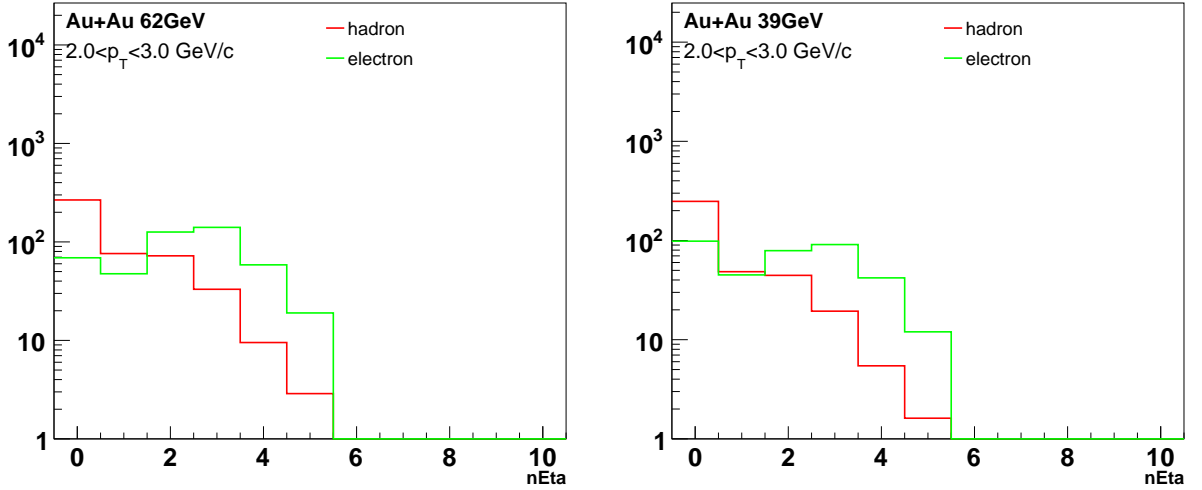


FIG. 35. n_η distribution for electron sample (from photonic electron) and hadron sample in 62GeV (left panel) and 39 GeV (right panel) Au+Au collisions taken in 2010

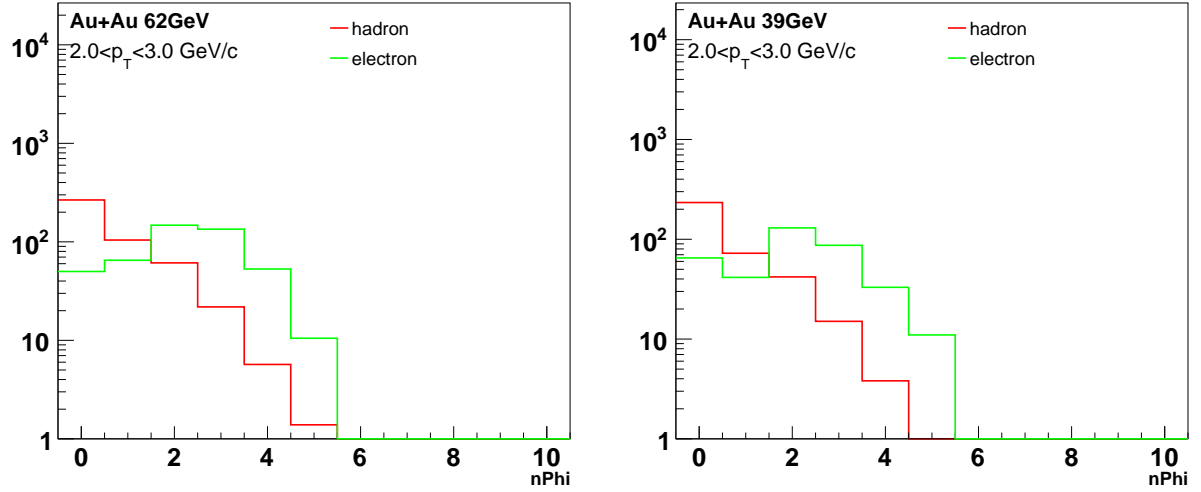


FIG. 36. n_ϕ distribution for electron sample (from photonic electron) and hadron sample in 62GeV (left panel) and 39 GeV (right panel) Au+Au collisions taken in 2010

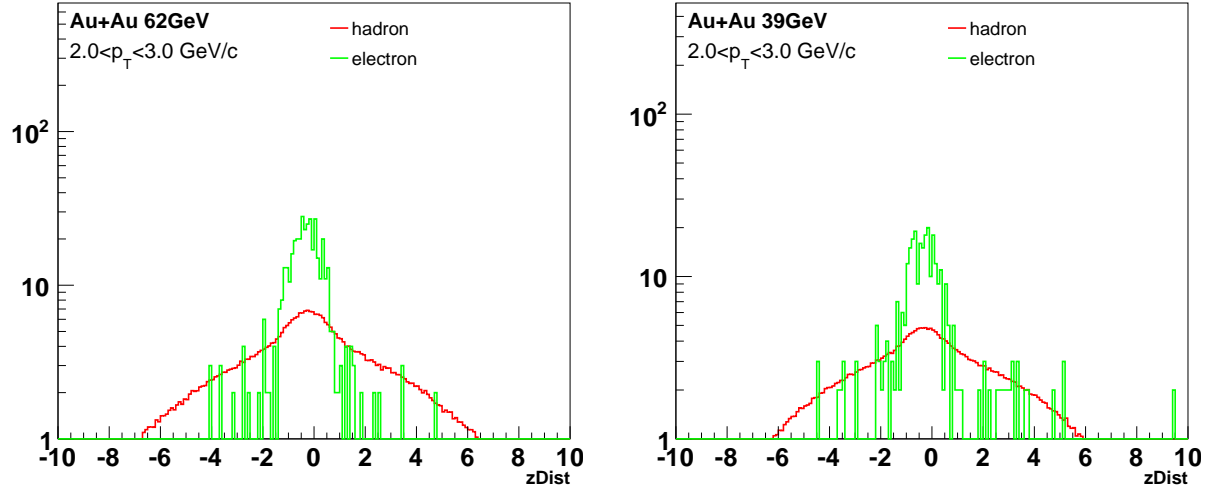


FIG. 37. z_{Dist} distribution for electron sample (from photonic electron) and hadron sample in 62GeV (left panel) and 39 GeV (right panel) Au+Au collisions taken in 2010

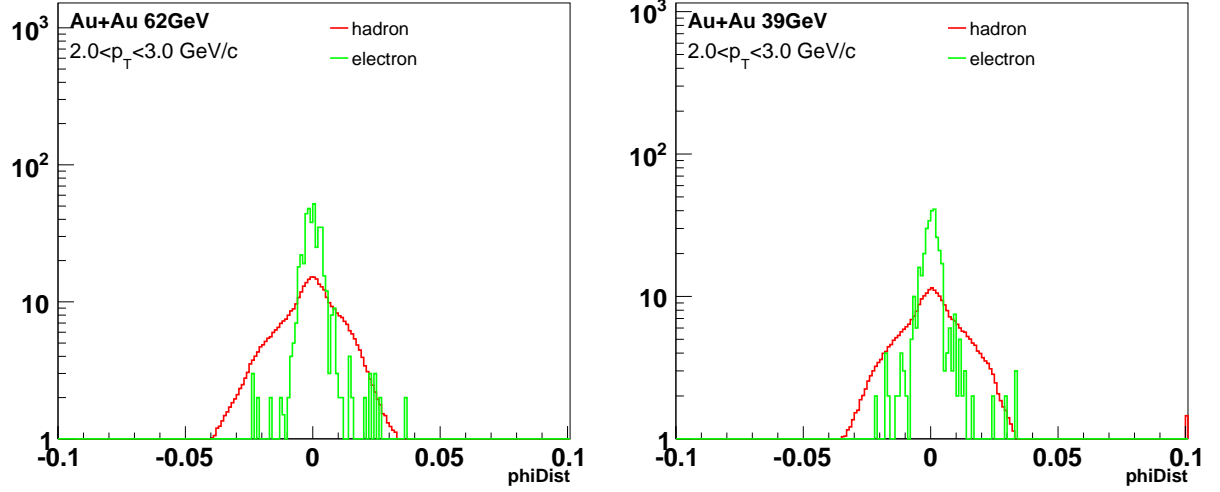


FIG. 38. ϕ_{Dist} distribution for electron sample (from photonic electron) and hadron sample in 62GeV (left panel) and 39 GeV (right panel) Au+Au collisions taken in 2010

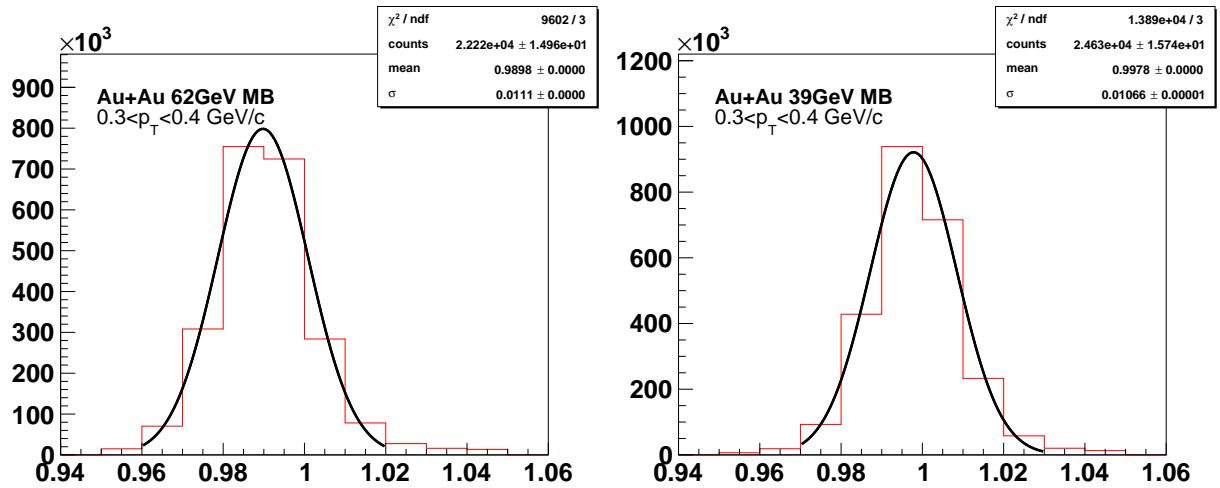


FIG. 39. $1/\beta$ distribution for electron sample (from photonic electron) and hadron sample in 62GeV (left panel) and 39 GeV (right panel) Au+Au collisions taken in 2010

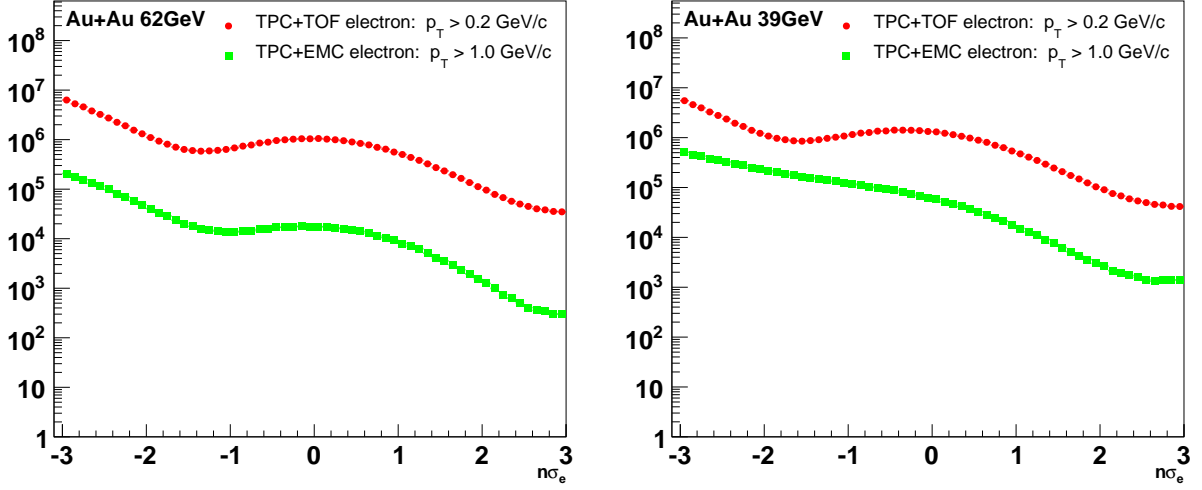


FIG. 40. $n\sigma_e$ distribution for electron sample (from photonic electron) and hadron sample in 62GeV (left panel) and 39 GeV (right panel) Au+Au collisions taken in 2010

Event Cut Parameters	Cuts Value
Trigger Ids (62GeV)	270001 or 270011 or 270021
Trigger Ids (39GeV)	280001
Valid vertex	$ V_x(TPC) > 10^{-5} \text{cm}$ or $ V_y(TPC) > 10^{-5} \text{cm}$ or $ V_z(TPC) > 10^{-5} \text{cm}$
Vertex correlation	$ V_z(TPC) - V_z(VPD) < 4\text{cm}$
V_z	$ V_z(TPC) < 30\text{cm}$
$V_r = \sqrt{V_x^2 + V_y^2}$	$ V_r(TPC) < 2\text{cm}$

Track quality and eID cuts ("TPC+EMC" electron)	Cuts value
Transverse Momentum	$p_T > 1.0 \text{GeV}/c$
Pseudorapidity	$ \eta < 1.0$
Track Flag	$flag > 0$ and $flag < 1000$
Spatial Hits	$nHitsFit \geq 25$
dE/dx Hits	$nHitsDedx \geq 15$
dca	$dca < 1\text{cm}$
p/E	$0.3 < p/E < 1.5$
$n\eta$	$n\eta \geq 1$
$n\phi$	$n\phi \geq 1$
ϕ_{Dist}	$ \phi_{Dist} < 0.01$
Z_{Dist}	$ Z_{Dist} < 2$
$n\sigma_e$	$-1 < n\sigma_e < 2$

Track quality and eID cuts ("TPC" electron)	Cuts value
Transverse Momentum	$p_T > 0.2 \text{GeV}/c$
Pseudorapidity	$ \eta < 1.0$
Track Flag	$flag > 0$ and $flag < 1000$
Spatial Hits	$nHitsFit \geq 25$
dE/dx Hits	$nHitsDedx \geq 15$
dca	$dca < 3\text{cm}$
p/E	$0.3 < p/E < 1.5$
$1/\beta$ (62GeV)	$ 1/\beta - 0.99 < 0.03$
$1/\beta$ (39GeV)	$ 1/\beta - 1 < 0.03$
$n\sigma_e$	$-1 < n\sigma_e < 2$

TABLE XII. analysis cuts for Run10 62GeV and 39GeV Au+Au collisions

E. Efficiency and Acceptance

² As the analysis in Run11 200GeV Au+Au MB collisions, the total J/ψ efficiency and acceptance
³ was determined by combining the electron tracking efficiency and acceptance with the electron
⁴ identification efficiencies using a toy model. The details will be described as bellow.

TPC tracking efficiency and acceptance

In order to determine the TPC tracking efficiency and acceptance, Monte Carlo electrons were embedded into real events. A GEANT simulation was used to determine the interaction of electrons with the detector material, after which the TPC Response Simulator was used to model the ionization energy and detector response. The embedding was performed using production P10ik and library SL10k_embed. Flat input spectra for the Monte Carlo electron transverse momentum, ϕ and rapidity distributions were used to reduce CPU time and increase statistics at higher p_T . The input electron p_T , ϕ and rapidity distribution are shown in Fig.41 for Au+Au 62GeV. And the p_T , ψ and rapidity distribution of electrons in Au+Au 39GeV are shown in Fig.42

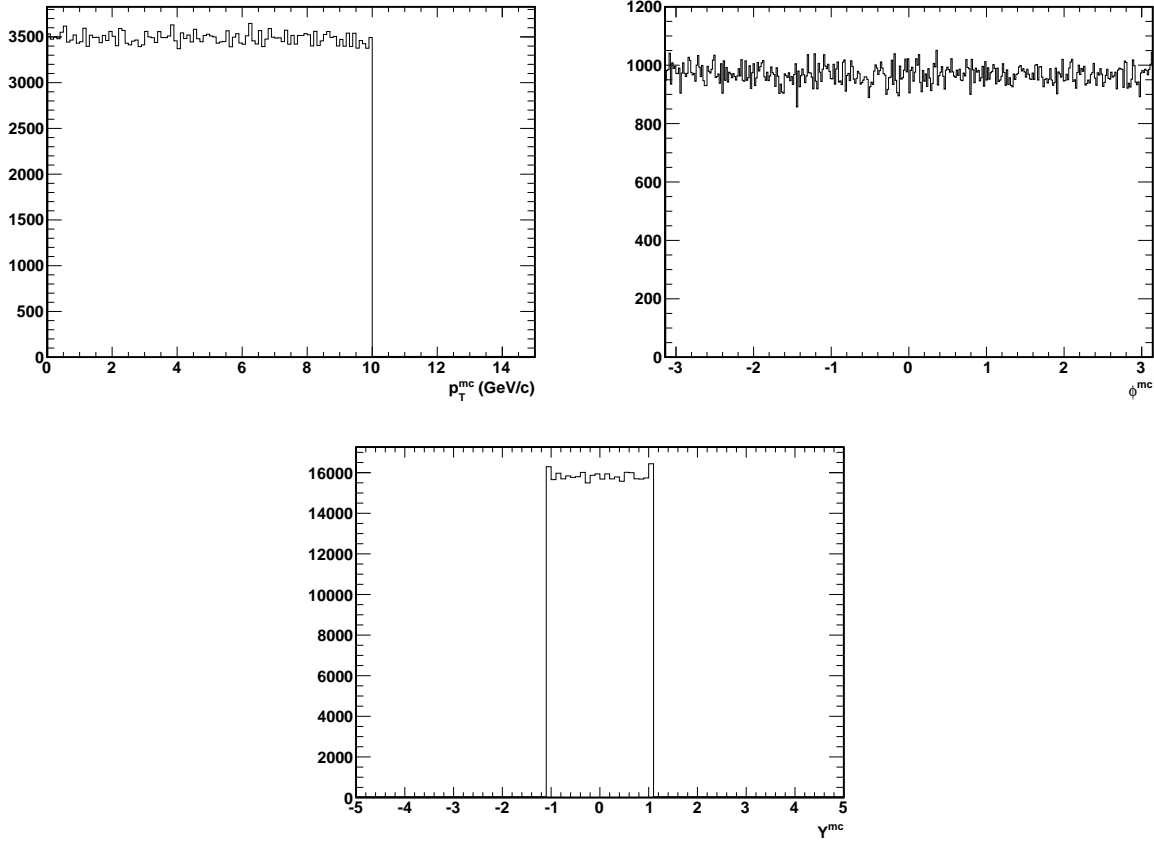


FIG. 41. The input electron p_T , ϕ and rapidity distribution for Au+Au 62GeV.

The Monte Carlo electron that pass through the TPC acceptance and were reconstructed by the tracking software were subjected to the same track quality requirements as the real data. Since the dE/dx can not be reproduce very well in embedding, we get the dE/dx distribution from data. For nHitsDedx cut efficiency, we also got it from data.

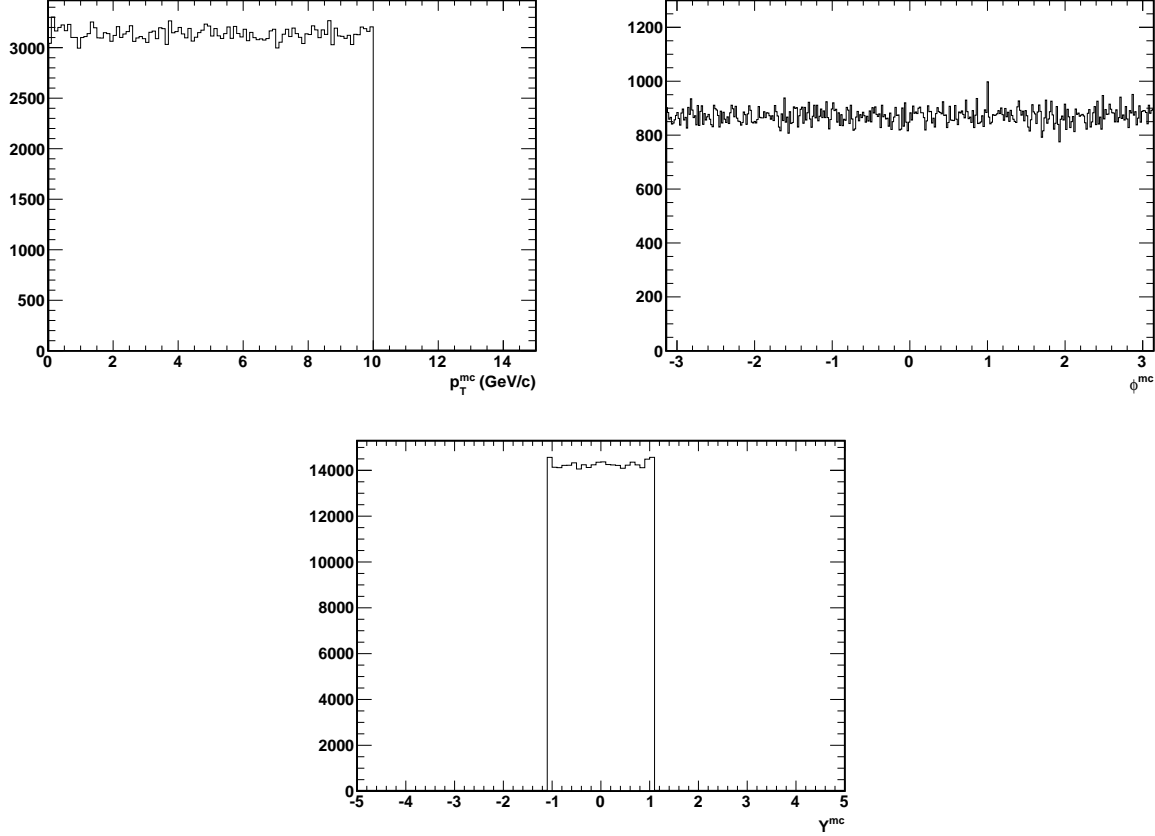


FIG. 42. The input electron p_T , ϕ and rapidity distribution for Au+Au 39GeV.

1 The embedding request and QA were made by Mustafa Mustafa. The embedding request can be
2 found at:

3 <http://www.star.bnl.gov/HyperNews-star/protected/get/heavy/3351.html>

4 <http://www.star.bnl.gov/HyperNews-star/protected/get/heavy/3350.html>

5 The QA plots of embedding can be found at:

6 http://www.star.bnl.gov/protected/heavy/mstftsm/NPE/AuAu62GeV/embeddingQA/single_e/embedding_qa_electrons_positrons_st_physics.pdf

8 http://www.star.bnl.gov/protected/heavy/mstftsm/NPE/AuAu62GeV/embeddingQA/single_e/embedding_qa_electrons_positrons_st_physics.pdf

10 Figure 43 shows the electron daughters efficiency as a function of MC p_T for 62GeV (left panel)
11 and 39GeV (right panel) after cuts listed bellow:

12 a) $n\text{HitsFit} \geq 25$

13 b) $dca < 3 \text{ cm}$

Momentum resolution

15 The momentum resolution and bremsstrahlung radiation energy loss are also obtained from the
16 embedding. We separate them into transverse momentum p_T . Figure 44 shows the ratio of re-
17 constructed p_T and MC p_T , p_T^{RC}/p_T^{MC} , distributions in different p_T bins for 62GeV and 39GeV,

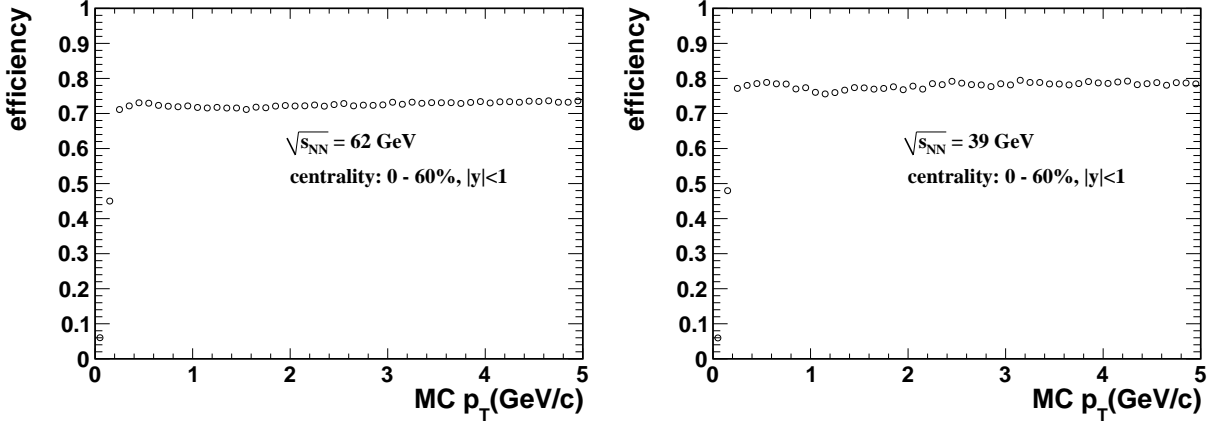


FIG. 43. Electron tracking efficiency as a function of MC p_T in Au+Au 62GeV (left panel) and 39GeV (right panel).

1 respectively. The integral of the histograms are normalized to 1. The Gaussian peaks around 1 are
2 due to p_T resolution and the long tails on the left side are due to bremsstrahlung radiation energy
3 loss. The p_T smearing is strongly dependent on p_T . Figure 45 shows the distribution of the difference
4 of reconstructed η and its corresponding MC η , $\eta^{RC} - \eta^{MC}$, in different p_T bins for Au+Au 62GeV
5 and 39GeV, respectively. The smearing is quite small, on the order of 0.01. The dependence on p_T
6 is small. Figure 46 shows the distribution of the difference of reconstructed ϕ and its corresponding
7 MC ϕ , $\phi^{RC} - \phi^{MC}$, in different p_T bins. The smearing is even smaller, on the order of 0.01. It has
8 small dependence on p_T .

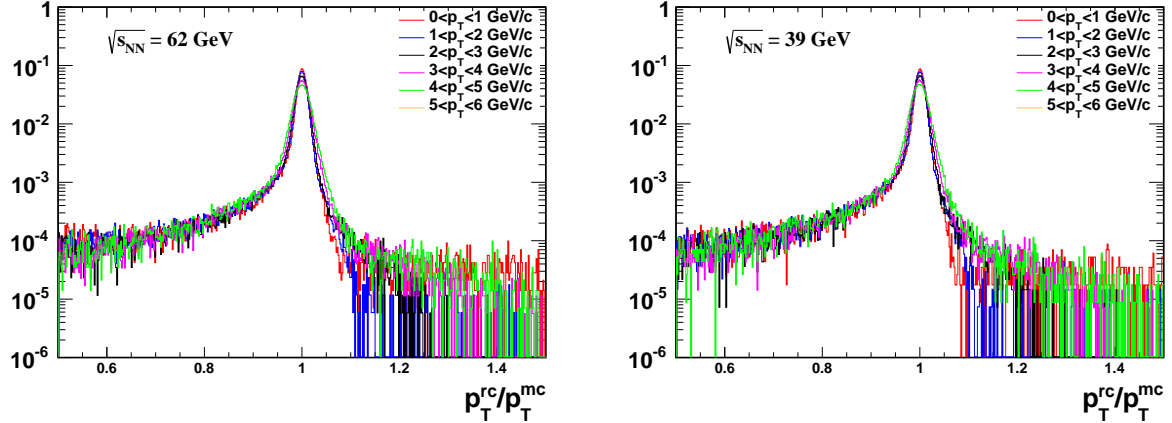


FIG. 44. The p_T^{rc}/p_T^{mc} distribution of electrons in different p_T bins for Au+Au 62GeV (left panel) and 39GeV (right panel), respectively.

9

10

11

BEMC cuts efficiency

12 Electron candidates in the TPC are projected to the BEMC and matched to an energy cluster
13 to determine their momentum-to-energy ratio p/E . And the information of BSMD, such as
14 $n\eta, n\phi, PhiDist$ and $ZDist$, is also used for electron identification.

15 The same methods of matching tracks to the BEMC and BSMD was performed in simulation.
16 Monte Carlo electrons were embedded into real data events and propagated through the detector
17 using a GEANT simulation. The tracks reconstructed form the Monte Carlo electrons were matched

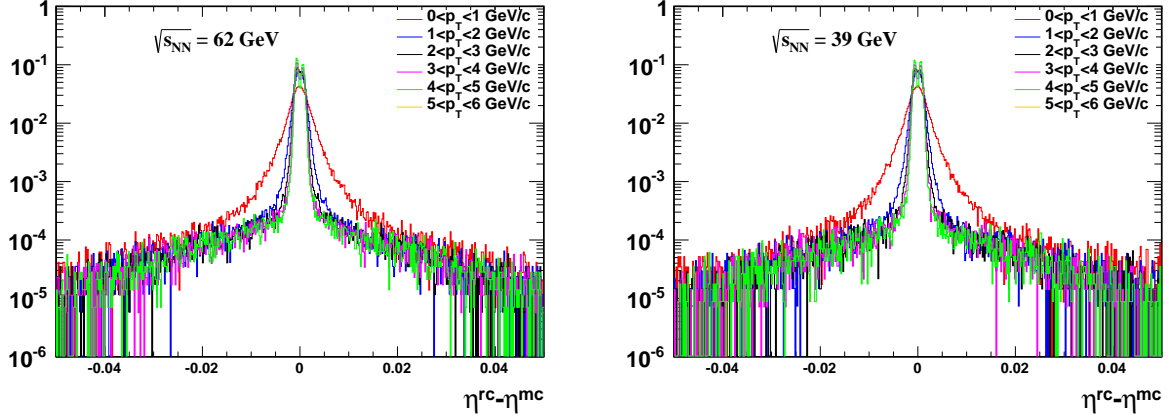


FIG. 45. The $\eta^{rc} - \eta^{mc}$ distribution of electrons in different p_T bins for Au+Au 62GeV (left panel) and 39GeV (right panel), respectively.

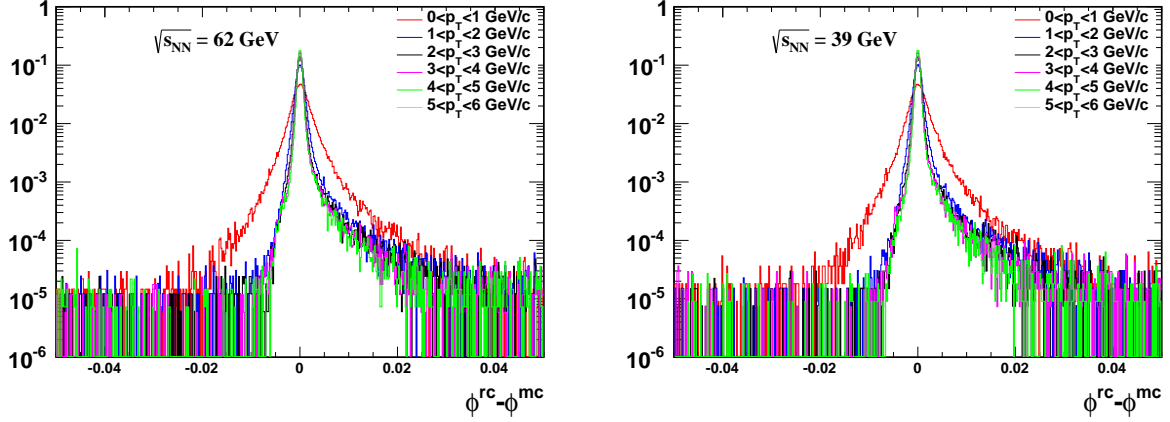


FIG. 46. The $\phi^{rc} - \phi^{mc}$ distribution of electrons in different p_T bins for Au+Au 62GeV and 39GeV, respectively.

to the BEMC and BSMD to determine the detector performance.

Figure 47 shows the electron efficiency as a function of MC p_T in $|\eta| < 1$ after TPC tracking, BEMC matching and cuts listed below ("TPC+EMC" electron efficiency):

- $n\text{HitsFit} \geq 25$
- $dca < 1\text{cm}$
- $0.3 < p/E < 1.5$
- $\|n\eta\| \geq 1, \|n\phi\| \geq 1, \|Phi_{Dist}\| < 0.01, \|Z_{Dist}\| < 2$

TOF cuts efficiency

The TOF conditions are not well simulated in the embedding so efficiencies of the TOF cuts have to be calculated from data. The efficiency of matching a track to the TOF in $Au + Au$ collisions was obtained from a high purity sample of electrons (photonic electron sample) from data by requiring $m_{ee} < 10MeV/c^2$. The TOF matching efficiency for electrons is caculated as a number of electrons

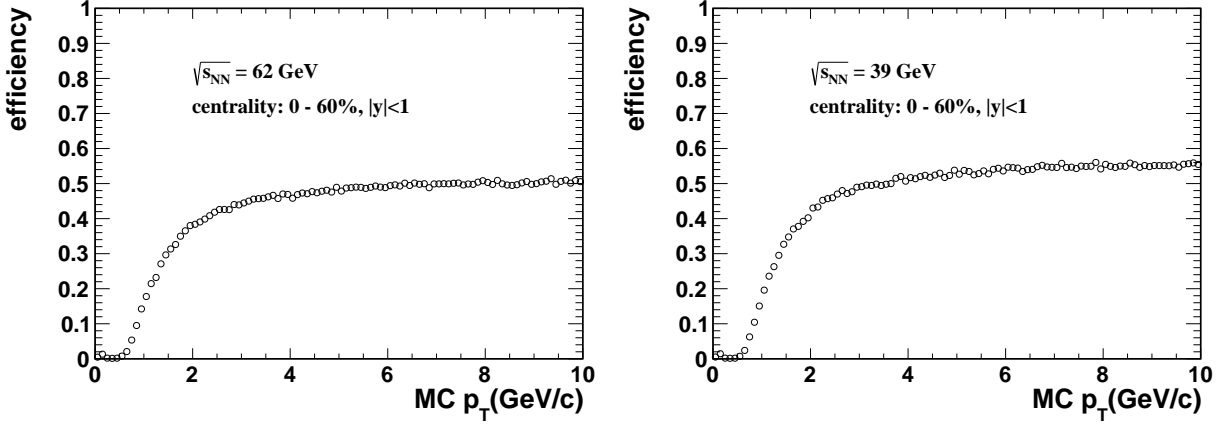


FIG. 47. The “TPC+EMC” electron efficiency as a function of MC p_T in midrapidity at centrality 0- 60% for Au+Au 62GeV (left panel) and 39GeV (right panel).

that match to the TOF divided by a number of electrons in the TPC (N_{TPC}^e) that passed the track quality and acceptance cuts:

$$\epsilon_{TOF\,matching} = \frac{N_{TOF}^e}{N_{TPC}^e} \quad (9)$$

The $1./\beta$ cut efficiency is also extracted using the photonic electron sample. The TOF matching efficiency and $1./\beta$ cut efficiency as a function of p_T is shown in Fig.48 and Fig.49 for Au+Au 62GeV and 39GeV, respectively.

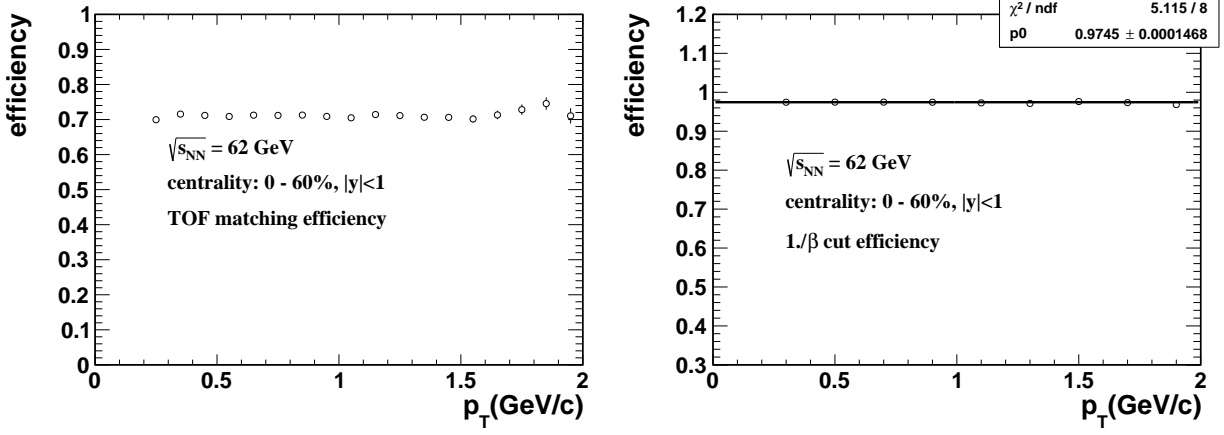
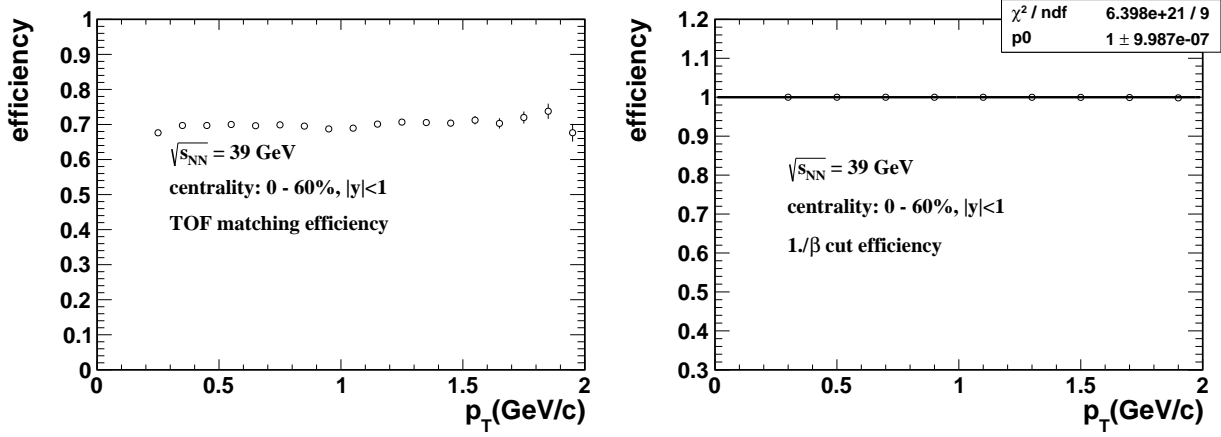


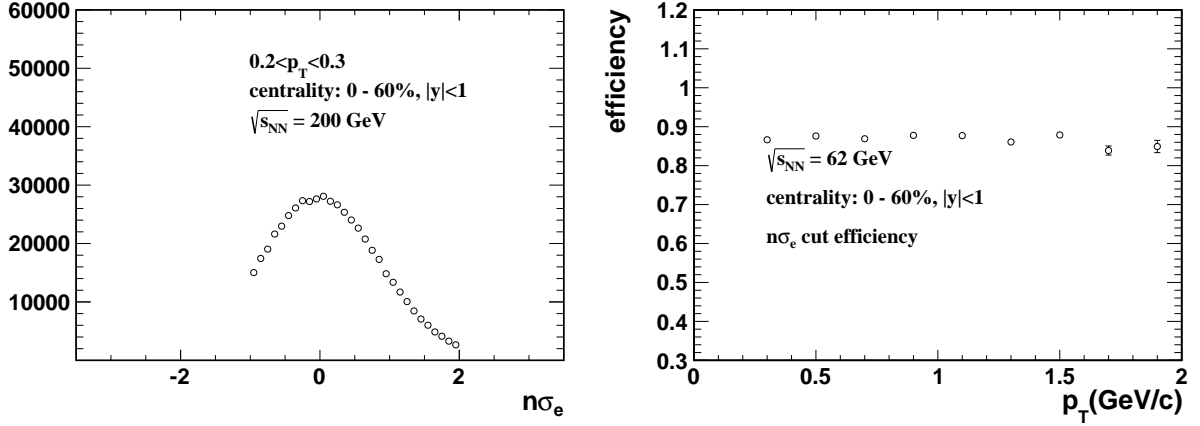
FIG. 48. The TOF matching efficiency and $1./\beta$ cut efficiency verse p_T for Au+Au 62GeV.

$n\sigma_e$ cuts efficiency

Since the dE/dx can not be reproduced very well in embedding, we get the $n\sigma_e$ distribution from data. After enhancing the electron contribution in the $n\sigma_e$ distribution by using the TOF and selecting photonic electrons, a Gaussian + exponential fitting was performed to the $n\sigma_e$ distribution to determine the shape of the electron contribution. Fig.50 and Fig.51 shows the $n\sigma_e$ distribution

FIG. 49. The TOF matching efficiency and $1/\beta$ cut efficiency verse p_T for Au+Au 39GeV.

for $0.2 < p_T < 0.3 \text{ GeV}/c$ and the $n\sigma_e$ cut efficiency as a function of p_T in Au+Au collisions for 62GeV and 39GeV, respectively.

FIG. 50. The $n\sigma_e$ distribution for electrons with $0.2 < p_T < 0.3 \text{ GeV}/c$ (left panel) and the $n\sigma_e$ cut efficiency as a funcion of p_T (right panel) for Au+Au 62GeV.

3

nHitsDedx cuts efficiency

The $n\text{HitsDedx} \geq 15$ cut efficiency is obtained from the photonic electron sample. We compared the number of electron candidates with and without this $n\text{HitsDedx}$ cut after the basic tracking quality cuts the same as we used in the analysis. The efficiency as a function of p_T is shown in Fig.52 for Au+Au 62GeV (left panel) and 39GeV (right panel).

9

F. Total J/ψ detection efficiency

After getting the detection efficiencies for the decay electrons, the J/ψ detection efficiency is then determined by folding the efficiencies of the decay electrons using the J/ψ decays kinematics. We wrote a toy model to calculate the total J/ψ detection efficiency which follows almost the same steps as we did in Au+Au 200GeV analysis.

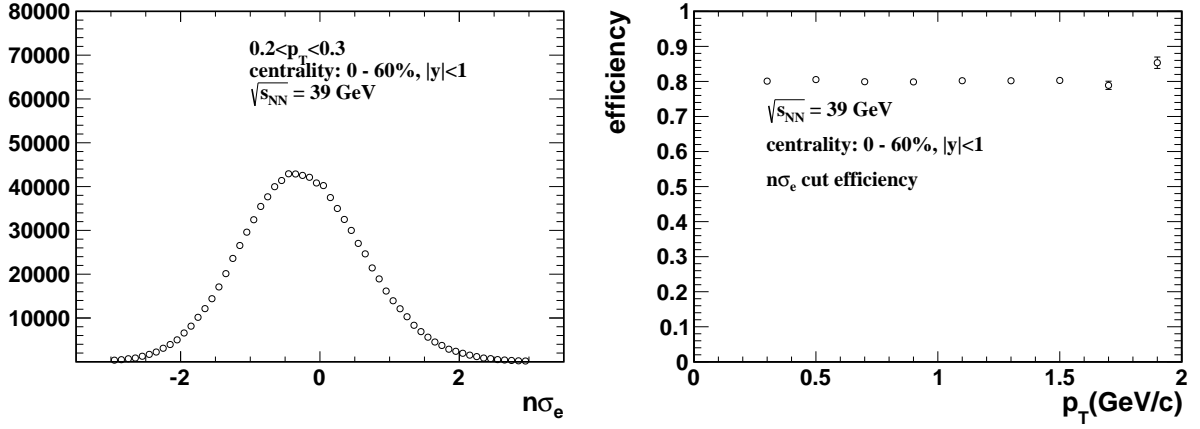


FIG. 51. The $n\sigma_e$ distribution for electrons with $0.2 < p_T < 0.3 \text{ GeV}/c$ (left panel) and the $n\sigma_e$ cut efficiency as a function of p_T (right panel) for Au+Au 39GeV.

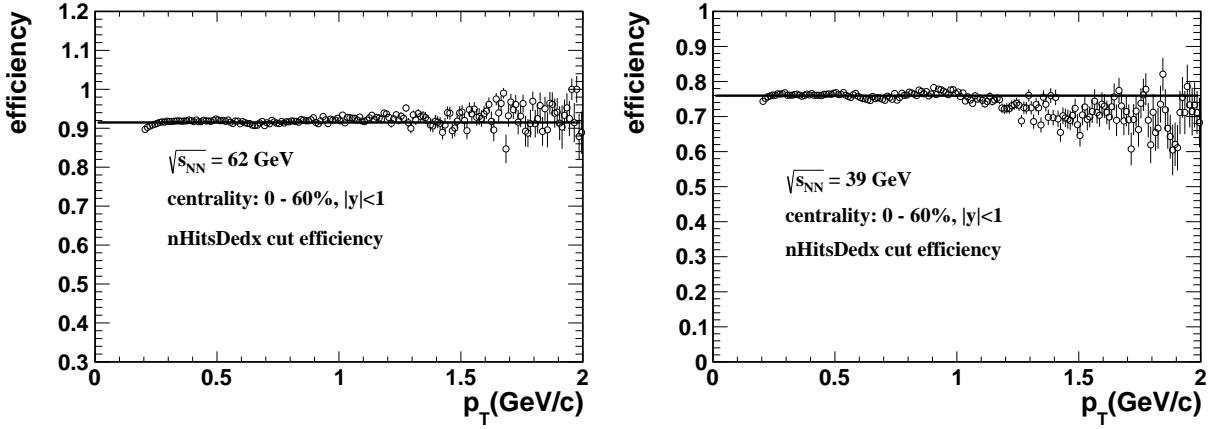


FIG. 52. The $n\text{HitsDedx}$ cut efficiency as a function of p_T for Au+Au 62GeV (left panel) and 39GeV (right panel).

The p_T and centrality dependence of the total J/ψ efficiency correction in Au+Au collisions for 62GeV (left panel) and 39GeV (right panel) are shown in Fig. 53. The efficiency increases with p_T and decreases in more central collisions. The total efficiency and acceptance corrections have been used to correct the measured J/ψ p_T spectrum to determine the invariant J/ψ yield. The J/ψ signal and invariant yield in $Au + Au$ collisions are described in the following chapter.

G. J/ψ signal and invariant yield

The reconstruction of J/ψ has been performed in Au+Au collisions at STAR via the dielectron decay channel:

$$J/\psi \rightarrow e^+ + e^- (\mathcal{B} = 5.94 \pm 0.06\%),$$

where \mathcal{B} is the branching ratio of the J/ψ decay to dielectrons.

The dielectron invariant mass spectrum is presented below, followed by a description of the J/ψ yield extraction and efficiency correction. Finally, the J/ψ invariant p_T spectrum is presented.

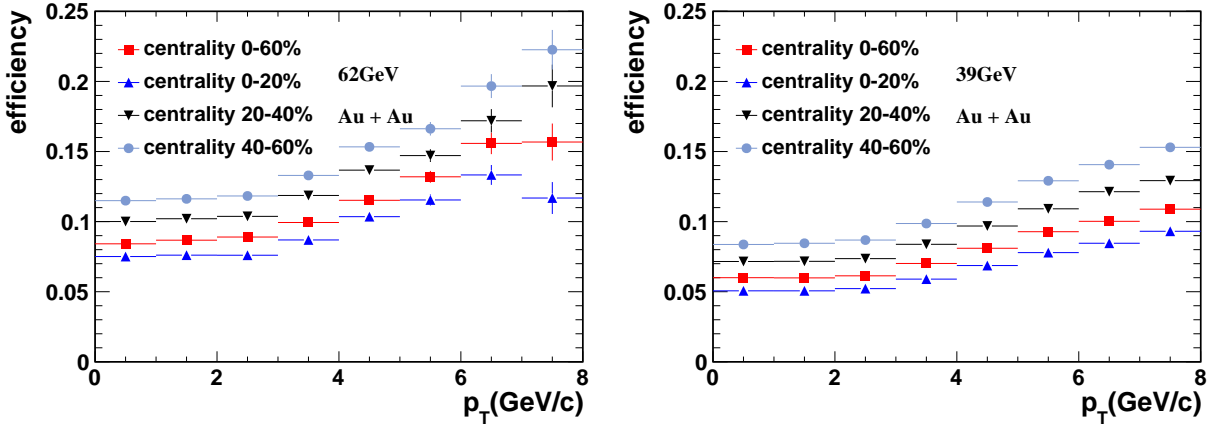


FIG. 53. The J/ψ total efficiency versus p_T for various centrality bins in Au+Au collisions for 62GeV (left panel) and 39GeV(right panel).

J/ψ signal

The dielectron invariant mass spectrum for $|y| < 1$ in different p_T range is shown in Fig. 54 and Fig. 55 for minimum bias triggered data in 0 – 60% central collisions for 62GeV and 39GeV, respectively.

The J/ψ line-shape from embedding with additional p_T smearing is shown in Fig. 56, along with the J/ψ signal from the data for Au+Au 39 and 62.4 GeV, respectively.

The J/ψ raw signal, signal-to-background ratio, and significance obtained in each p_T bin are summarized in Table XIII. The detail plots can be found in appendix Fig. 69 and 70.

Centrality (%)	p_T (GeV/c)	$N_{J/\psi}$	S/B	$S/\delta S$
39 GeV				
0-60	0-1	101	0.44	5.6
	1-2	121	0.48	6.3
	2-3	78	0.88	6.1
	3-4	16	0.64	2.5
62.4 GeV				
0-60	0-1	150	0.28	5.7
	1-2	244	0.40	8.4
	2-3	119	0.48	6.2
	3-4	36	0.44	3.3

TABLE XIII. The J/ψ uncorrected signal $N_{J/\psi}$, signal-to-background ratio S/B and significance $S/\delta S$ obtained in 39 and 62.4 GeV Au+Au collisions

J/ψ invariant p_T spectrum

The J/ψ p_T spectrum for different centrality bins in Au+Au 39 GeV, 62 GeV and 200 GeV collisions is shown in Fig. 57.

H. Systematic uncertainties

Following almost the same procedure we used in Au+Au 200 GeV analysis, the systematic uncertainties for 62 GeV and 39 GeV is listed in table XIV and table XV, respectively. As shown in

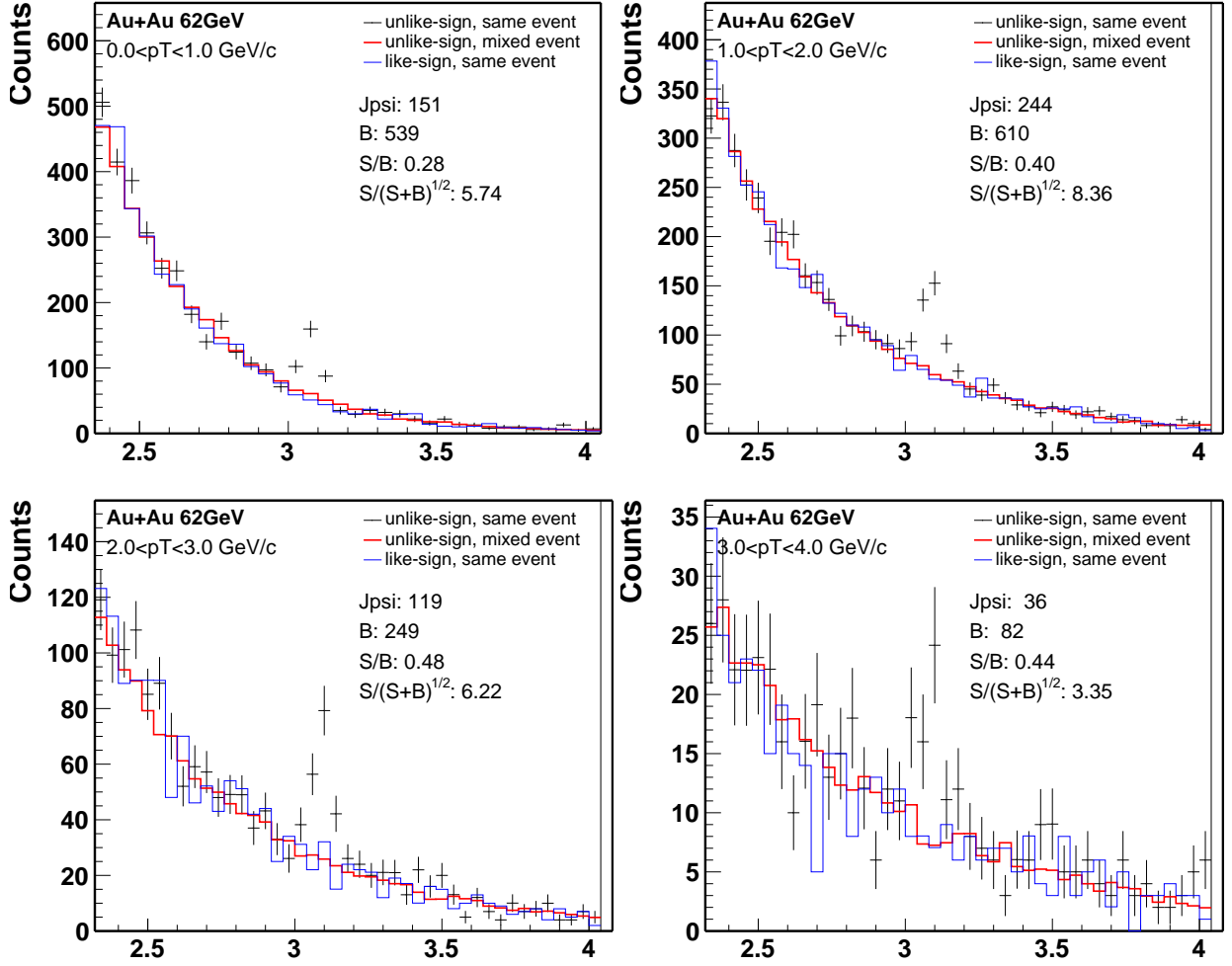


FIG. 54. The dielectron mass spectrum in 0 – 60% central Au+Au collisions 62GeV.

table XV, the total systematic uncertainties in 39 GeV are dominated by the BEMC related cuts. The efficiency of BEMC related cuts versus p_T from data (photo-electron sample) and embedding for 39 and 62.4 GeV Au+Au collisions is shown in Fig. 58, respectively. As depicted in this figure, there exists disagreement between simulation and data for Au+Au 39 GeV. And the difference between data and embedding has been assigned as systematic uncertainties.

p_T range (GeV/c)	0 – 1	1 – 2	2 – 3	3 – 4	4 – 5
dca cuts (%)	2.94	2.28	1.27	1.07	-
nHitsFit cuts (%)	3.71	2.88	1.06	1.25	-
$n\sigma_e$ cuts (%)	2.98	4.14	10.52	13.61	-
TOF related cuts (%)	2.00	2.00	2.00	2.00	-
BEMC related cuts (%)	4.39	3.97	3.35	3.33	-
yield extraction (%)	6.19	6.24	2.52	7.35	-
radiative decay (%)	4.00	4.00	4.00	4.00	-
total for 0-60% (%)	10.43	10.26	12.29	16.52	-
total for 0-20% (%)	11.53	11.23	11.89	17.54	-
total for 20-40% (%)	12.24	10.34	11.79	17.53	-
total for 40-60% (%)	11.36	10.58	11.75	17.51	-

TABLE XIV. The systematic uncertainties verse p_T for MB Au+Au 62 GeV.

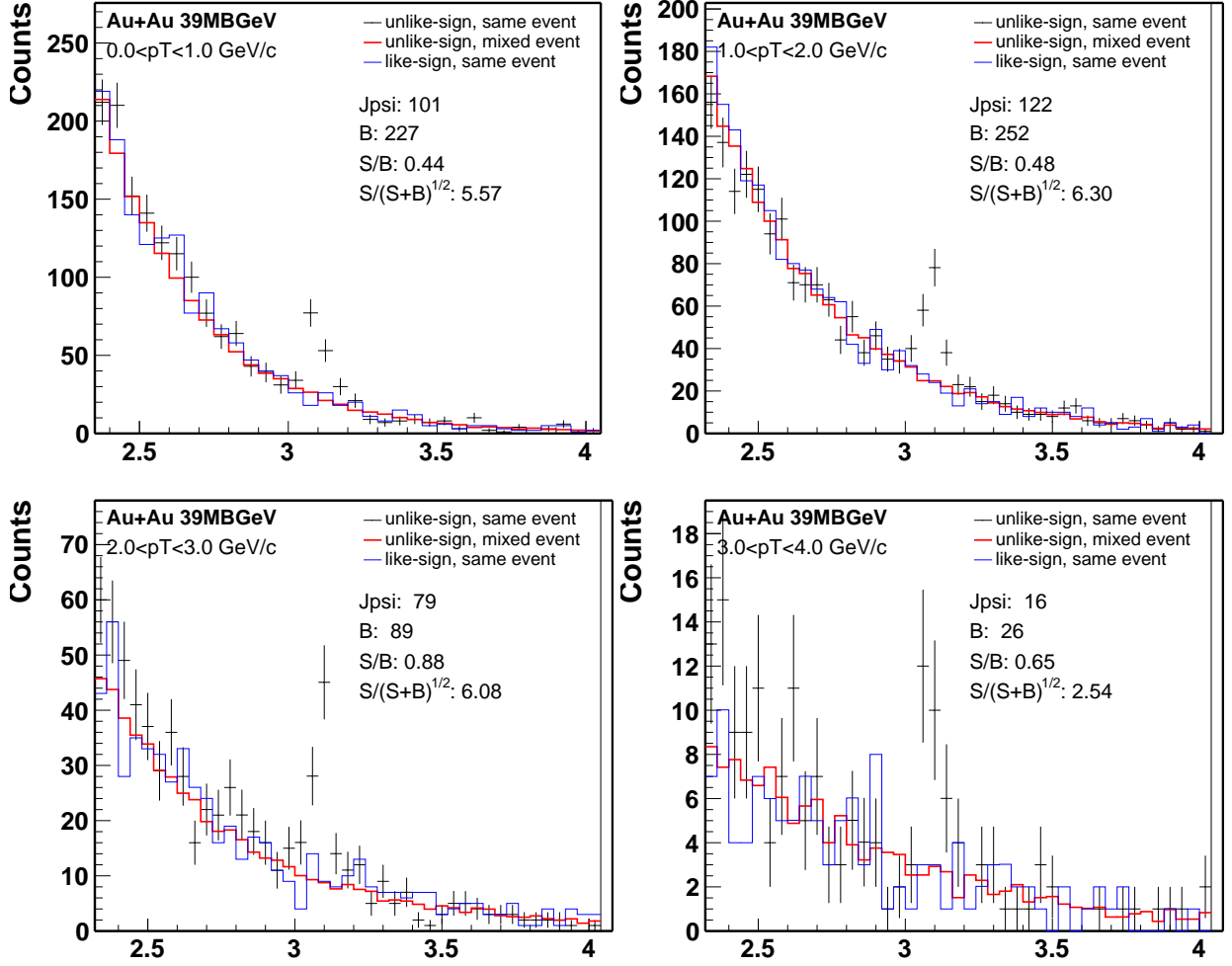


FIG. 55. The dielectron mass spectrum in 0 – 60% central Au+Au collisions 39GeV.

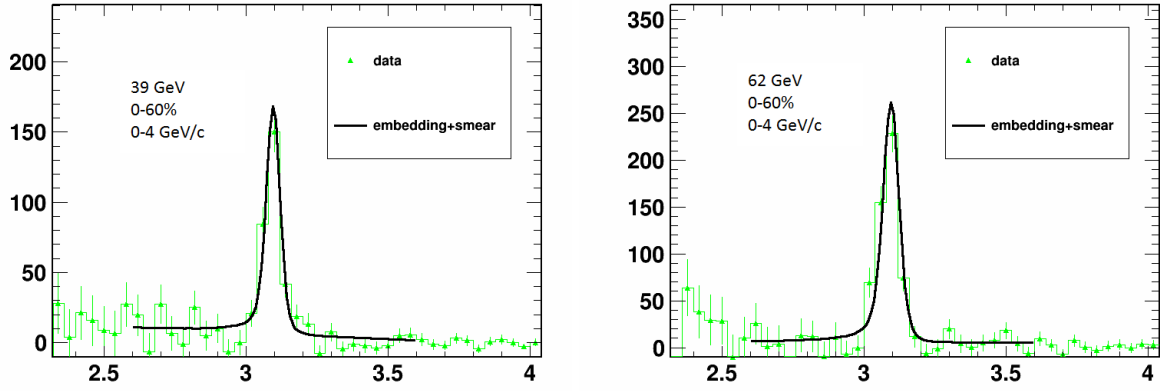


FIG. 56. The J/ψ signal after the combinatorial background subtraction with the J/ψ line shape from embedding with additional p_T smearing for Au+Au 39 and 62.4 GeV, respectively.

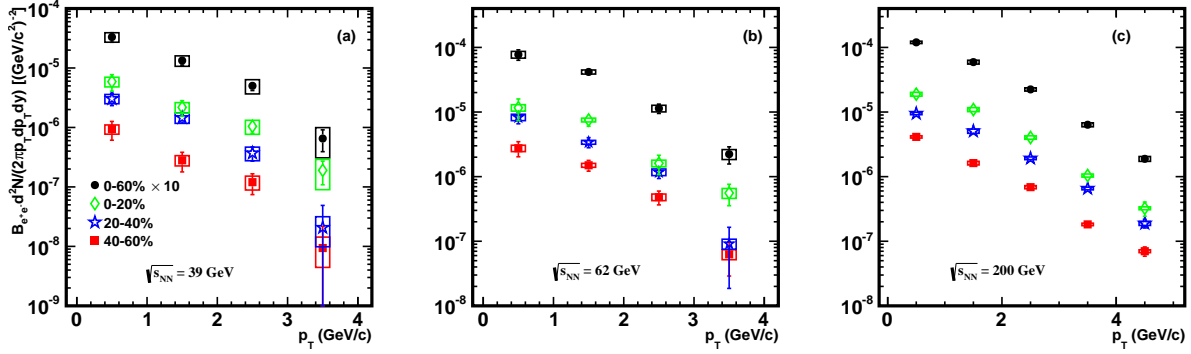


FIG. 57. The invariant yield versus transverse momentum for $|y| < 1$ in 0 – 20%, 20 – 40%, 40 – 60%, and 0 – 60% centrality in Au+Au collisions 39GeV, 62GeV and 200 GeV, respectively.

p_T range (GeV/c)	0 – 1	1 – 2	2 – 3	3 – 4	4 – 5
dca cuts (%)	2.31	1.93	0.99	0.48	-
nHitsFit cuts (%)	3.85	3.49	3.70	4.54	-
$n\sigma_e$ cuts (%)	6.14	4.29	3.33	5.02	-
TOF related cuts (%)	1.10	1.10	1.10	1.10	-
BEMC related cuts (%)	16.47	19.02	25.52	30.96	-
yield extraction (%)	6.00	7.20	12.64	12.44	-
radiative decay (%)	4.00	4.00	4.00	4.00	-
total for 0-60% (%)	19.55	21.57	29.22	34.38	-
total for 0-20% (%)	18.50	20.21	21.54	37.51	-
total for 20-40% (%)	17.79	19.68	22.82	32.84	-
total for 40-60% (%)	17.68	19.66	20.28	35.48	-

TABLE XV. The systematic uncertainties verse p_T for MB Au+Au 39 GeV.

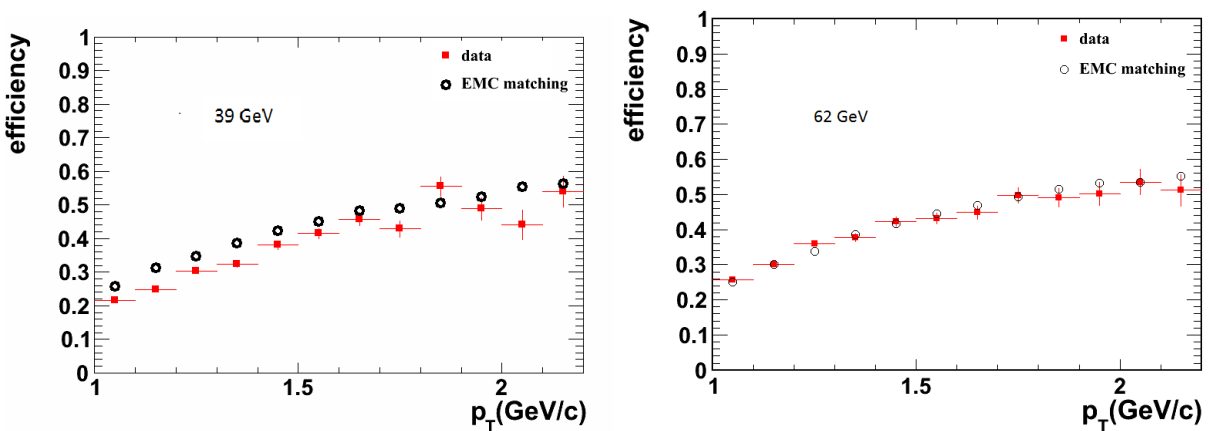


FIG. 58. The BEMC response and related cuts efficiency from simulation and data for Au+Au 39 and 62.4 GeV, respectively.

1 **III. THE INTERPOLATION OF PP REFERENCE AT $\sqrt{s} = 39$ AND 62.4 GEV**

2 **IV. INTRODUCTION**

3 Lattice QCD predicts that, under conditions of extremely high temperatures and energy densities,
4 a phase transition or crossover from hadronic matter to a new form of matter, known as Quark Gluon
5 Plasma (QGP) [10], will occur. The Relativistic Heavy Ion Collider (RHIC) was built to search for
6 the QGP and to study its properties in laboratory through high-energy heavy-ion collisions [11–14].
7 Many observables have been proposed to probe the QGP created in heavy-ion collisions. Among
8 them, the J/ψ suppression caused by the color-charge screening in QGP is one of most important
9 signatures [15].

10 Over the past twenty years, J/ψ production in hot and dense medium has been a topic attracting
11 growing interest. Suppression of J/ψ production has been observed in various experimental mea-
12 surements [16–19]. A similar suppression pattern and magnitude of J/ψ was observed at SPS and
13 RHIC despite more than one order of magnitude difference of collision energy. Furthermore, the J/ψ
14 is suppressed more in forward rapidity than that in midrapidity at RHIC 200 GeV Au+Au collisions
15 [20] and comparable J/ψ nuclear modifications have been observed by PHENIX Collaboration at
16 forward rapidity from $\sqrt{s_{NN}} = 39$ to 200 GeV in Au+Au collisions [21]. These experimental ob-
17 servations suggest that, in addition to color screening, there exist other effects contributing to the
18 modification of J/ψ production. Cold nuclear matter (CNM) effects, the combined contribution of
19 finite J/ψ formation time and finite space-time extent of QGP and recombination from uncorrelated
20 c and \bar{c} in the medium may account for these contributions [22]. Among these contributions, the
21 regeneration of J/ψ from the recombination of c \bar{c} plays an important role to explain the similar
22 suppressions at SPS and RHIC. As the collision energy increases, the regeneration of J/ψ from the
23 larger charm quark density would also increase which partly compensates for the additional suppres-
24 sion from color-screening. The regeneration also expects a stronger suppression at forward rapidity
25 at RHIC where the charm quark density is lower than that at midrapidity. At LHC, the J/ψ is
26 less suppressed in both mid-rapidity and forward rapidity than that at RHIC [23, 24], which may
27 indicate that the regeneration contribution is dominant in the J/ψ production at LHC energies.
28 Measurements of J/ψ in different collision energies at the Solenoidal Tracker at RHIC (STAR) can
29 give us indications on the balance of these mechanisms for J/ψ production and medium properties.

30 To qualify the medium effects on the modification of J/ψ production, the knowledge of J/ψ cross
31 section and kinematics in $p + p$ collision is crucial to offer a reference. The hard interactions in
32 $p + p$ collisions to create the charm quark pairs are well calculated by perturbative QCD (pQCD).
33 However, the subsequent soft process to form J/ψ hadron can not be described within the framework
34 of pQCD, which make it difficult to determine the cross section and kinematics of J/ψ precisely
35 by model calculations. During RHIC year 2010, STAR has collected abundant events of Au+Au
36 collisions at $\sqrt{s_{NN}} = 39$ and 62.4 GeV, while the reference data in $p + p$ collisions is not in the
37 schedule of RHIC run plan. There are several measurements from fixed target $p+A$ experiments
38 [25–27] and Intersecting Storage Ring (ISR) collider experiments [28, 29] at mid-rapidity near these
39 two energy points. However, the p_T shapes from [28] and [29] at 63 GeV are inconsistent with
40 each other and the cross section measurements at 39 GeV [25–27] are comparable to (or even larger
41 than) that at 63 GeV [28, 29]. Therefore, as what we did in ref. [30], we study the world-wide data
42 to obtain the J/ψ reference at these collision energies.

43 In this letter, we report an interpolation of the p_T -integrated and differential inclusive J/ψ cross
44 section in $p + p$ collisions at mid-rapidity to $\sqrt{s} = 39$ and 62.4 GeV. We establish a strategy to
45 estimate the inclusive J/ψ cross section and kinematics at certain energy points, which makes the
46 calculation of the J/ψ nuclear modification factors for any colliding system and energy at RHIC

¹ possible. The extrapolation is done in three steps:

- ² 1) Energy interpolation of the existing total J/ψ cross section measurements.
- ³ 2) Energy evolution of the rapidity distribution.
- ⁴ 3) How transverse momentum distribution changes with energy.

⁵ V. AVAILABLE EXPERIMENTAL RESULTS TREATMENT

⁶ The measurements of J/ψ hadroproduction have been performed for about forty years. In such
⁷ a long period, different experimental techniques have been utilized and different input information
⁸ was available at the time of the measurements. Therefore, comparison of different experimental
⁹ results on an equal footing needs an update of the published values on several common assumptions
¹⁰ and aspects. For example, the branching ratio of $J/\psi \rightarrow e^+e^-$ (or $\mu^+\mu^-$) have changed with time;
¹¹ the assumed functional forms for the x_F and p_T shapes, which can be used to infer the total J/ψ
¹² production, are different in different measurements; and the treatment of the nuclear effects are not
¹³ homogeneous. In this section, we update all the results with the current best knowledge of branching
¹⁴ ratios, kinematics and nuclear effects.

¹⁵ The cross section for J/ψ on a nuclear target is often characterized by a power law:

$$\sigma_{J/\psi}^{pA} = \sigma_{J/\psi}^{pN} \times A^\alpha. \quad (10)$$

¹⁷ where $\sigma_{J/\psi}^{pA}$ is the corresponding proton-nucleus cross section for a target of atomic mass number A ,
¹⁸ $\sigma_{J/\psi}^{pN}$ is the J/ψ proton-nucleon cross section, and α is the parameter which characterizes the nuclear
¹⁹ dependence.

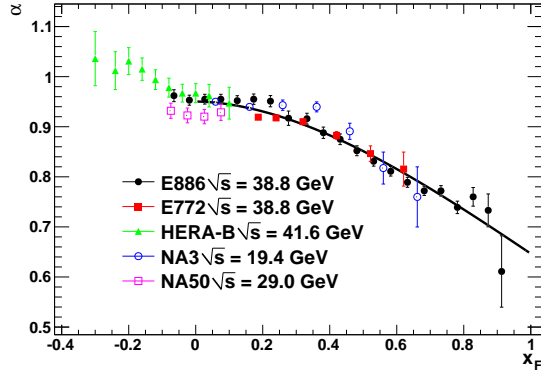


FIG. 59. (color online) Measurements of α defined in Eq. (19) as a function of x_F by various experiments in different collision energies [31–35]. The solid curve represents the parametrization of Eq. (22) discussed in the text.

²⁰ The dependence of α on x_F measured by NA3 [31], NA50 [32], E772 [33], E886 [34] and HERA-B
²¹ [35] is shown in Fig. 59, where x_F is defined as $x_F = 2p_z/\sqrt{s}$ (p_z is longitudinal momentum, along
²² the beam direction.). No significant energy dependence of α as a function of x_F is observed within
²³ uncertainties, thus we assume it is independent of the cms-energy (\sqrt{s}). The results of J/ψ α at
²⁴ $x_F > 0$ can be represented for convenience by simple parametrization shown as solid line in Fig. 59:

$$\alpha(x_F) = a \times e^{-\ln 2(\frac{x_F}{b})^c} \quad (11)$$

where $a = 0.950 \pm 0.003$, $b = 1.38 \pm 0.05$, and $c = 1.81 \pm 0.09$. The J/ψ cross section in proton nucleon collisions are extracted from nuclear target experiments using Eq. (19), wherein the parameter α are interpolated from the data shown in Fig. 59 with Eq. (22). Some of the experimental measurements are only quoted for a limited phase-space. To obtain the total cross sections, the functional forms of x_F and p_T spectrum shapes [35] utilized for extrapolation are

$$\frac{d\sigma}{dx_F} = a \times e^{-\ln 2(\frac{x_F}{b})^c} \quad (12)$$

$$\frac{d\sigma}{dp_T} = a \times \frac{p_T}{(1 + b^2 p_T^2)^c} \quad (13)$$

respectively, where a , b , and c are free parameters. As illustrated in Fig. 60, these two functional forms describe the x_F and p_T spectra very well. All the measurements are updated with the latest branching fractions ($5.961 \pm 0.032\%$ for $J/\psi \rightarrow \mu^+ + \mu^-$, $5.971 \pm 0.032\%$ for $J/\psi \rightarrow e^+ + e^-$) [36]. The treated results on J/ψ cross sections [25–27, 31, 32, 37–42, 44–49, 51–54, 59] are listed in Tab. XVI. They show a good overall consistency, even though some of them contradict with each other. For example, the two measurements (E331 [41] and E444 [42]) at 20.6 GeV deviate from each other by roughly 2σ ; the E705 measurement [47] at 23.8 GeV is higher than the UA6 [44] one at 24.3 GeV by more than 2σ . And there exists no reported global systematic uncertainties in these experiments which could cover the differences.

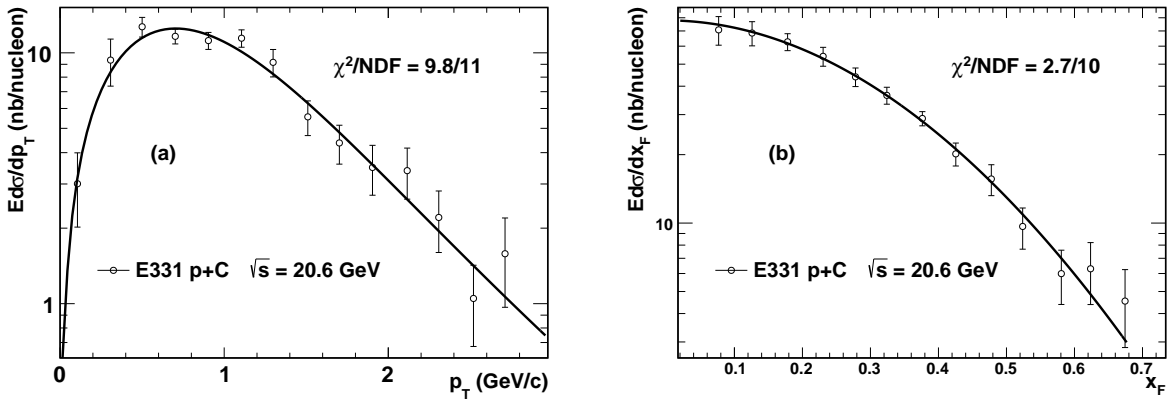


FIG. 60. (color online) Distributions of $Ed\sigma/dp_T$ (left panel) and $Ed\sigma/dx_F$ (right panel) in $p + C$ collisions at $\sqrt{s} = 20.6$ GeV measured by E331 collaboration [41]. The solid lines are fit curves with the functional forms described in the text.

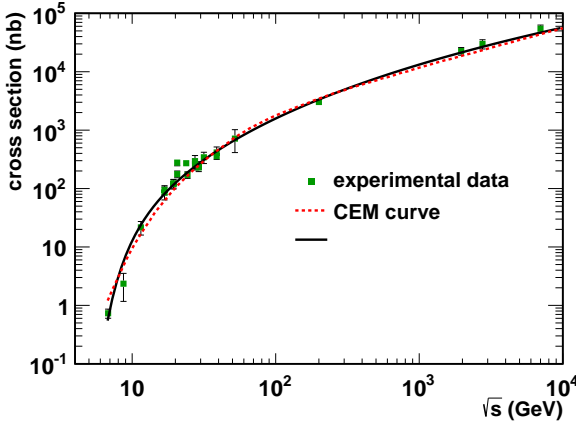
18

VI. RESULTS

The energy evolution of the total inclusive J/ψ production cross section in proton induced interactions is shown in Fig. 61. The first approach is to use the predicted shape in the Colour Evaporation Model (CEM) at Next to Leading Order (NLO) [55] to describe the energy dependence of J/ψ cross section. The central CT10 parton density set [56] and $\{m, \mu_F/m, \mu_R/m\} = \{1.27 \text{ (GeV)}, 2.10, 1.60\}$ set is utilized in the predicted shape, where m is the charm quark mass, μ_F is the factorization scale, μ_R is the renormalization scale. The fit is defined such that the normalization of the NLO CEM calculation is left as a free parameter (α): $\sigma = \alpha \times \sigma_{\text{CEM}}$. The second approach is to use a functional

TABLE XVI. (color online) Updated total ($\sigma_{J/\psi}$) production cross sections in proton-induced interactions.

Experiment	Reaction	\sqrt{s} (GeV)	$\sigma_{J/\psi}$ (nb/nucleon)
CERN-PS [37]	p+A	6.8	0.732 ± 0.13
WA39 [38]	p+p	8.7	2.35 ± 1.18
IHEP [39]	p+Be	11.5	21.63 ± 5.64
E331 [40]	p+Be	16.8	85.15 ± 21.30
NA3 [31]	p+Pt	16.8	95.0 ± 17.0
NA3 [31]	p+Pt	19.4	122.6 ± 21
NA3 [31]	p+p	19.4	120 ± 22
E331 [41]	p+C	20.6	278 ± 32.8
E444 [42]	p+C	20.6	176.5 ± 23.3
E705 [47]	p+Li	23.8	271.51 ± 29.84
UA6 [44]	p+p	24.3	171.42 ± 22.21
E288 [45]	p+Be	27.4	294.12 ± 73.53
E595 [46]	p+Fe	27.4	264 ± 56
NA38/51 [48, 49]	p+A	29.1	229.5 ± 34.4
NA50 [32]	p+A	29.1	250.7 ± 37.6
E672/706 [27]	p+Be	31.6	343.07 ± 75.12
E771 [25]	p+Si	38.8	359.1 ± 34.2
E789 [26]	p+Au	38.8	415.04 ± 100
ISR [59]	p+p	52	716 ± 303
PHENIX [51]	p+p	200	3032 ± 288
CDF [52]	p+ \bar{p}	1960	22560 ± 3384
ALICE [53]	p+p	2760	29912.6 ± 5384.3
ALICE [54]	p+p	7000	54449.4 ± 8494

FIG. 61. (color online) Energy dependence of inclusive J/ψ production cross section [25–27, 31, 32, 37–42, 44–49, 51–54, 59]. The dashed line is the fit from CEM shape [55]. The solid line is a function fit of Eq. (14) as discuss in the text.

form to describe the cross section energy evolution:

$$f(\sqrt{s}) = a \times y_{\max}^d \times e^{\frac{-b}{y_{\max}^c}} \quad (14)$$

where $y_{\max} = \ln(\frac{\sqrt{s}}{m_{J/\psi}})$, a, b, c and d are free parameters. As shown in Fig. 61, both approaches can describe the energy evolution trend of J/ψ cross section. The χ^2/NDF for CEM and Eq. (14) fit are 92.9/22 and 52.6/19, respectively. The large χ^2 mainly comes from three experimental points which contradict with the common trend (E331 and E444 measurements at 20.6 GeV, E705 measurement at 23.8 GeV). If we exclude these three data points and refit the results, the χ^2/NDF for CEM and Eq. (14) fit are 41.6/19 and 15.5/16, respectively. The values extrapolated (without the three experimental points which deviate from the common trend most) for the J/ψ cross sections at $\sqrt{s} = 39$ and 62.4 GeV, utilizing the Eq. (14) and the NLO CEM based fit are listed in Table XVII.

TABLE XVII. Extrapolated values of the J/ψ production cross section at $\sqrt{s} = 39$ and 62.4 GeV. The extrapolated value of CEM is considered as the default set, the difference between CEM and function fit has been taken as the systematic uncertainties of the extrapolation.

Fit	cross section (nb/nucleon)	
	$\sqrt{s} = 39$ GeV	$\sqrt{s} = 62.4$ GeV
NLO CEM	416±16	924±36
Eq. (14)	407±19	828±39
evaluated results	416±16±9	924±36±96

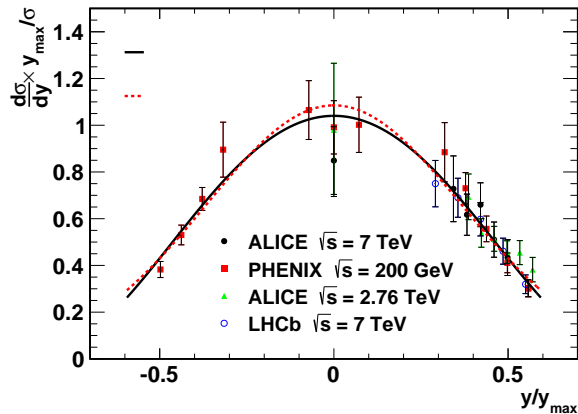


FIG. 62. (color online) Normalized J/ψ production cross section as a function of y/y_{\max} . The two function fits are described in the text. The difference between these two curves has been considered as systematic errors.

The knowledge of the rapidity dependence of J/ψ production at different cms-energies is crucial to obtain a reference for the measurements at mid-rapidity from RHIC. Based on a universal energy scaling behavior in the rapidity distribution obtained at different cms-energies, we explore approaches to the extrapolation of the rapidity distribution. As shown in Fig. 62, the y-differential cross sections at different cms-energies have been normalized by the total cross section, and the normalized values are plotted verse y/y_{\max} , where y_{\max} has been previously defined. Despite more than one order of magnitude difference of collision energy, the treated RHIC [51] and LHC [53, 54, 57] experimental distributions fall into a universal trend, which allows us to perform global fits to all the experimental results with suitable functions. Two functional forms are chosen to describe the normalized $d\sigma/dy$:

$$\frac{1}{\sigma} \frac{d\sigma}{d(y/y_{\max})} = ae^{-\frac{1}{2}(\frac{y/y_{\max}}{b})^2} \quad (15)$$

$$\frac{1}{\sigma} \frac{d\sigma}{d(y/y_{\max})} = \frac{a}{1 - (y/y_{\max})^2} e^{-b(\ln(\frac{1+y/y_{\max}}{1-y/y_{\max}}))^2} \quad (16)$$

where a and b are free parameters. Both of them can describe the global distribution very well ($\chi^2/NDF = 10.1/27$ for Eq. (15), $\chi^2/NDF = 11.2/27$ for Eq. (16)). The statistical uncertainties of rapidity distribution are directly extracted from the fit of Eq. (15). The difference between these two fits has been considered as systematic errors. With the extrapolated J/ψ cross sections and rapidity distributions, the predicted J/ψ cross section times branching ratio at $\sqrt{s} = 39$ and 62.4 GeV at mid-rapidity are $Br(e^+e^-)d\sigma/dy|_{|y|<1.0} = 8.97 \pm 0.59$ and 17.64 ± 2.12 nb, respectively. The uncertainties include statistical and systematic uncertainties from both total cross section and rapidity distribution estimations, they are added in quadrature. These values are highly consistent with the estimations from CEM model (8.7 \pm 4.5 nb for 39 GeV, 17.4 \pm 8.0 nb for 62.4 GeV).

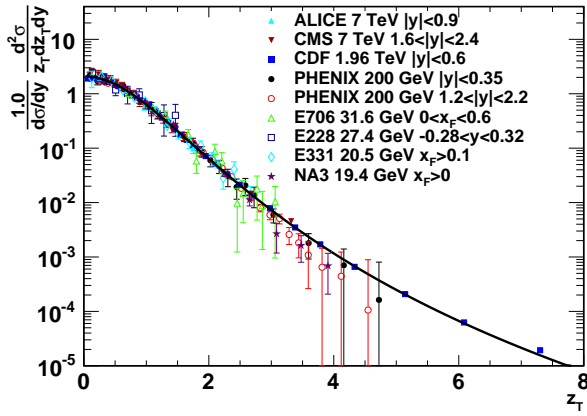


FIG. 63. (color online) J/ψ z_T distributions for available experimental results from $\sqrt{s} = 10$ to 7000 GeV. The solid line is a function fit as discussed in the text.

The energy evolution of J/ψ transverse momentum distribution is also studied via available experimental measurements from $\sqrt{s} = 10 - 7000$ GeV [27, 31, 41, 45, 47, 51, 52, 54, 58, 60]. We used light target data (p [31], Be [27, 45], Li [47], and C [41]) to minimize cold nuclear matter effects. To compare the different experimental measurements at different energies and rapidity domains, as shown in Fig. 63, the transverse momentum distributions are normalized by their p_T -integrated cross sections and plotted verse the z_T variable, which is defined as $z_T = p_T/\langle p_T \rangle$. The treated distributions follow a universal trend despite of the different cms-energies and rapidity domains. We can describe the global distributions very well by the following function:

$$\frac{1}{\sigma} \frac{d^2\sigma}{dz_T dy} = a \times \frac{1}{(1 + b^2 z_T^2)^n} \quad (17)$$

where $a = 2b^2(n - 1)$, $b = \Gamma(3/2)\Gamma(n - 3/2)/\Gamma(n - 1)$, and n is the only free parameter. From the fit, we obtain $n = 3.94 \pm 0.03$ with $\chi^2/NDF = 105.9/151$.

With the universal shape and $\langle p_T \rangle$ information at certain energy and rapidity domain (we focus on mid-rapidity), we can extrapolate the transverse momentum distribution at any cms-energy. Thus the next step is to evaluate the energy evolution of $\langle p_T \rangle$. The $\langle p_T \rangle$ at mid-rapidity as a function of cms-energy from world-wide experiments [27, 31, 41, 45, 50–52, 54, 58, 59] is shown in Fig. 64. Also, only part of the world-wide fixed-target data (with p, Be, Li, and C respectively) are used to reduce the cold nuclear matter effects. The $\langle p_T \rangle$ versus energy can be fitted by the function form:

$$f(\sqrt{s}) = p + q \ln \sqrt{s} \quad (18)$$

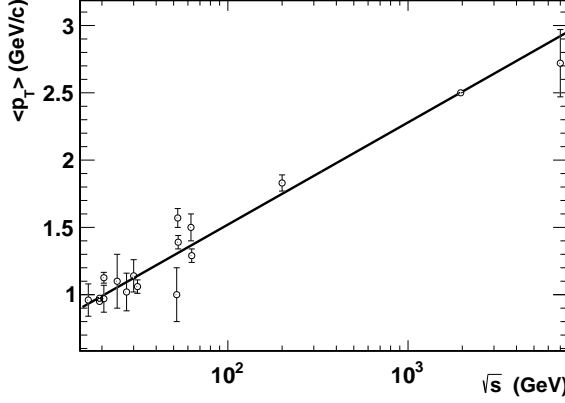


FIG. 64. (color online) $J/\psi \langle p_T \rangle$ at mid-rapidity as a function of cms-energy from $\sqrt{s} = 10$ to 7000 GeV. The solid line is a function fit as discussed in the text.

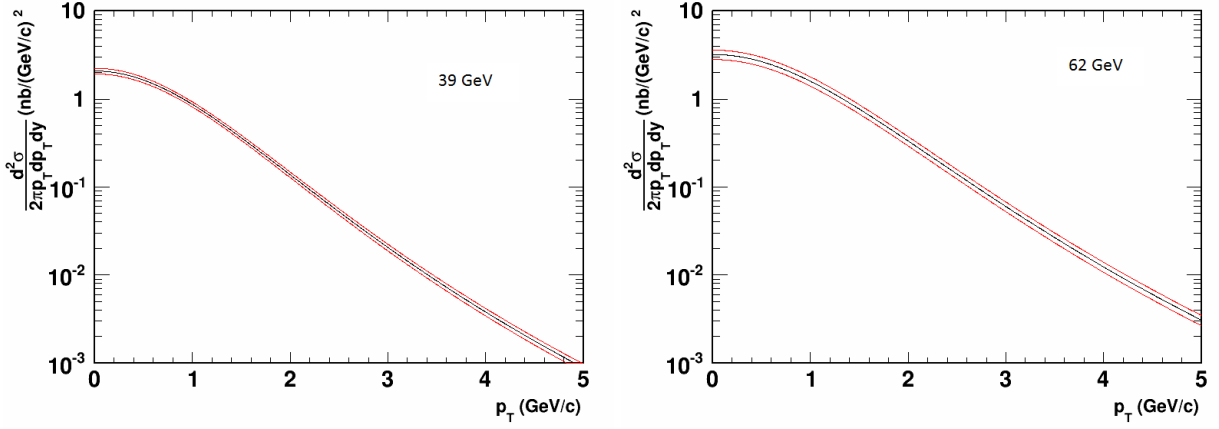


FIG. 65. (color online) The expected J/ψ cross section as a function of p_T for $p+p$ 39 and 62.4 GeV. The red lines represent for the uncertainties from cross section interpolation, rapidity distribution estimation, and p_T shape evaluation.

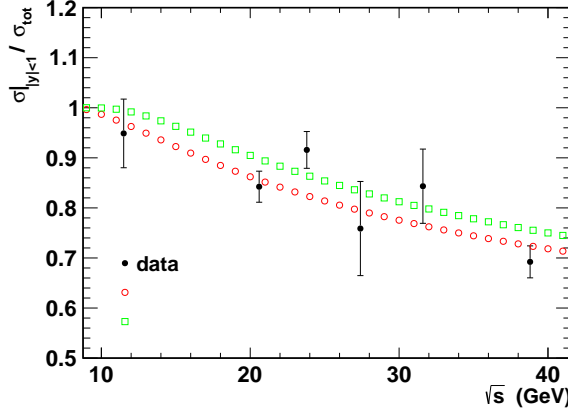


FIG. 66. (color online) The ratios of $J/\psi \sigma|_{y|<1.0}$ to σ_{total} as a function of cms-energy [25–27, 39, 41, 42, 46, 47, 61]. The open points are the estimations using the two fit functions in Fig. 62.

where p, q are free parameters. The fit parameters are $p = 0.0023 \pm 0.0182$, $q = 0.329 \pm 0.031$ with $\chi^2/NDF = 41.1/15$. The estimated $\langle p_T \rangle$ from the fit function at $\sqrt{s} = 39$ and 62.4 GeV are 1.21 ± 0.04 and 1.36 ± 0.04 GeV/c, respectively. With these inputs, the transverse momentum distribution at these two cms-energies can be completely determined and shown in Fig. 65.

There are rare rapidity distribution measurements in p+A collisions at $\sqrt{s} < 200$ GeV. Therefore, the universal energy scaling parameters of rapidity distributions are determined by the measurements at $\sqrt{s} \geq 200$ GeV. Its validity at low energy (< 200 GeV) range still need to be further investigated. But we do have various x_F distribution measurements of J/ψ in fix-target experiments [25–27, 39, 41, 42, 46, 47, 61]. Together with the α verse x_F curve in Fig. 59 and the transverse momentum distributions obtained using the strategy described in the above section, we can evaluate the rapidity distributions via the x_F distributions measurements in the fix-target experiments to check the validity of the rapidity interpolation method. The ratios of $J/\psi \sigma|_{|y|<1.0}$ to σ_{total} , which are calculated utilizing the evaluated rapidity distributions in fix-target experiments, versus cms-energy are shown in Fig. 66. The two sets of open points plotted in the figure are obtained as follows:

- 1) Parameterize the universal $\frac{1}{\sigma} \frac{d\sigma}{d(y/y_{max})}$ versus y/y_{max} trend in Fig. 62 by Eq. (15) and Eq. (16), respectively.
- 2) Extract the rapidity distribution ($\frac{1}{\sigma} \frac{d\sigma}{dy}$ versus y) utilizing the parameterizations of Eq. (15) and Eq. (16), respectively.
- 3) Calculate the ratios of $J/\psi \sigma|_{|y|<1.0}$ to σ_{total} according the rapidity distributions at certain energies.

In this figure, we can see that our extrapolation strategy also works at low cms-energy range.

Eventually, the interpolations of the p_T -integrated and differential inclusive J/ψ cross section in $p + p$ collisions at mid-rapidity could be accomplished as follows:

- 1) The total cross section of J/ψ at certain energy could be extracted through the curves shown in Fig. 61.
- 2) The shape of the rapidity distribution at certain energy could be derived from the universal trend depicted in Fig. 62. The cross section at mid-rapidity can be evaluated in conjunction with the total cross section.
- 3) The p_T distribution at certain energy in mid-rapidity could be obtained via the parametrization of Eq. (17) illustrated in Fig. 63 with $\langle p_T \rangle$ extracted from Fig. 64. Together with the cross section at mid-rapidity, the p_T differential cross section at mid-rapidity is done.

The interpolations at $\sqrt{s} = 39$ and 62.4 GeV are listed in Table XVIII.

TABLE XVIII. The interpolations of cross section and p_T distribution at $\sqrt{s} = 39$ and 62.4 GeV.

rapidity range	cross section (nb/nucleon)	
	$\sqrt{s} = 39$ GeV	$\sqrt{s} = 62.4$ GeV
$ y < \infty$	416 ± 18	924 ± 103
$ y < 1$	301 ± 20	592 ± 71
Parameters of Eq. (17)		p_T distribution
		$\sqrt{s} = 39$ GeV $\sqrt{s} = 62.4$ GeV
n	3.94 ± 0.03	3.94 ± 0.03
$\langle p_T \rangle$	1.21 ± 0.04	1.36 ± 0.04

1 **VII. SUMMARY**

2 We study the world-wide data of J/ψ production and kinematics at $\sqrt{s} = 6.8 - 7000$ GeV. We
 3 have developed a strategy to interpolate the J/ψ cross section, rapidity distribution, and transverse
 4 momentum distribution at any cms-energy in $\sqrt{s} = 6.8 - 7000$ GeV. The rapidity and transverse
 5 momentum distributions measured in different energies have a universal energy scaling behavior.
 6 With this strategy, we predicted that the J/ψ cross section times branching ratio at $\sqrt{s} = 39$ and
 7 62.4 GeV in mid-rapidity are $Br(e^+e^-)d\sigma/dy|_{|y|<1.0} = 8.97 \pm 0.59$, 17.64 ± 2.12 nb, respectively.

8 **VIII. NUCLEAR MODIFICATION FACTOR**

9 Nuclear modification factors (R_{CP} , R_{AA}) are used to quantify the suppression of J/ψ production.
 10 R_{CP} is a ratio of J/ψ production in central collisions to peripheral collisions and defined as follows:

$$12 \quad R_{CP} = \frac{\frac{dN/dy}{\langle N_{coll} \rangle}(\text{central})}{\frac{dN/dy}{\langle N_{coll} \rangle}(\text{peripheral})} \quad (19)$$

13 where $\langle N_{coll} \rangle$ is the average number of nucleon-nucleon collisions in relative centrality bins and
 14 $\frac{dN/dy}{\langle N_{coll} \rangle}$ is the yield per nucleon-nucleon collisions in a given centrality bin. The dN/dy is obtained
 15 by the integration of the J/ψ p_T spectrum. Due to the limit p_T coverage of measurements, the
 16 extrapolation of p_T spectrum is done by two functions shown as below:
 17

$$18 \quad \frac{dN}{dp_T} = a \times \frac{p_T}{(1 + b^2 p_T^2)^n} \quad (20)$$

$$20 \quad \frac{dN}{dp_T} = l \times e^{\frac{m_T}{h}} \quad (21)$$

21 where a , b , n , h and l are free parameters. The difference between these two function fits has been
 22 taken as systematic uncertainties. The detail plots of fitting can be found in Appendix Fig. 71. One
 23 should be aware that we can not get conclusion that J/ψ production is not suppressed when $R_{CP} = 1$,
 24 since the J/ψ production may change already in peripheral Au+Au collisions, in particular from cold
 25 nuclear matter effects. The R_{CP} , as a function of the average number of participants ($\langle N_{part} \rangle$), for
 26 Au+Au collisions at $\sqrt{s_{NN}} = 39$, 62.4 and 200 GeV, are shown in Fig. 67. Note that the peripheral
 27 bin selection for Au+Au collisions at these three energy points is 40 - 60% centrality. Significant
 28 suppression is observed in central Au+Au collisions at 62.4 GeV which is similar as at 200 GeV.
 29 The uncertainties for R_{CP} are mainly coming from TPC tracking cuts. The systematic uncertainties
 30 origin from yield extraction, BEMC and TOF related cuts, and $n\sigma_e$ cuts, are mostly canceled out
 31 or negligible.

32 R_{AA} is obtained by comparing J/ψ production in A+A collisions to the yield in $p + p$ collisions.
 33 It is defined as follows:

$$35 \quad R_{AA} = \frac{1}{T_{AA}} \frac{d^2 N_{AA}/dp_T dy}{d^2 \sigma_{pp}/dp_T dy} \quad (22)$$

36 where $d^2 N_{AA}/dp_T dy$ is the invariant J/ψ yield in A+A collisions and $d^2 \sigma_{pp}/dp_T dy$ is the J/ψ cross

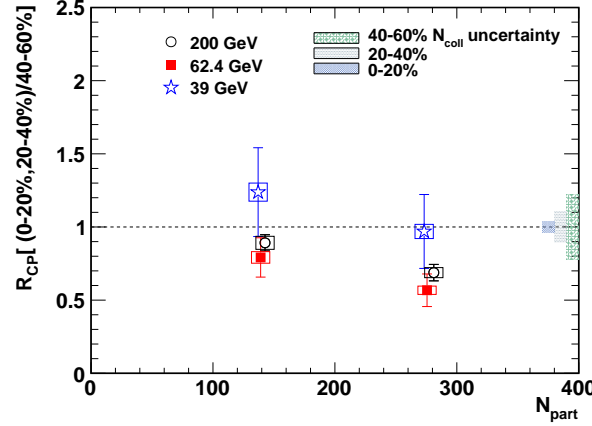


FIG. 67. J/ψ R_{CP} results with respect to 40 – 60% (peripheral) for Au+Au collisions as a function of N_{part} . The error bars represent the statistical uncertainties. The boxes represent the systematic uncertainties. The shaded bands represent the normalization uncertainty from the average number of binary nucleon-nucleon collisions ($< N_{coll} >$) in different centrality bins.

section in $p + p$ collisions. The nuclear overlap function is defined as $T_{AA} = < N_{coll} > / \sigma_{inel}^{pp}$, and takes into account the inelastic cross section in $p + p$ collisions ($\sigma_{inel}^{pp} = 34 \pm 3, 36 \pm 3$ and 42 ± 3 mb for 39, 62.4 and 200 GeV, respectively) and the number of nucleon-nucleon collisions in A+A collisions ($< N_{coll} >$, value and uncertainties can be found at [62]). If there is no any hot or cold nuclear matter effect, the value of R_{AA} should be unity. The J/ψ cross section in $p+p$ 200 GeV collisions, used as baseline, was obtained by combining the STAR data for $p_T > 2$ GeV/c [63] and PHENIX measurements for for $p_T > 2$ GeV/c [64]. With the derived $p + p$ references for 39 and 62.4 GeV, and the measured $p + p$ baseline at 200 GeV , we obtain the R_{AA} of J/ψ for $p_T > 0$ as a function of N_{part} in Au+Au collisions at $\sqrt{s_{NN}} = 39, 62.4$, and 200 GeV, respectively, as shown in Fig. 68.

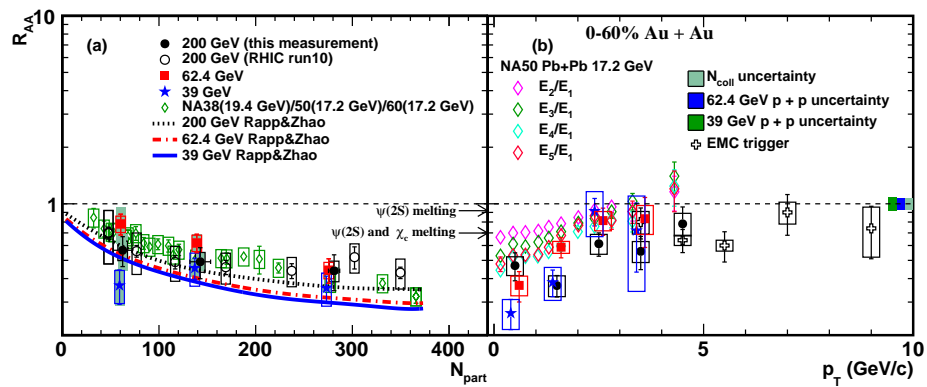


FIG. 68. J/ψ R_{AA} results as a function of N_{part} (panel a) and p_T (panel b) in Au+Au collisions at $\sqrt{s_{NN}} = 39, 62.4$ and 200 GeV. The error bars represent the statistical uncertainties. The boxes represent the systematic uncertainties. The shaded bands indicate the uncertainties from $< N_{coll} >$ and the uncertainties for the derived baselines for 39 and 62.4 GeV. The SPS results are from [65]. The "E_i" in panel (b) denotes the total transverse energy produced in the collision, which is related to the number of nucleons (E_1 : $N_{part} = 79$; E_2 : $N_{part} = 165$; E_5 : $N_{part} = 375$). The ratio of feed-down J/ψ from higher chamonium states to inclusive J/ψ is from [66]. The results of "RHIC run10" are from ref [67] and the results of "EMC trigger" are from ref [68].

-
- 2 [1] <http://www.star.bnl.gov/protected/common/common2011/trigger2011/lumiAu200GeV/>
 3 [2] <http://www.star.bnl.gov/protected/common/common2010/centrality/200GeV/index.html>
 4 [3] H. Bichsel - Comparison of Bethe-Bloch and Bichsel functions - STAR Note SN0439
 5 [4] Particle Data Group. <http://pdg.lbl.gov>.
 6 [5] A. Adare et al., Phys. Rev. Lett **98**, 232002, 2007
 7 [6] T. Zebo et al., Phys. Rev. C **79**, 051901, 2009
 8 [7] A. Spiridonov and D. Zeuthen, arXiv:hep-ex/0510076.
 9 [8] <http://www.star.bnl.gov/protected/common/common2010/trigger2010/lumi62GeV/>
 10 [9] <http://www.star.bnl.gov/protected/common/common2010/trigger2010/lumi39GeV/>
 11 [10] P. Braun-Munzinger, J. Stachel, Nature **448**, 302 (2007).
 12 [11] I. Arsene et al. (BRAHMS Collab.), Nucl. Phys. A **757**, 1 (2005).
 13 [12] K. Adcox et al. (PHENIX Collab.), Nucl. Phys. A **757**, 184 (2005).
 14 [13] B.B. Back et al. (PHOBOS Collab.), Nucl. Phys. A **757**, 28 (2005).
 15 [14] J. Adams et al. (STAR Collab.), Nucl. Phys. A **757**, 102 (2005).
 16 [15] T. Matsui, H. Satz, Phys. Lett. B **178**, 416 (1986).
 17 [16] M.C. Abreu et al., Phys. Lett. B **477**, 28 (2000).
 18 [17] B. Alessandro et al., Eur. Phys. J. C **39**, 335 (2005).
 19 [18] B. Alessandro et al., Eur. Phys. J. C **48**, 329 (2006).
 20 [19] A. Adare et al., Phys. Rev. Lett. **98**, 232301 (2007).
 21 [20] A. Adare et al., Phys. Rev. C **84**, 054912 (2011).
 22 [21] A. Adare et al., Phys. Rev. C **86**, 064901 (2012).
 23 [22] F. Karsch et al., Phys. Lett. B **193**, 105 (1987).
 24 [23] B. Abelev et al., Phys. Rev. Lett. **109**, 072301 (2012).
 25 [24] B. Abelev et al., Phys. Lett. B **734**, 314 (2014).
 26 [25] T. Alexopoulos et al., Phys. Rev. D **55**, 3927 (1997).
 27 [26] M. H. Schub et al., Phys. Rev. D **52**, 1307 (1995).
 28 [27] A. Gribushin et al., Phys. Rev. D **62**, 012001 (2000).
 29 [28] A. G. Clark et al., Nucl. Phys. B **142**, 29 (1978).
 30 [29] C. Kourkounelis et al., Phys. Lett. B **91**, 481 (1980).
 31 [30] W. Zha et al., Phys. Rev. C **88**, 067901 (2013).
 32 [31] J. Badier et al., Z. Phys. C **20**, 101 (1983).
 33 [32] B. Alessandro et al. (NA50 Collab.), Eur. Phys. J. C **33**, 31 (2004).
 34 [33] D. M. Alde et al., Phys. Rev. Lett. **66**, 133 (1991).
 35 [34] M. J. Leitch et al., Phys. Rev. Lett. **84**, 3256 (2000).
 36 [35] I. Abt et al., Eur. Phys. J. C **60**, 525 (2009).
 37 [36] K. A. Olive et al., Chin. Phys. C **38**, 090001 (2014).
 38 [37] A. Bamberger et al., Nucl. Phys. B **134**, 1 (1978).
 39 [38] M. J. Corden et al., Phys. Lett. B **98**, 220 (1981).
 40 [39] Yu. M. antipov et al., Phys. Lett. B **60**, 309 (1976).
 41 [40] K. J. Anderson et al., Phys. Rev. Lett. **36**, 237 (1976).
 42 [41] J. G. Branson et al., Phys. Rev. Lett. **38**, 1331 (1977).
 43 [42] K. J. Anderson et al., Phys. Rev. Lett. **42**, 944 (1979).
 44 [43] L. Antoniazzi et al., Phys. Rev. D **46**, 4828 (1992).
 45 [44] C. Morel et al., Phys. Lett. B **252**, 505 (1990).
 46 [45] H. D. Snyder et al., Phys. Rev. Lett. **36**, 1415 (1976).
 47 [46] E. J. Siskind et al., Phys. Rev. D **21**, 628 (1980).
 48 [47] L. Antoniazzi et al., Phys. Rev. D **46**, 4828 (1992).
 49 [48] M. C. Abreu et al., Phys. Lett. B **444**, 516 (1998).
 50 [49] M. C. Abreu et al., Phys. Lett. B **438**, 35 (1998).
 51 [50] E. Nagy et al., Phys. Lett. B **60**, 96 (1975).
 52 [51] A. Adare et al. (PHENIX Collab.), Phys. Rev. D **85**, 092004 (2012).
 53 [52] D. Acosta et al. (CDF Collab.), Phys. Rev. D **71**, 032001 (2005).
 54 [53] B. Abelev et al. (ALICE Collab.), Phys. Lett. B **718**, 295 (2012).
 55 [54] K. Aamodt et al. (ALICE Collab.), Phys. Lett. B **704**, 442 (2011).
 56 [55] R. E. Nelson, R. Vogt, and A. D. Frawley, Phys. Rev. C **87**, 014908 (2013).
 57 [56] H. L. Lai et al., Phys. Rev. D **82**, 074024 (2010).
 58 [57] R. Aaij et al. (LHCb Collab.), Eur. Phys. J. C **71**, 1645 (2011).
 59 [58] B. Aubert et al. , Nucl. Phys. B **1421**, 29 (1978).
 60 [59] E. Amaldi et al., Nuovo Cim. **19**, 152 (1977).
 61 [60] V. Khachatryan et al. (CMS Collab.), Eur. Phys. J. C **71**, 1575 (2011).
 1 [61] M.S. Kowitt et al., Phys. Rev. Lett. **72**, 1318 (1994).

- ² [62] <http://www.star.bnl.gov/protected/common/common2010/centrality/>
- ³ [63] L. Adamczyk et al., Phys. Lett. B **722**, 55 (2003).
- ⁴ [64] A. Adare et al., Phys. Rev. D **82**, 012001 (2010).
- ⁵ [65] M.C Abreu et al., Phys. Lett. B **499**, 85, (2001).
- ⁶ [66] P. Faccioli et al., JHEP **0810**, 004 (2008).
- ⁷ [67] B.I. Abelev et al., Phys. Rev. C **90**, 24906 (2014).
- ¹ [68] B.I. Abelev et al., Phys. Lett. B **722**, 55 (2013).

2

IX. APPENDIX

1

A. J/ψ signal in Au+Au 39 GeV

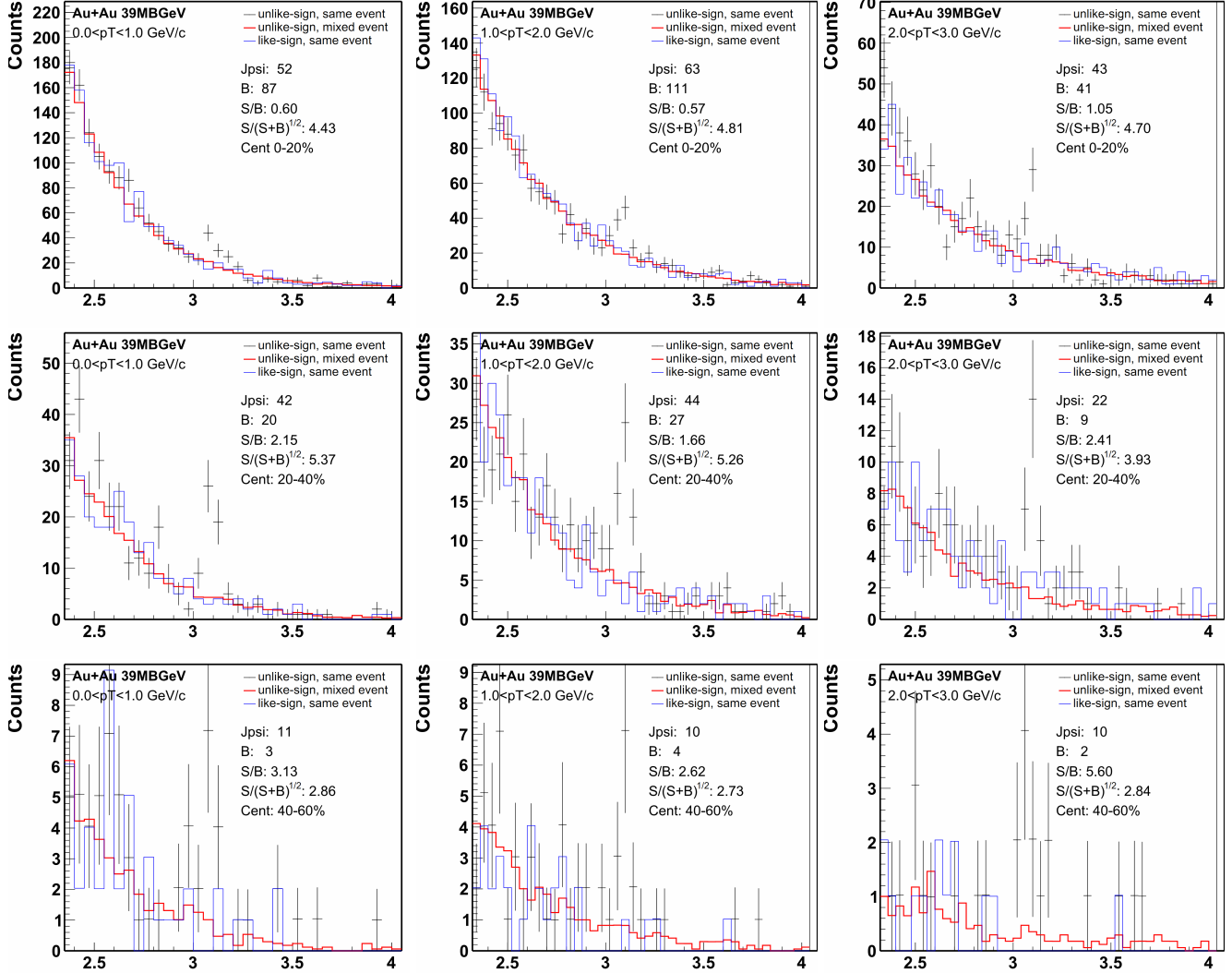


FIG. 69. (color online) J/ψ signal in different p_T and centrality bins for Au+Au 39 GeV collisions.

B. J/ψ signal in Au+Au 62 GeV

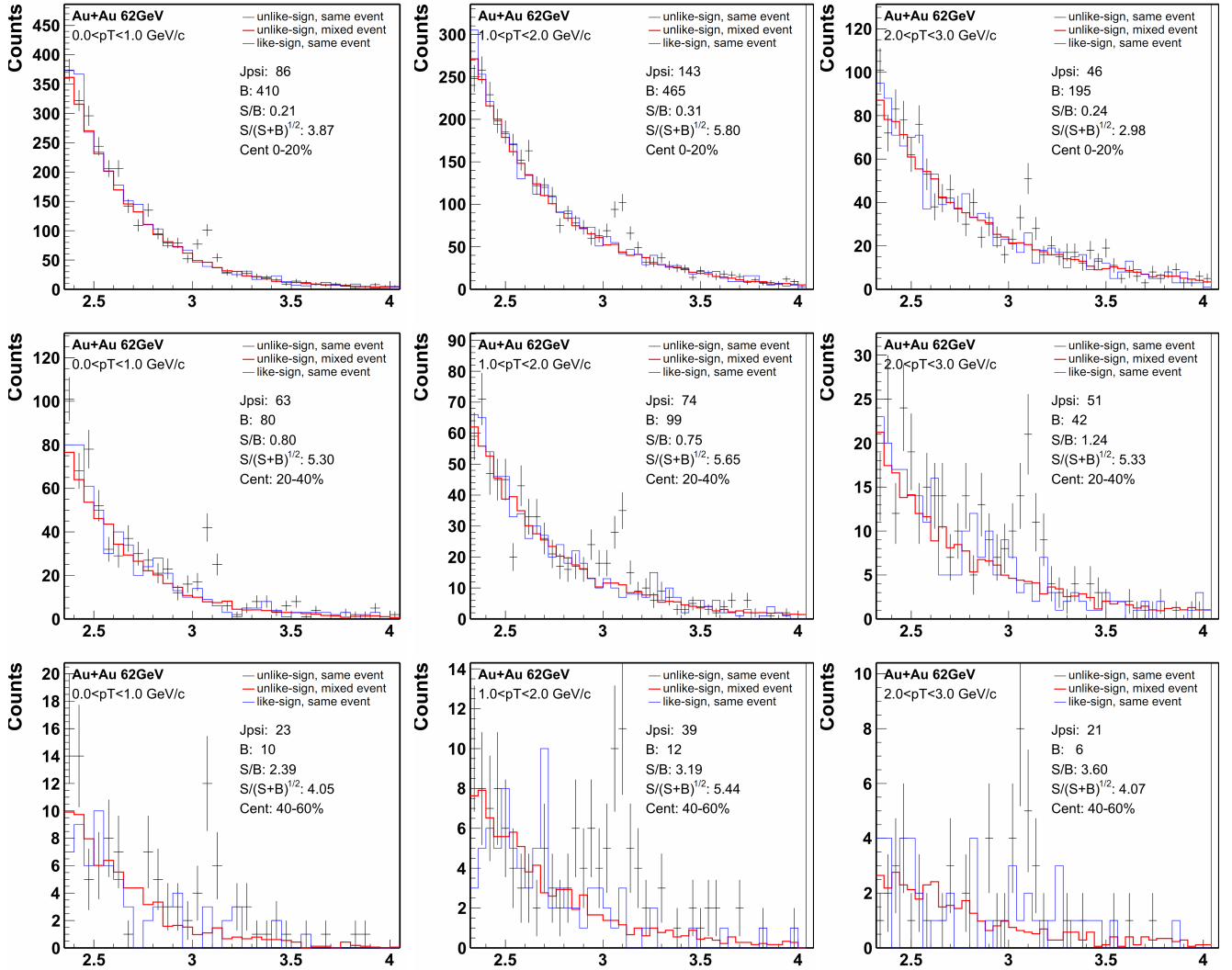


FIG. 70. (color online) J/ψ signal in different p_T and centrality bins for Au+Au 62 GeV collisions.

C. $\text{J}/\psi p_T$ spectrum in different centrality bins for Au+Au 39, 62, and 200 GeV collisions

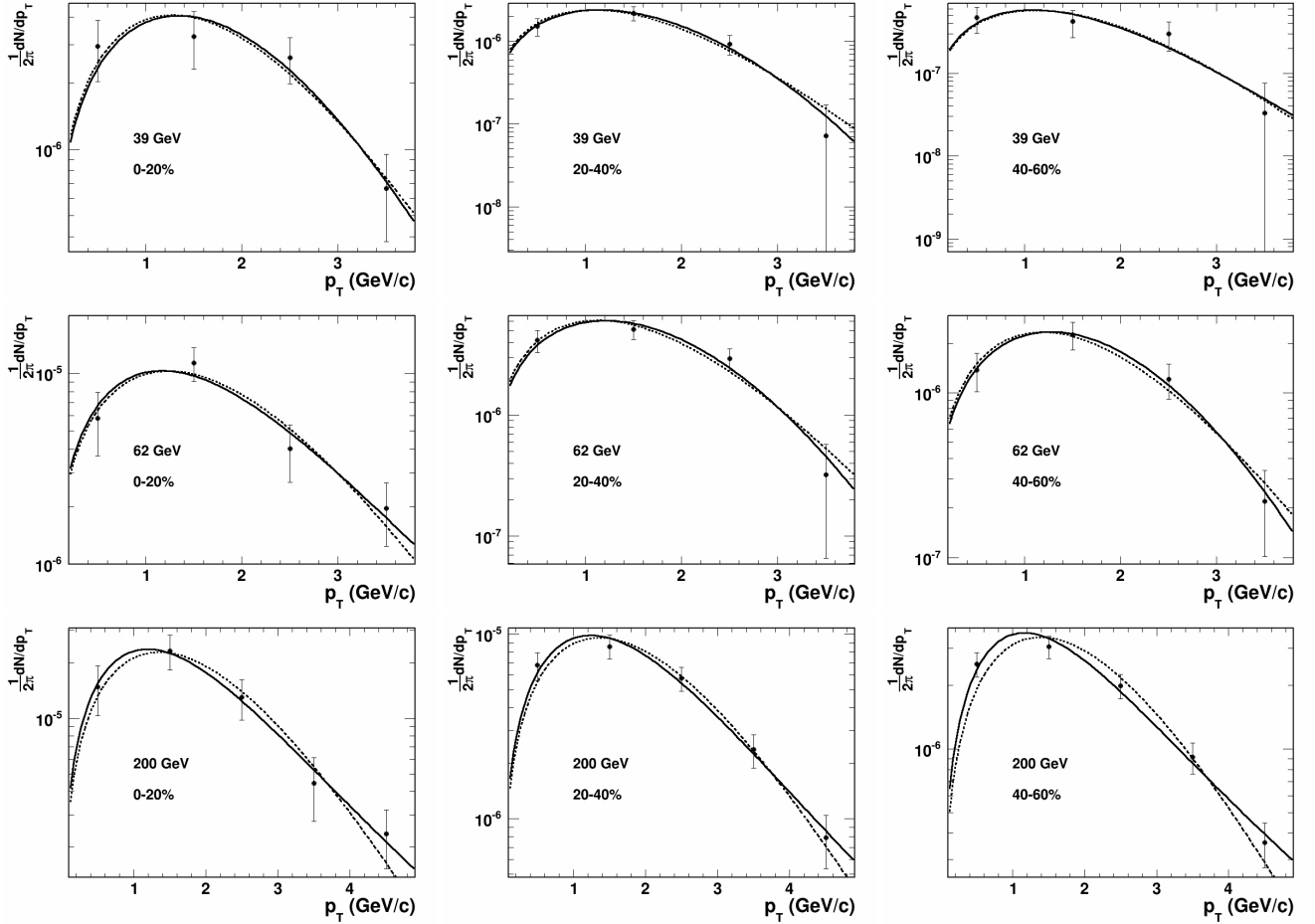


FIG. 71. (color online) $\text{J}/\psi p_T$ spectrum in different centrality bins for Au+Au 39, 62, and 200 GeV collisions. The solid line is the function fit of Eq. (20). The dashed line represents for the fit of Eq. (21).

D. The $\text{J}/\psi p_T$ spectrum for 200 GeV in comparison with published RHIC RUN 2010 results

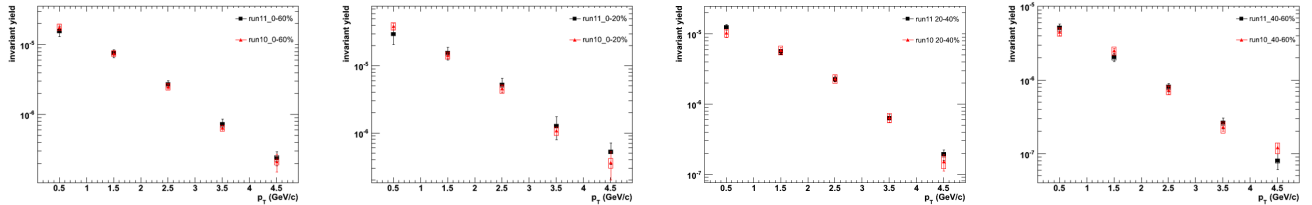


FIG. 72. (color online) $\text{J}/\psi p_T$ spectrum in different centrality bins for Au+Au 200 GeV collisions in comparison with published RHIC RUN 2010 results.